Monitoring of camera positions for Auger Fluorescence Telescopes

von

Joaquín Calvo de Nó

Diplomarbeit in Physik

vorgelegt der

Fakultät für Mathematik, Informatik und Naturwissenschaften

der

RheinischWestfälischen Technischen Hochschule Aachen

im

März 2008

angefertigt am

III. Physikalischen Institut A

Erstgutachter und Betreuer

Prof. Thomas Hebbeker
III Physikalisches Institut A
RWTH Aachen

Zweitgutachter

Prof. Martin Erdmann
III Physikalisches Institut A
RWTH Aachen

Contents

1 Introduction

1.1 Cosmic Rays

The Earth's atmosphere is constantly hit by a large amount of particles originating from space. These particles consist for the most part of protons, though there are also smaller proportions of other charged particles such as alpha particles, electrons and heavier atomic nuclei. Although these particles do not form a beam or a ray, "cosmic ray" is the common term used to describe them.

This phenomenon was first observed by the physicist Victor Hess in the year 1912 [1]. In an experiment he systematically measured the ionization rate at altitudes up to 5300 meters during several balloon flights. His result showed a considerable increase in the ionization rate in comparison to the data at ground level. He attributed this effect to a radiation of great penetrating power coming from outside the atmosphere. For this discovery he was later awarded the Nobel Prize in Physics.

Since then, a vast number of different experiments have tried to explain the nature and origin of these mysterious particles. Nevertheless, the study of cosmic rays remains to this day one of the most relevant domains in the field of astroparticle physics.

1.1.1 Energy Spectrum

The energy spectrum of the cosmic rays describes the energy dependence of the cosmic ray flux in a range between 10^8eV and 10^{20}eV. For lower energies, cosmic rays are deviated from the heliosphere by the solar wind and its embedded magnetic field. As a result of this, cosmic rays below that energy do not reach the Earth's atmosphere. Fig. 1 displays the energy spectrum of the primary particles of cosmic rays in a logarithmic scale. The continuous spectrum demonstrates a decrease of the flux for increasing energies. As a result of this, at the highest energies the rate of particles does not exceed 1 per km^2 per century.

At first sight, the cosmic ray flux closely follows a simple power law shown in equation 1. Upon a closer look, the measured spectrum does however reveal some particularities not described by the same power law [20],[21]. This can be seen in Fig. 2, where the flux is multiplied by $E^{2.5}$ to amplify the deviations from the power law. These deviations occur at certain energies and are commonly referred to as the "knee" and the "ankle" due to their form in the spectrum.

$$\frac{d^2\phi(E)}{d\Omega\, dE} = const \cdot (E/GeV)^{-\gamma} \frac{1}{GeV \cdot sr \cdot cm^2} \tag{1}$$

The knee appears approximately at an energy of 10^{15}eV and consists basically in a

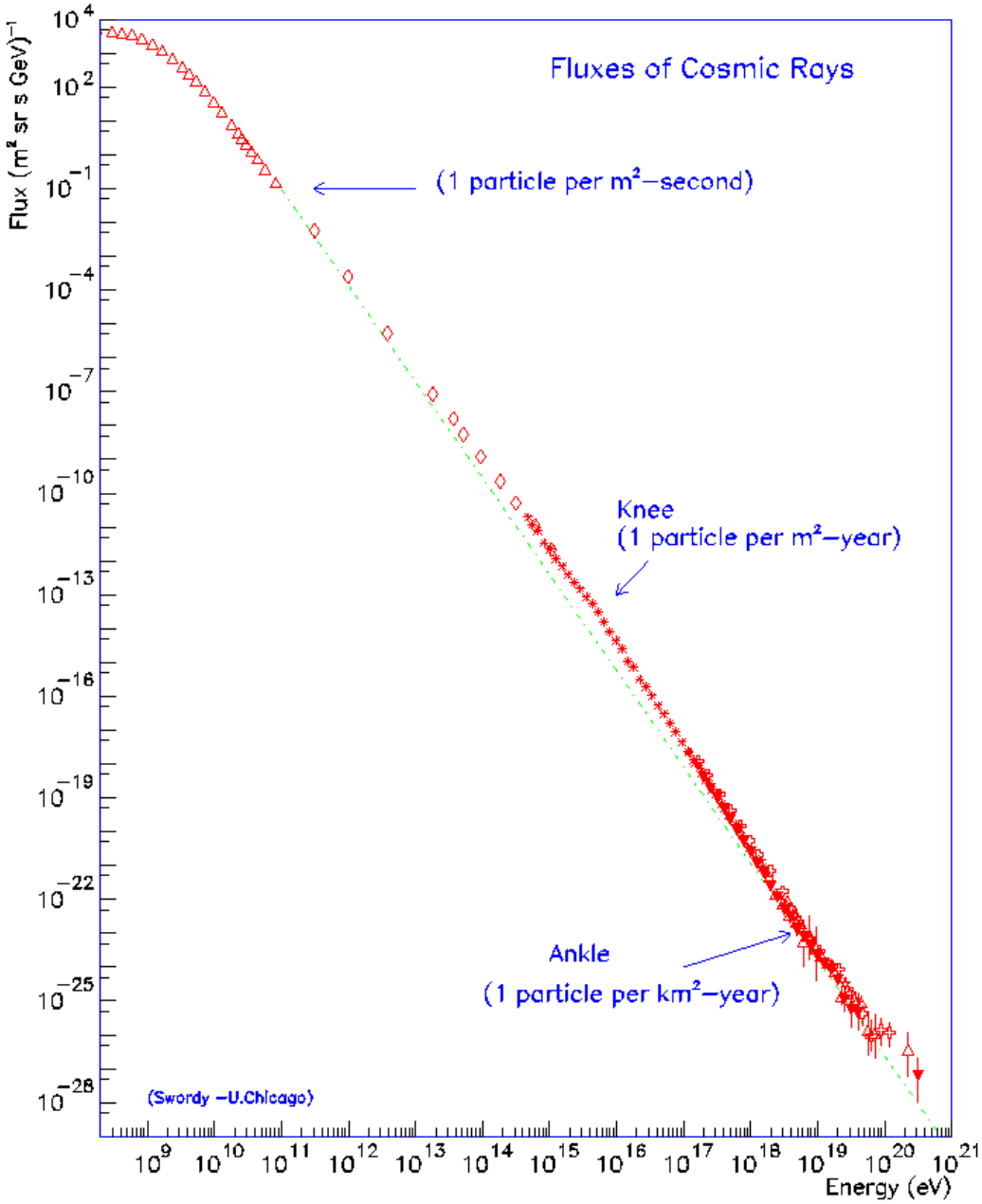

Figure 1: Energy spectrum of Cosmic Rays, from 10^8eV to 10^{20}eV, adapted from [4].

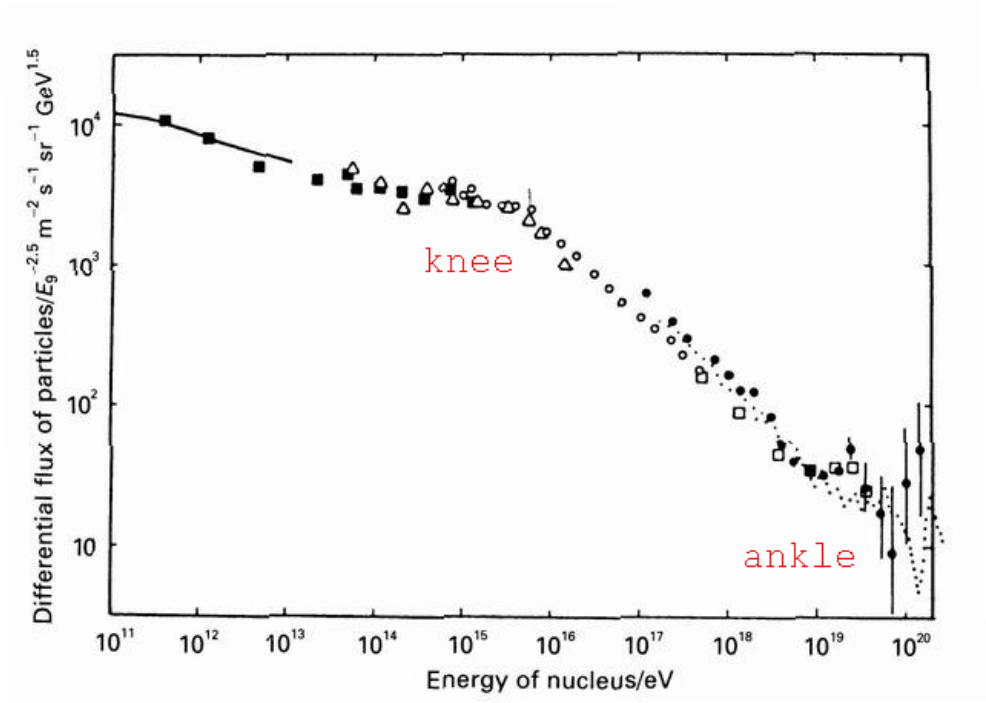

Figure 2: Energy spectrum of Cosmic Rays, with the flux multiplied by a factor $E^{2.5}$ to show the knee and the ankle [25].

variation of the spectral index γ, roughly from 2.7 to 3.1. This results in a slightly more slanted curve in the range of the spectrum located between 10^{15}eV and 10^{18}. There are several theories about the origin of the knee, though the definitive cause of this phenomenon remains uncertain.

For energies higher than 10^{18}eV, the nature of the spectrum changes once more, likely due to the transition from galactic to extragalactic Cosmic Rays. This hypothesis implies that the magnetic field of the galaxy is not strong enough to contain the particles exceeding this energy inside, leaving only the possibility of extragalactic cosmic ray sources. This phenomenon manifests itself in the form of an additional variation of the spectral index, which returns to a value close to 2.7. Its effect in the form of the Cosmic Ray spectrum is referred to as the ankle.

Finally, for energies higher than $6{\cdot}10^{19}$eV the existence of Cosmic Rays is expected to be strongly limited by the Greisen-Zatsepin-Kuzmin (GZK) cutoff [9]. This threshold predicts that, above this aforementioned energy, Cosmic Rays interact with the 2.7K cosmic microwave background. The interaction would then lead to the production of pions according to the processes 2 and 3 and hence to the reduction of the particle energy.

$$\gamma + p \rightarrow \Delta^+ \rightarrow p + \pi^0 \tag{2}$$

or

$$\gamma + p \rightarrow \Delta^{+} \rightarrow n + \pi^{+} \tag{3}$$

As a result of this, cosmic rays with energies above $6{\cdot}10^{19}$eV are attenuated over cosmic distances (see Fig. 3). There is considerable controversy about the existence of this phenomenon [17],[18]. However, recent results of the Pierre Auger Collaboration strongly suggest its presence [26].

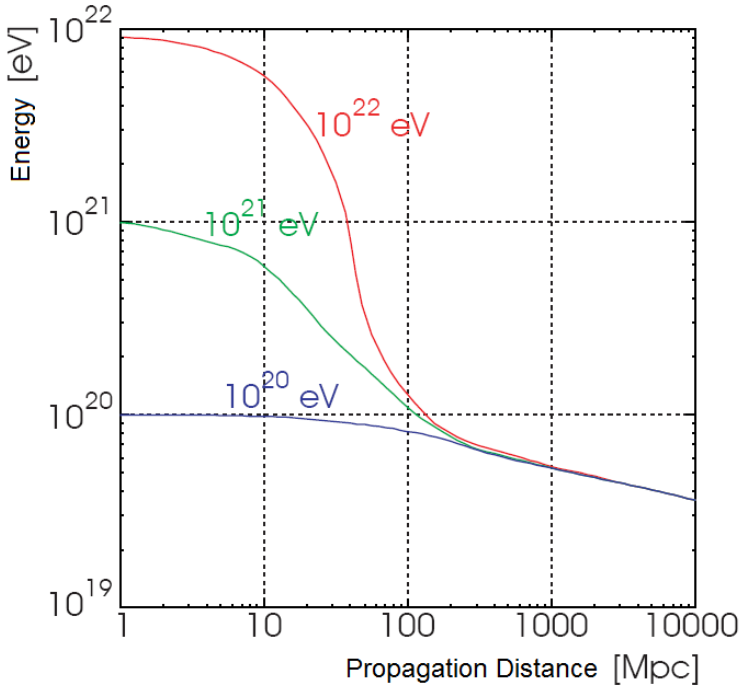

Figure 3: Diagram showing the theoretical energy attenuation caused by the GZK threshold as a function of the propagation distance, for three different energies (adapted from [23]).

1.1.2 Cosmic Ray Sources

The variety of particle energies shown in the spectrum is a likely indication of the variety of cosmic ray sources. There are many candidates for cosmic ray sources, the most notable being supernova remnants (SNR), white dwarves, neutron stars, active galactic nuclei (AGN), radio galaxies and colliding galaxies. Cosmic rays can then be divided into two categories depending on their origin, which is either galactic and extragalactic.

The first section of the energy spectrum corresponds to cosmic rays originating inside our galaxy. They are typically associated with supernovae or neutron stars. Albeit already very energetic, galactic cosmic rays do not reach the necessary amount of energy for their trajectories to remain undisturbed by the galactic magnetic field. Therefore, the direction of the incoming particle does not point to its original source. Furthermore, much like for the solar wind, cosmic rays with energies roughly lower than 10^{10}eV are deflected to the poles by the Earth's magnetic field before their entrance in the atmosphere. As stated in the previous chapter, for energies around 10^{18}eV, a transition from galactic to extragalactic cosmic ray sources is expected to occur.

The term Ultra High Energy Cosmic Rays (UHECR) describes particles in the final section of the cosmic ray energy spectrum (E $> 10^{19}$eV). With energies at these scales, the trajectories of the particles suffer negligible deflections. As opposed to cosmic rays of lower energies, it is therefore possible to locate their origin by establishing their direction as they arrive to the Earth.

A study of the properties of Ultra High Energy Cosmic Rays is essential for the understanding of the GZK cutoff. The Hillas diagram [5] in Fig. 4, based on equation 4 limits the possible sources capable of accelerating particle to these energies mainly to AGNs or colliding galaxies.

$$E_{max} \approx \beta \cdot c \cdot Ze \cdot B \cdot L \tag{4}$$

This equation provides an approximation of the maximal possible energy for a given source. $\beta \cdot c$ describes the shock speed, Ze the electric charge of the particle, B refers to the strength of the magnetic field and L to the typical size of the medium. The formula basically conveys that the particle's maximal Gyroradius (or Larmor radius) is limited by the size of the phenomenon that accelerates it. The maximal energy is therefore proportional to the size of the phenomenon as well as the strength of its magnetic field.

1.1.3 Cosmic Ray Acceleration

The structure of the cosmic ray spectrum does not resemble the form expected from a black body spectrum. This excludes the possibility of thermal acceleration as the explanation for cosmic rays and suggests a process with a resulting power law distribution. This hypothetical mechanism would therefore be responsible for the acceleration of cosmic rays beyond thermal energies.

In 1949 Enrico Fermi, another Nobel prize laureate, suggested a process to ex-

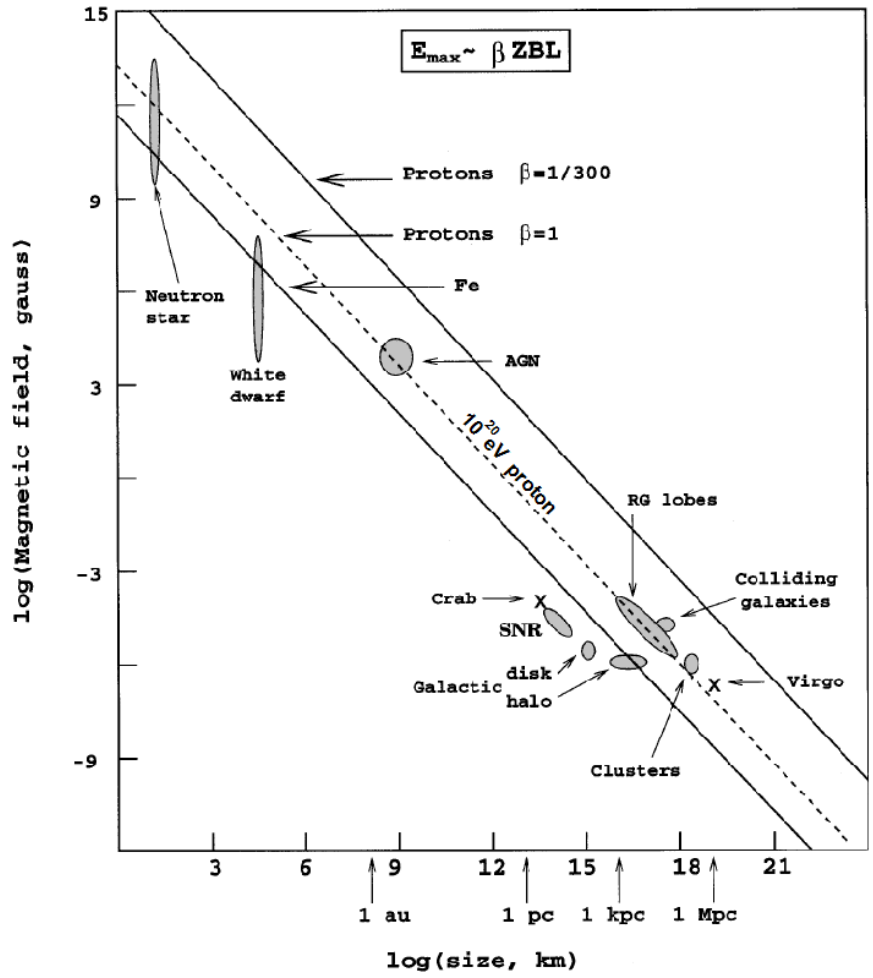

Figure 4: Hillas diagram, adapted from [5]. The region above the diagonal lines indicates the phenomena capable of accelerating particles to energies higher than 10^{20}eV.

plain the acceleration of cosmic rays[11], a process known as Fermi-acceleration. It is supposed to involve moving interstellar magnetic fields interacting with charged particles. Fermi predicted two types of resulting accelerations, the first and the second order Fermi-acceleration. The former is based on the interaction of charged particles with shock waves. The charged particles crossing these shock waves would be confined between the turbulent magnetic fields both preceding and following them. The particles would then bounce back and forth, gaining energy with each cycle and finally reaching a critical energy that releases them from the shock wave.

The second order Fermi-acceleration based on the collision of charged particles with randomly moving magnetized gas clouds is supposed to cause a similar effect. These clouds end up acting as a magnetic mirror, potentially reflecting the charged particles with increased energies. If the magnetic cloud is moving towards the particle, the resulting head-on collision should increase the particle energy. Statistically, the probability of a head-on collision is greater than a head-tail collision, causing on average an increase of the particle energy.

For the first order Fermi-acceleration, the energy gain per shock depends linearly on the shock velocity β. In contrast, for the second order Fermi-acceleration, the energy gain per collision is proportional to the β^2 of the mirror. Hence the name of the two processes. In both cases the resulting spectrum of the accelerated particles is closely described by a power law. Therefore, both types of Fermi-acceleration provide possible explanations for the existence of cosmic rays. Strong magnetic fields capable of achieving this effect are found for example in supernova remnants, centers of galaxies or radio galaxies.

1.1.4 Extensive Air Showers (EAS)

In 1939, the physicist Pierre Auger carried out a cosmic ray measurement involving an array of detectors distributed over an area of $25m^2$. He discovered the existence of a time coincidence in a large number of the recorded events [3]. This led him to the conclusion that the coincident events were the result of a single incident primary particle. The term Extended Air Showers (or Cosmic Ray Showers) refers to the production of a large amount of particles by individual cosmic particles.

Upon entering the Earth's atmosphere, cosmic rays collide with atmospheric nuclei and produce new particles. These secondary particles remain very energetic and continue interacting with the surrounding particles, leading to the production of more and more particles and thereby forming a cascade. The size of the shower rises until a maximum is reached where the energy loss caused by ionisation dominates over the creation of new particles. From that point on, the size of the EAS starts to decline. The shower propagation however continues until finally the energy of the original primary particle is distributed over a large amount of particles. Eventually, a fraction of the total number of particles (essentially electrons and muons)

reach the ground. Unlike the intensity, which depends mainly on the energy of the primary particle, the shape of the EAS is essentially energy independent due to the large amount of interactions involved.

Fig. 5 displays the possible reactions and classifies them in three separate components: the hadronic component, the muonic component and the electromagnetic component. This can be explained with a closer examination of the shower development. After the first interaction, the production of pions ($\pi^{\pm}$ and π^{0}) and, to a lesser extent, kaons ($K^{\pm}$ and K^{0}), typically takes place. These particles can then interact with nuclei in the air and create new hadrons, thus forming a core of hadronic particles and continuing the hadronic development of the shower. The charged pions and hadrons can however also decay into muons and muon neutrinos, while the neutral pions decay mostly into photons. The photons finally lead to the creation of the electromagnetic component by the means of electron-positron pair production or Compton effect. The electromagnetic cascades that appear as a result of this are responsible for the creation of approximately 90% of the charged particles. Through ionisation losses, most of the energy of these particles is dissipated.

The muons produced in the muonic component of an EAS are, due to their relatively high mass, very penetrating. This allows them to reach the ground level mostly unattenuated.

For electromagnetic particles, the radiation length defines their mean penetration depth in a given medium. In the case of hadrons, this is given by the nuclear interaction length. To understand the distribution behind the shower development, it is perhaps helpful to consider a basic model first.

In the Heitler model [6], the interaction length determines a fixed distance λ for which a particle will always undergo a collision. The two particles resulting from the collision will each receive half the energy from the original. This way, after n interactions, the number of particles will reach:

$$N(X) = 2^{X/\lambda} \tag{5}$$

where $n = X/\lambda$ and X therefore refers to the distance traveled along the shower axis. The parameter X, whose value is given in g/cm^2, is called the "slant depth". At some point the decreasing energy of the shower particles will reach a critical value E_{cr}, for which the particle creation will stop. This simple model allows an approximate calculation of some important shower parameters. For instance, a particle at slant depth X will therefore have an energy of $E(X) = E_0/N(X)$, where E_0 refers to the primary particle energy. This means that, at the shower maximum, the slant depth will be given by:

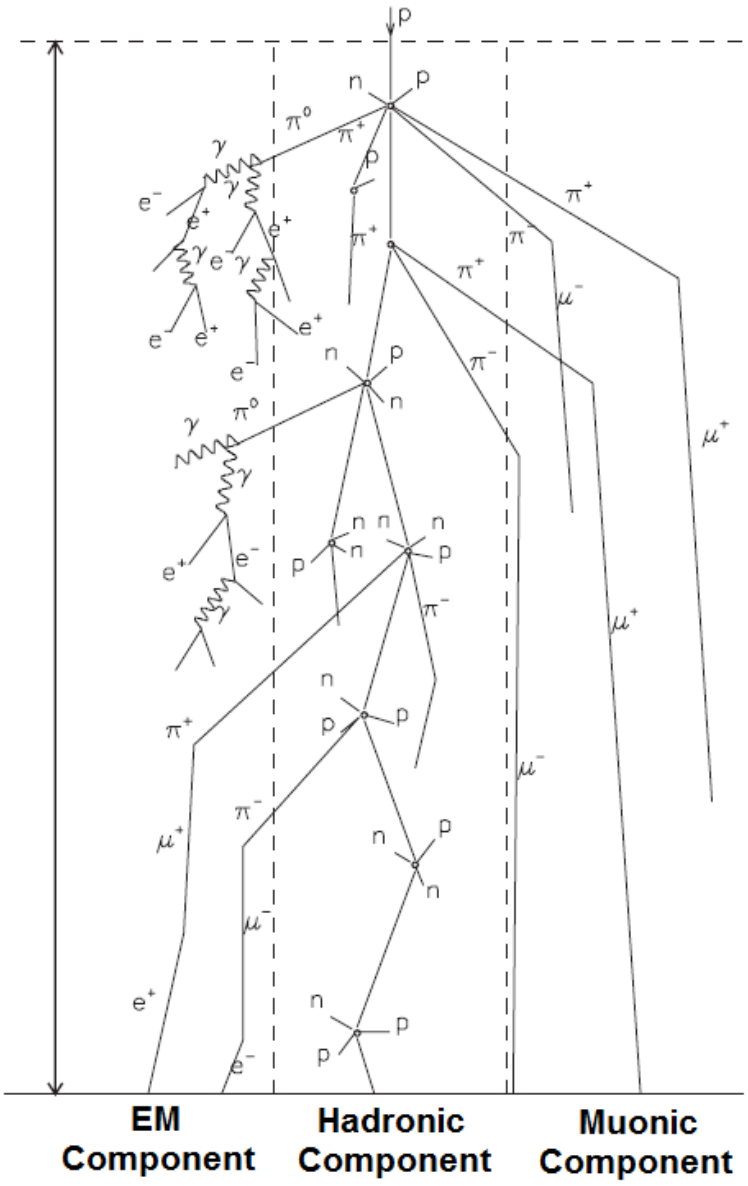

Figure 5: Schematic diagram representing the reactions to be found in an extended air shower, adapted from [12].

$$X_{max} = \lambda \cdot \frac{ln(E_0/E_{cr})}{ln(2)} \tag{6}$$

The simple Heitler model is nevertheless successful in providing basic but fundamentally correct approximations of the relations between some of the shower parameters.

The development of the electromagnetic component of an EAS is essentially similar to the explanation provided by the Heitler model. It is conditioned by the diverse energy loss reactions that occur at different energy ranges. These processes are mainly: pair production, Compton effect and photo-electric effect for photons, and ionisation as well as Bremsstrahlung for electrons. Of these effects, pair production and Bremsstrahlung are associated to the higher energies, while the photo-electric effect and ionisation predominate for lower energies (for energies below E_{cr}). Taking the Heitler model as a starting point, different approximations of the shower development can then be extrapolated depending on assumptions about the energy loss processes. The electromagnetic component of the EAS, which contains the overwhelming majority of shower particles, is finally given by the Gaisser-Hillas function [5]:

$$N = N(X_{max}) \cdot \left(\frac{X - X_0}{X_{max} - X_0}\right)^{(X_{max}-X_0)/\lambda} \cdot exp\left(\frac{X_{max} - X_0}{\lambda}\right) \tag{7}$$

where X_0 corresponds to the atmospheric depth of the first interaction, $N_{max} = N(X_{max})$ and the constant λ is equal to 70 g/cm^2. With this equation, it is possible to estimate the number of electromagnetic charged particles N as a function of the atmospheric depth, thus providing the longitudinal structure of the shower. The formula does, in fact, describe the initial particle increase as well as the subsequent decrease, as the energy losses caused by ionisation starting to gain importance.

Through Coulomb scattering, the electrons of the shower spread laterally away from the core. Since the scattering is inversely proportional to the particle energy, lower energy particles spread the most. As a result of this, the area covered by the shower increases, thereby reaching sizes of several square kilometers. In addition, the changed trajectory of the lateral particles result in the formation of a curved shower front. The lateral distribution function describes the lateral particle density as a function of the distance from the shower core. An approximation of the lateral shower structure was parametrized by Kamata, Nishimura and Greisen (NKG-function)[22]:

$$f_{NKG}(R/R_0) \propto (R/R_0)^{s-2} \cdot (1 + R/R_0)^{s-4.5} \tag{8}$$

where $s = 3X/(X + 2X_{max})$ defines the shower age, while the Molière radius is given by $R_0 \approx$9.3g/cm^2. The equation 8 is theoretically related to the density of charged

particles at ground level, which can be directly measured by an array of detectors. Hence the importance of this function for cosmic ray experiments.

1.2 The Pierre Auger Observatory

The Pierre Auger Observatory[19] for the study of Ultra High Energy Cosmic Rays is run by an international collaboration. It is especially adapted for the detection of cosmic rays with energies above 10^{18}eV. Its detecting methods are twofold, consisting of a `Fluorescence Detector` or FD and a `Surface Detector` or SD. The resulting cross-calibration allows for redundancy in its measurements and leads therefore to important reductions in systematic uncertainties. This leads to a very accurate event reconstruction. As a result of the twofold detecting mechanism, the design of the observatory is also referred to as `hybrid`.

1.2.1 The Fluorescence Detector

In addition to interactions mentioned in chapter 1.1.4, the shower particles also interact with nitrogen atoms in the atmosphere in a way that results in the emission of faint ultraviolet fluorescence light. Unlike the shower cascade, this light is emitted isotropically and does not follow the direction of the primary particle. The extended air showers can thus be detected at ground level at distances of several kilometers from the shower core.

With the detection of ultraviolet fluorescence light in the atmosphere it is then possible to reconstruct the direction and energy of cosmic ray showers as they propagate in the atmosphere. In the Pierre Auger Observatory, this task is performed by the Fluorescence Detector or FD. The FD is composed of 24 telescopes, distributed in four different buildings (also called "eyes"), with six telescopes each (see Fig. 6).

A schematic representation of a typical fluorescence telescope is shown in Fig. 7. Each one of the 24 telescopes has an identical structure consisting of the same two elements: A 13m^2 segmented spherical mirror with a radius of 3.4m captures the light coming through the telescope's window and reflects it back to a camera composed of 440 photomultipliers. The photomultipliers are arranged in a 20×22 pixel configuration, each one covering a field of view of about 1.5×1.5 degrees. Together, in a single camera, they cover a field of view of 30×30 degrees. Each `eye` therefore covers a total range of 180×30 degrees.

The window of each telescope is equipped with a corrector lens and a filter that improve the quality of the signal and reduce the background. The optical axis, which traverses the centers of both camera and mirror, forms an angle of 16^o with the horizontal axis. This allows the telescopes to cover the range between 1 and 31^o from the horizontal.

The detector operates much in the same way as a calorimeter, detecting the light emitted by the EAS in the air and extrapolating its total energy. However, in order for the detection to be successful, the background light captured by the detector is

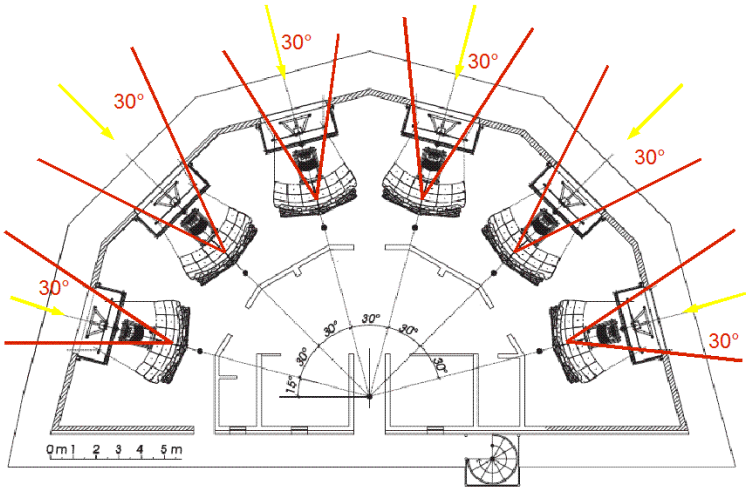

Figure 6: General layout of the fluorescence telescopes inside a typical Fluorescence Detector Eye [7].

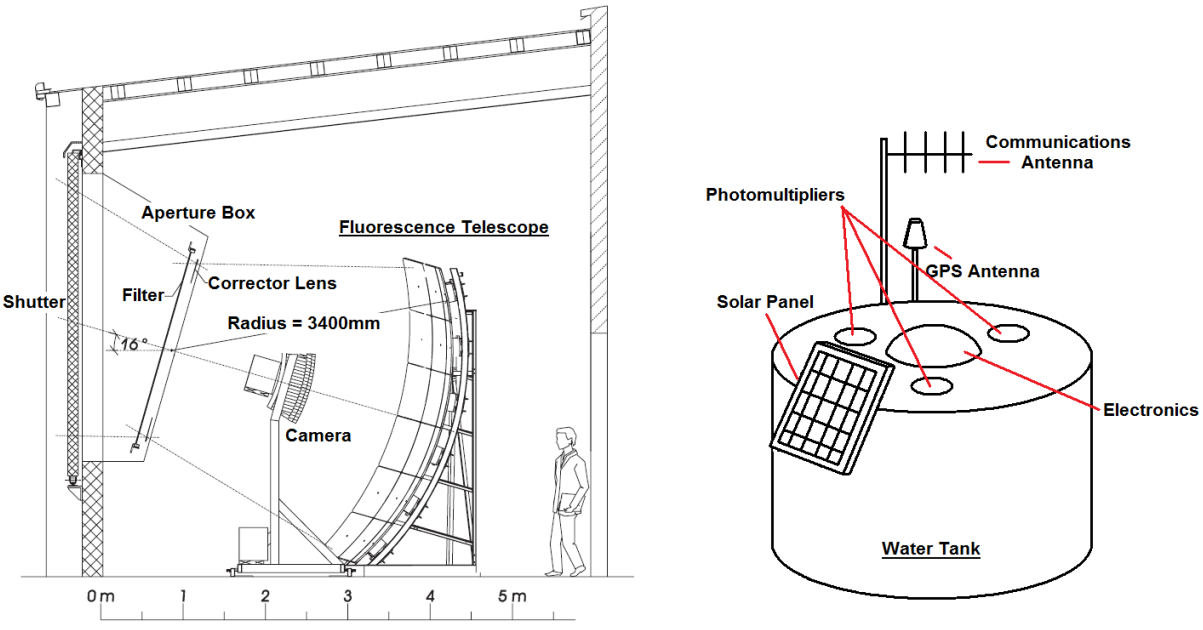

Figure 7: Schematic representations of a typical fluorescence telescope[7] (left) and a typical SD water tank (right).

to remain minimal. Therefore, the detector functions only during moonless nights with acceptable atmospheric conditions. This constraint reduces its maximal duty cycle to around 15%. Moreover, even when the requirements are met, the atmospheric conditions need to be constantly monitored in order to take into account their possible influence on the light propagation.

The FD `eyes` are situated in four different sites along the border of an area of roughly 3000 km^2 (see Fig. 8). Each building is oriented towards the inside of this area, overlooking it from a slightly higher level, on the top of small hills. The Surface Detector of the Pierre Auger Observatory is located in the area covered by the fluorescence telescopes.

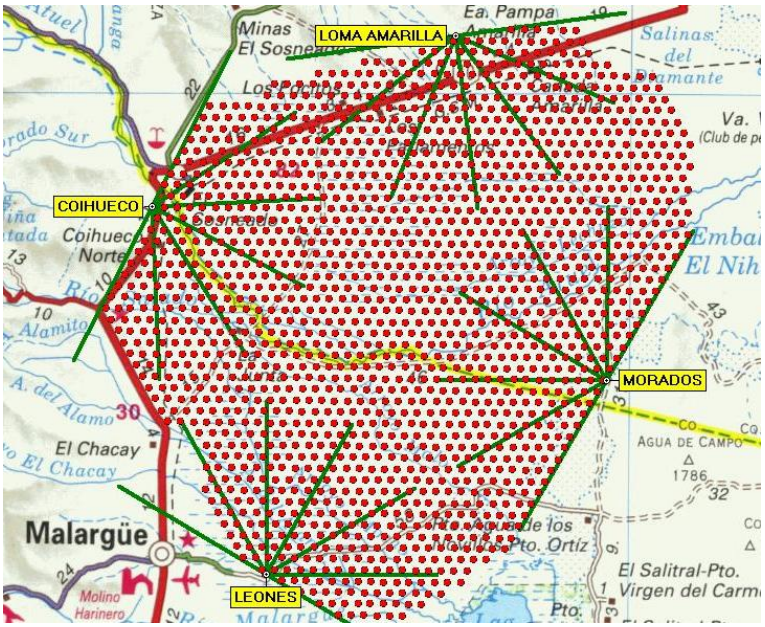

Figure 8: Locations of the Fluorescence Detector telescopes and the Surface Detector water tanks in the Pierre Auger Observatory [7].

1.2.2 The Surface Detector

Some of the particles produced in an extended air shower are unstable and decay after traveling only a few kilometers through the atmosphere. Neutrinos, on the other hand, are not easily detected. Muons constitute therefore, along with electrons/positrons, the main components of the showers at ground level that can be detected. As Pierre Auger demonstrated, the detection of these particles on the ground is another method for the detection of Extended Air Showers. By measuring the number of muons specifically, it is possible to establish the energy of the initial shower. The problem of this method lies on the reduced cosmic ray flux at these

energies, and the resulting rarity of such events. In order to detect showers caused by Ultra High Energy Cosmic Rays, a surface of thousands of squared kilometers is therefore required.

In the case of the Surface Detector, however, the measurement is not limited by external conditions such as weather or brightness of the sky, thereby achieving a theoretical duty cycle of 100%. On the other hand, it is not as accurate as the Fluorescence Detector, as it does not directly measure the shower profile, but only its remaining particles (muons). Hence, it is only possible to calibrate the data using simulations based on known models. These limitations provide examples of the compatibility and complementarity of these two detecting mechanisms.

For the Surface Detector, the Pierre Auger Observatory uses 1600 water tanks, equipped with three photomultiplier tubes each. The tanks are cylindrical, with a diameter of 3.6m and an height of 1.2m (see Fig. 7). Each one of the tanks contains therefore 12 m^3 of water in order to detect the Cerenkov-light emitted by the muons as they traverse them. The tanks are arranged in an array covering the 3000 km^2 surface in a triangle configuration, with a distance of 1.5 kilometers between every two tanks, as shown in Fig. 8. Besides the photomultiplier tubes, each one of the tanks also requires a number of additional components to collect and transmit the data. These are: a solar panel, to obtain the energy necessary for its function, a GPS and a communications antenna, to transmit its time and its data, respectively, to the nearest FD `Eye`.

In addition to the Fluorescence and Surface Detectors, other methods of shower detection are currently being studied. These include, for example, the detection of radio emission with the use of antennas [15], or the detection of large scale air ionisation with RADAR antennas [16]. These two phenomena can both be caused by EAS and are therefore to be considered indications of these events. The goal is to diversify as much as possible the methods by which the events are registered, in order to provide redundancy in the measurements, and eventually find better methods.

2 The HEAT enhancement

Besides the already operational baseline fluorescence telescopes, there are currently three complementary subdetectors under construction, called High Elevation Auger Telescopes [2]. Once finished, they will extend the energy range of the FD down to roughly 10^{17}eV.

2.1 Scientific Motivation

The Pierre Auger Observatory is currently in the final stage of its construction. The installation of the 1600 water tanks of the Surface Detector array and the 24 telescopes that constitute the Fluorescence Detector is now complete. With these two elements, the Pierre Auger Observatory is finally fully operational. However, the shower detection will only be completely unbiased for cosmic ray energies higher than $10^{18.5}$eV. For energies lower than this value, the event reconstruction could be biased and the statistics limited. An extension to lower energies would be interesting, as two important features of the cosmic ray spectrum are supposed to take place precisely in this range between 10^{17} and $10^{18.5}$ eV. The first one is the so called "second knee" of the cosmic ray spectrum and the second is the transition from galactic to extragalactic cosmic rays. Interestingly, a precise study of the composition in this energy range has yet to be performed by a major cosmic ray experiment. Therefore, with an adequate setup, it will be possible to test the existence of the transition by measuring the cosmic ray composition at these energies.

In order to understand the causes of the biased results for lower energies under the current configuration, an explanation of the calculations that lead to the identification of the shower composition is needed. The most important parameter for this measurement is the `mean depth of shower maximum`, or $\overline{X}_{max}$. X_{max} determines the maximum of the longitudinal profile of a shower (i.e. the number of particles versus atmospheric depth). For a constant energy, it fluctuates depending on the mass of the primary particle of the shower. By comparing the energy dependence of $\overline{X}_{max}$ with simulations, it is possible to estimate the proportion of lighter and heavier elements for showers with a given energy. This finally leads to the composition of the primary particles of EAS as a function of their energy.

However, at lower energies, the configuration of the current Fluorescence Detector setup imposes limitations on the reliability of the $\overline{X}_{max}$ analysis. These general limitations can be classified in four different categories:

1. Lower energy showers ($10^{17.5}$eV) produce fainter fluorescence light signals than higher energy ones, thereby decreasing the reach of their detectability down to a distance of only about 10 km. Therefore, lower shower energies automatically imply larger elevation angles.

2. For lower energy showers, the $\overline{X}_{max}$ ranges from 600 $\frac{g}{cm^2}$ for iron to 720 $\frac{g}{cm^2}$ for protons as primary particles. This corresponds to heights between 4200m and 8500m above the Auger surface array. This means that for showers in the low energy range, the maxima of their development takes place at higher altitudes. Hence, low energy showers (unlike higher energy showers, whose maxima are located much closer to the ground) are not always fully detected under the current FD setup.

3. Showers that move towards the Fluorescence Detector Eyes are difficult to reconstruct due to the time-compression of the signal measured by the photomultipliers. Additionally, nearby events typically have opposed properties. Both types of events are often discarded at trigger level.

4. The highly nonisotropic Cerenkov light emitted by EAS in forward direction increases the probability of an early triggering of the telescope for some geometries. This leads to a detection of the shower before its evolution reaches its maximum, thereby biasing the event reconstruction. This is mostly the case for low energy showers, where the Cerenkov light amounts to a large proportion of the measured signal. The result of this is a clear energy dependence in the accuracy of the X_{max} determination.

Showers whose maxima lie outside of the field of view of the telescopes are generally rejected. As a result of the limitations, this is more frequently the case for low energy showers. In order to achieve a totally unbiased analysis, an energy-dependent shower acceptance is to be avoided. A precise understanding of the causes of the limitations is therefore important.

Overall, the origins of these technical limitations can ultimately be traced back to the general disposition of the Fluorescence Detector telescopes. It imposes limits on the field of view, which under the current setup, only covers from 1 to 31 degrees above the horizontal (schematic representation shown in Fig. 9). As a result of this, there is an incomplete event selection that limits the statistics for these types of events and increases the probability of introducing systematic uncertainties.

2.2 Setup and Location

As stated above, the limitations causing difficulties for low energy showers originate mainly from the geometrical disposition of the telescopes. An expansion of the covered field of view would therefore provide a simple solution to the existing problem.

The High Elevation Auger Telescopes consist of three additional telescopes that will be installed near the existing FD eye at the Coihueco site (see Fig. 8). Instead of in the same building, the three telescopes will be placed in three individual shelters. The shelters will be located next to one another and separated by an azimuthal angle $\Delta\Phi$ of 36^o, as shown in Fig. 11. Each one of the telescopes will be mounted

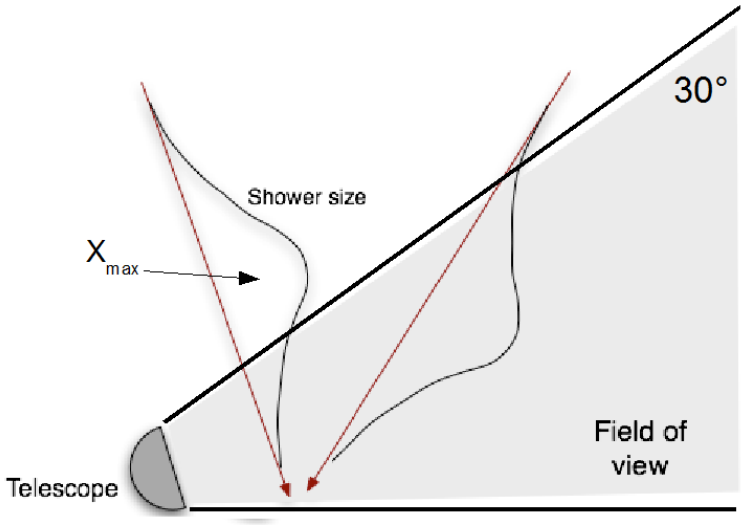

Figure 9: A simple example of the current limitations of the fluorescence telescopes that lead to systematic uncertainties.

on a platform which can tilt them 30 degrees upwards. This will expand the field of view from 0 to 60 degrees (see Fig. 10). All three telescopes will be installed on the downhill slope in front of the already existing Coihueco Fluorescence Detector. The Coihueco site is itself located on the top of a hill in the northwestern part of the Surface Detector array. Note that these three telescopes will function independently of the nearby Fluorescence Detector building, with no real time exchange of trigger information. The mechanical structure of the telescopes will retain exactly the same dimensions and elements as the 24 baseline telescopes, except for some minor modifications. These will mainly consist of special measures for a safer fixation of the different optical elements as well as the addition of the necessary structural components required to build a system with enough rigidity. All the optical parts and mechanics will remain basically unchanged. A HEAT telescope will also operate through the detection of fluorescence light emitted by the EAS, reflected by a $13m^2$ segmented spherical mirror and detected by a photomultiplier camera. It will only have two working positions, the standard horizontal one for installation, calibration, test measurements and maintenance, and the 30 degree up position for shower detection. The transition from one mode to another will be operated manually.

The new telescope shelters are basically made of three different structural components. First of all, the concrete foundation, that supports the tilting mechanics and provides stability for the whole building. Secondly, the strong steel base plate, filled with concrete, on which all the sensitive optical elements are fixed. Finally a relatively light-weight steel container encloses the optical components and electronics. The base plate is connected to the foundation, while the steel enclosure is itself fixed to the plate. Similarly to the baseline telescopes, a shutter system will

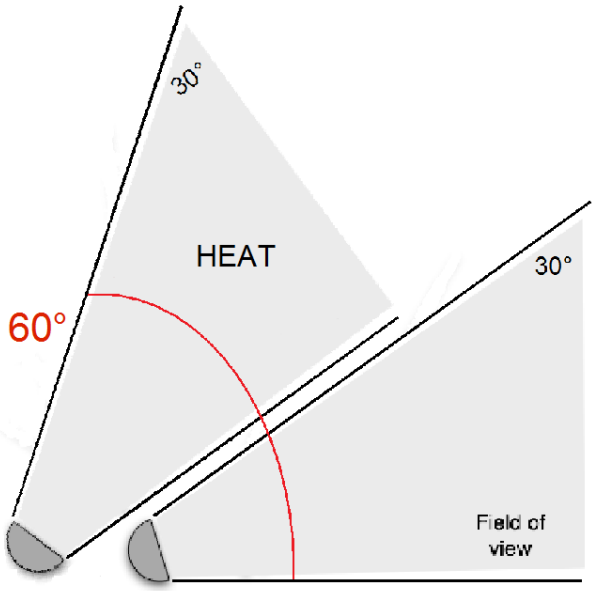

Figure 10: The solution offered by the High Elevation Auger Telescopes enhancement.

be mounted on the steel enclosure, but with a different design.

2.3 Expected Properties

For lower energy showers, according to the cosmic ray spectrum, the cosmic ray flux becomes significantly higher than for the currently analysed showers with energies above $10^{18.5}$eV. Consequently, the number of detectors needed to collect the same amount of data decreases for lower energies. Therefore, instead of adding another 24 telescopes with an elevated field of view, installing only three additional telescopes will suffice to improve the analysis in the low energy range.

As previously explained, the telescopes are separated by an angle of 36 degrees. This value was chosen based on simulations that were performed to calculate the spacing, for which the telescopes would cover the most useful field of view [2]. This scan of the azimuthal separation was implemented for an angular range from 30 to 60 degrees (see Fig. 12). The acceptance and detector resolution were then extrapolated for these different setup possibilities. An azimuthal angle of $\Delta\Phi = 36^o$ was finally chosen, as this was found to be optimal. The resulting simulation of the field of view for this optimal azimuthal angle can be seen in Fig. 13. Note that the increase of the curvature of the field of view for higher elevations, shown in Fig. 12 and 13, is a purely geometrical effect.

In order to understand the improvement of the analysis as a consequence of the

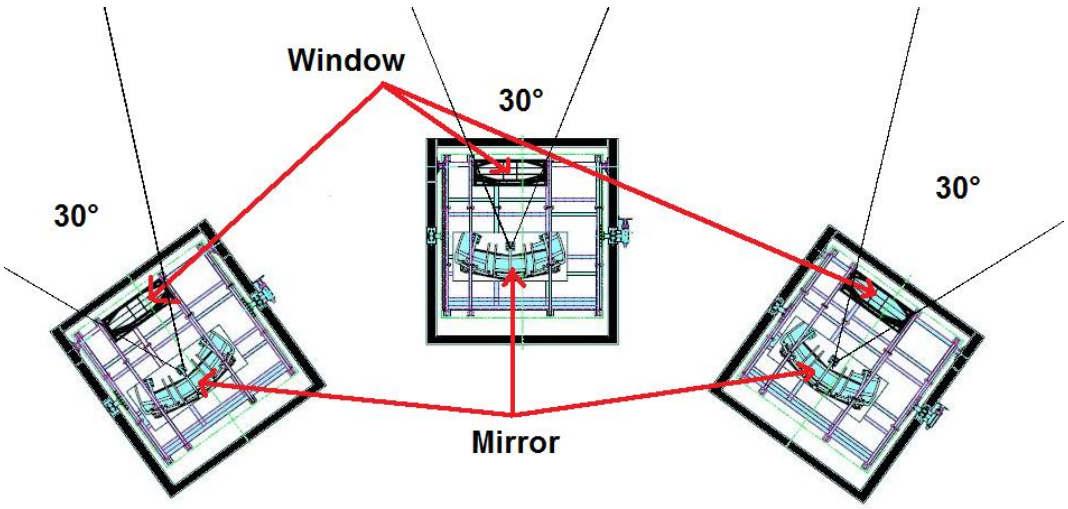

Figure 11: Geometrical disposition of the three HEAT shelters, with a separation angle of 36 degrees and a field of view of 30^o per telescope.

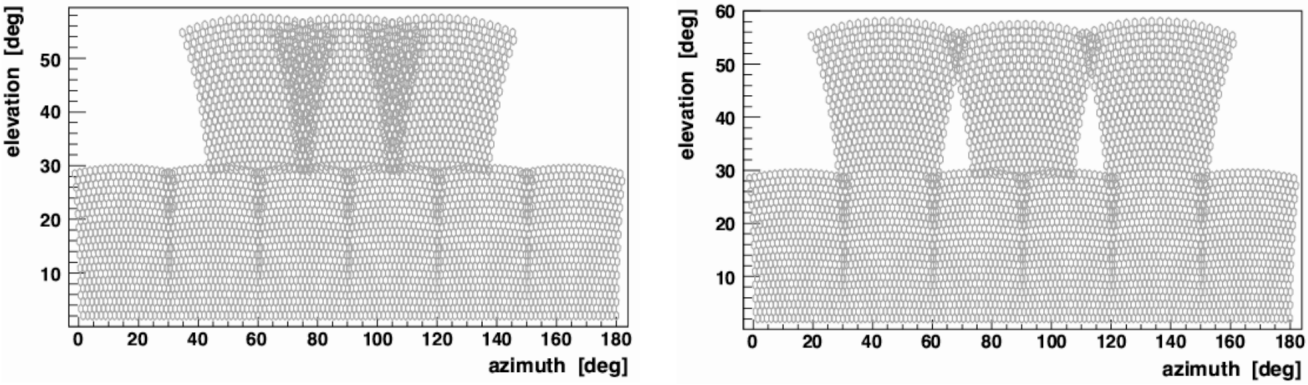

(a) $\Delta\Phi = 30^o$ (b) $\Delta\Phi = 45^o$

Figure 12: Field of view simulations (a) for a 30 degree azimuthal angle and (b) for a 45 degree azimuthal angle.

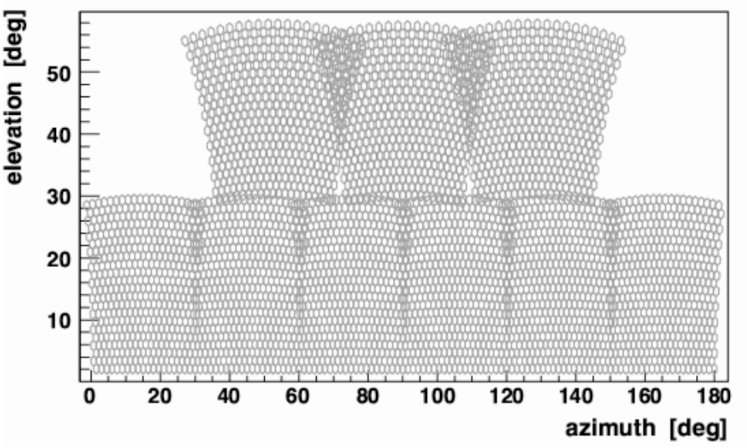

Figure 13: Simulations indicate an optimal azimuthal angle for 36 degrees.

elevated field of view, shower detection simulations [13] reflecting the performance under the enhanced setup were carried out.

To reconstruct the geometry of a shower, the first step is finding the Shower Detector Plane (SDP), which is defined by the detector and the shower axis (see Fig. 14). The geometrical parameters that describe the shower in the SDP are: the distance between the shower and the detector R_P, the time when the minimum distance is reached t_0 and the angle between the shower and the ground χ_0. According to the geometry, in order to determine these three parameters, the function 9 is then fitted to the measured data, where $t(\chi)$ corresponds to the hit time for an inclination χ.

$$t(\chi) = t_0 + \frac{R_P}{c} \cdot tan(\chi_0 - \chi)^2/2 \tag{9}$$

Figures 15 and 16 show the process for a simulated shower with an energy of $E = 10^{17.5}$eV and whose center lies at a distance of D=1.2km of the fluorescence telescopes. Such a close-by, low energy shower would typically be incorrectly reconstructed with the current Fluorescence Detector setup, given that it would not cover the maximum of the dE/dX profile. This would, however, not be the case with HEAT, as Fig. 16 shows an optimal profile reconstruction as well as an optimal X_{max} determination. Simulations were also carried out for the detection of other types of showers with greater energies and distances (for which the HEAT enhancement was not particularly intended) with consistently positive results.

The "elongation rate" describes the variation rate of the mean depth of shower maximum $\overline{X}_{max}$ with energy. This parameter also benefits greatly from HEAT. Fig. 17 displays the comparison between the simulation results for proton and iron induced showers with and without the expanded field of view. In this diagram the difference between both setups becomes clear. While the enhanced reconstruction remains

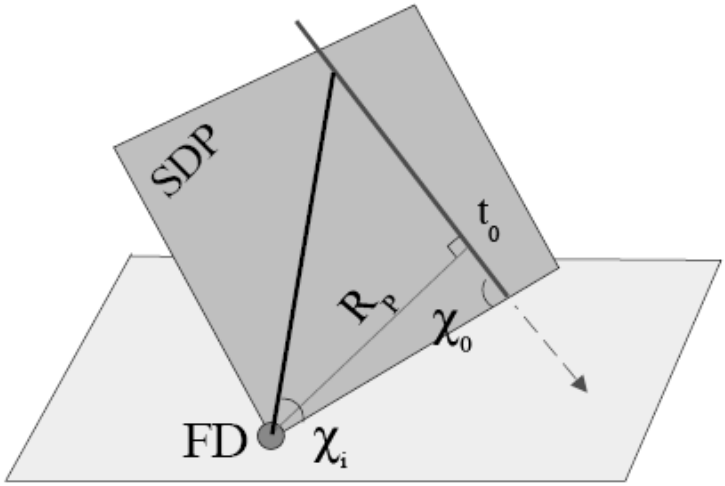

Figure 14: The geometry of the shower reconstruction, adapted from [8].

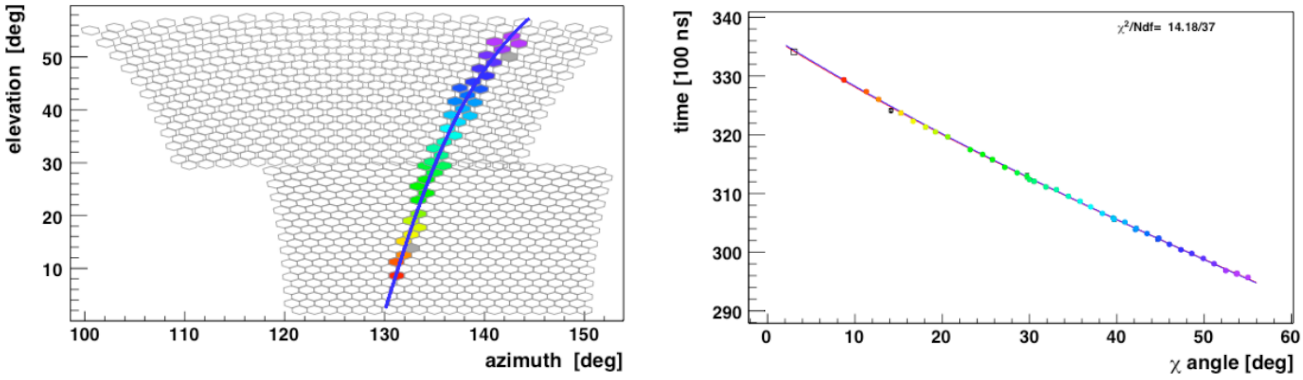

(a) Shower detection simulation, $E = 10^{17.5}$eV and D=1.2km

(b) The "Time Fit".

Figure 15: Example of a simulated close-by low-energy event and its reconstruction with (a) the shower trace in the shower detector plane and (b) the reconstruction of the Time Fit, where arrival time is plotted against inclination. In both cases the different colors indicates the pixel detection time (violet≡early, red≡late).

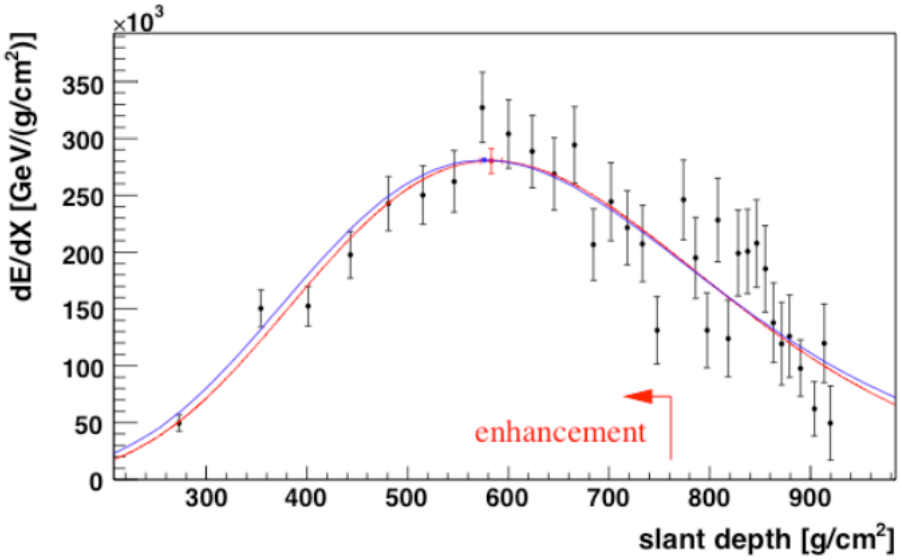

Figure 16: dE/dX profile of the aforementioned event. The generated curve is shown in blue, while the red line displays the Gaisser-Hillas profile. The red arrow indicates the region of the profile that would be measured by the HEAT enhancement.

consistent with the generated data down to even 10^{17}eV, the current reconstruction displays discrepancies for energies lower than $5 \cdot 10^{17}$eV. This creates a biased sample with higher $\overline{X}_{max}$ values and favors lighter elements as primary particles.

Both energy and angular resolution constitute important properties of a cosmic ray detector. The width of the X_{max} distribution is, along the average value, an indicator of the primary mass of an extended air shower. This fact renders an optimal energy and X_{max} resolution of the fluorescence detector desirable for this observatory. The analysis indicating both energy and X_{max} resolutions, for current and extended setups, is shown in Fig. 18. Once again, the improvement that results here is clearly visible, especially for lower energies.

The results of the study of the expected properties of HEAT validate the installation of an enhancement as a useful addition to the observatory. The simulations not only demonstrate this, but also confirm its necessity in order to have unbiased results down to roughly 10^{17}eV and a better shower reconstruction altogether. Every detector attribute, from acceptance to elongation rate and resolution, improves significantly as a result of such an enhancement. This happens not only for low energy EAS, but for higher energy showers as well.

2.4 Status of HEAT

Currently, the HEAT site remains under construction [28]. The site preparation is on schedule and making good progress. The foundations for the three telescope

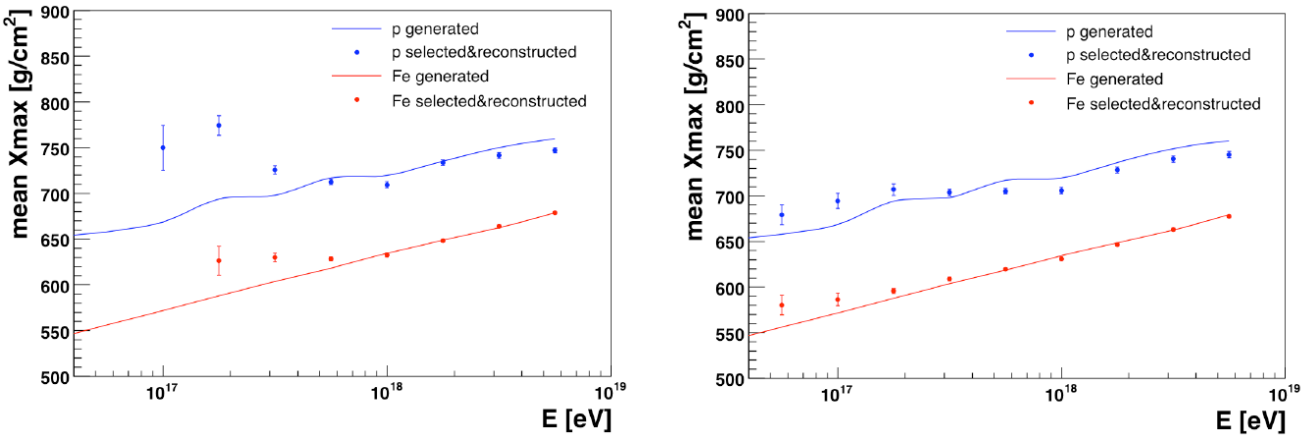

(a) Current elongation rate (b) Enhanced elongation rate

Figure 17: Elongation rates (a) measured and reconstructed for proton and iron particles, for the existing setup, (b) for simulated and reconstructed events, after the enhancement.

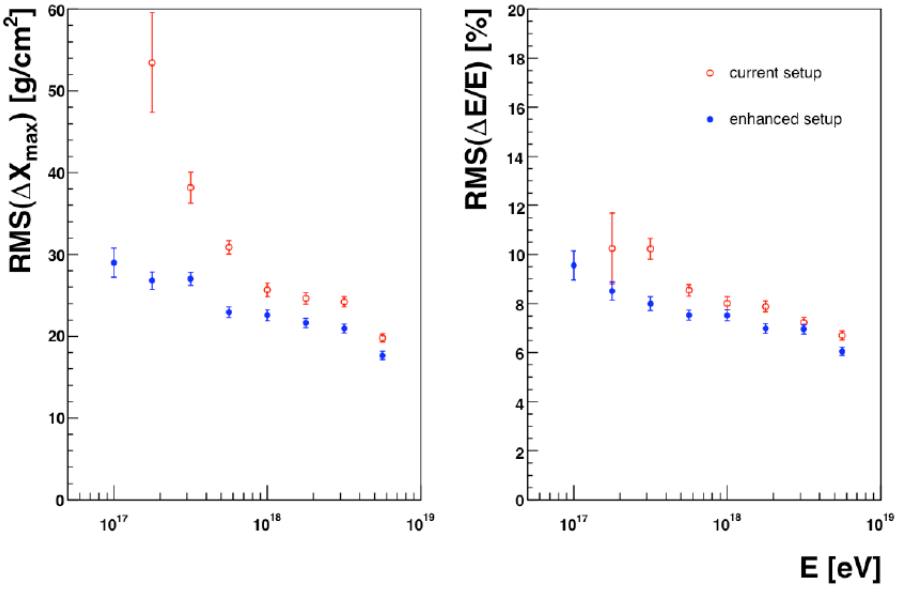

Figure 18: X_{max} and energy resolution of current and enhanced setups.

enclosures were finished in February 2008. The installation of the tilting mechanics and the base plates has already begun. Pictures of the construction site can be seen in Fig. 19. In addition, electronic components for the HEAT telescopes were already shipped to the site from Germany. It is anticipated that the HEAT enhancement will be operational by the end of 2008.

Figure 19: Foundations of the three HEAT telescopes.

2.5 Complementarity with Infill Array

In addition to HEAT, a second enhancement for the Pierre Auger Observatory is currently under construction [29]. A denser array (infill array) of water tanks, called AMIGA (Auger Muons and Infill for the Ground Array), is being installed in the field of view of the new enhancement telescopes. Once finished, it will consist of a 23.5km^2 array of SD detectors with spacings of 433m and 750m and buried muon scintillator counters. These detectors will complement the fluorescence measurements: the water tanks will allow the hybrid technique to be used for low energy showers and the muon detectors will be used to gain information on the mass composition. Combined, the properties of both the HEAT and AMIGA enhancements will offer a complementarity that will significantly reduce the current uncertainties at lower energies, especially for nearby events.

2.6 Challenges

Although the installation of three additional telescopes appears to have no evident drawbacks, there are some minor difficulties that have to be kept in mind. Other than the necessary structural modifications in the building, the telescopes will not be different from the currently used ones. This means that camera, mirror and electronics have to be identical in all fluorescence telescopes. This poses a problem in that these components were not initially conceived for this purpose (i.e. for being tilted up to 30 degrees from the horizontal). Even though the heavy base plate

and the strong fixations are designed to provide enough stability for the shelter in all possible conditions, the same does not necessarily hold for both mirror and camera. Additionally, due to the sensitivity of all components and their calibrated positioning for optimal optical properties, even the slightest alteration could be the cause of significant inaccuracies in the shower reconstruction.

3 Objectives of this diploma thesis

In order to ensure the functionality of the HEAT telescopes and test their stability, this task intends to set the basis for the design and operation of an inclination monitor. Its objective is to study the dynamic behaviour and detection of possible distortions of the telescopes inside the shelter when it is tilted or subject to strong winds and other environmental fluctuations.

The ultimate goal is to measure mechanical deformations with a great precision, either to prove the feasibility of this project or to manifest the need for corrections. For the telescopes to be viable, the measured variations must remain within certain tolerances. If it were discovered that the fluctuations did in fact exceed said tolerances, a number of measures would then be undertaken to minimize them. The stability could, for example, be improved with the installation of additional fixations connecting the mirror with the camera.

The tolerances in question are listed below in table 1. These were defined based on the work done by M.Palatka [10] on the uncertainty of the position of the telescopes. The determination of the uncertainties are based on raytracing calculations and simulate the effect of different deformations on the geometrical properties of the telescope. The results of these exhaustive calculations attribute a particular importance to the camera-mirror distance. The distance between the mirror and the shutter, while still important, is not as critical.

The inclination tolerance is also based on the typical camera misalignment for the baseline fluorescence telescopes. These misalignments lead to angular offsets of roughly 0.1^o in the absolute telescope pointing. This value constitutes a reference for the misalignment of the current telescopes and can, therefore, be taken as a limit for the inclination uncertainty of the the HEAT telescopes. The typical offsets were at first estimated using star image methods and were later confirmed by the geometry reconstruction of laser shots from the Central Laser Facility of the observatory [14].

These maximal values are to be considered the maximal deformation that are allowed to occur as a result of the inclination of the HEAT shelter. For higher variations, it is not guaranteed that the telescopes will properly reconstruct the shower events without any bias. The goal of this task is to ultimately determine the real variations with an accuracy ten times better than the corresponding tolerance.

Unfortunately, due to several unexpected difficulties, the construction of the HEAT enhancement telescopes was delayed for a number of months with respect of the original schedule. One of the consequences of this delay was that the new telescopes were not finished in time for this diploma thesis to be able to provide monitoring

Parameter	Tolerance
Camera-Mirror Distance	0.5 mm
Shutter-Mirror Distance	5 mm
Optical Axis Inclination	0.1^o

Table 1: List of calculated tolerances for the mechanical deformations of the optical components of the HEAT telescopes.

data from the telescopes themselves. However, it was possible to test the inclination monitor in one of the already existing Auger fluorescence telescopes. The Fluorescence Detector building located in Los Leones (see Fig. 8) was used for this purpose.

Evidently, in this location, the monitoring system does not measure fluctuations caused by the tilting of the telescope, as there are none. Besides, strong winds are not expected to cause a significant effect, since the telescopes are located in a bigger and more robust concrete building, as opposed to the smaller steel shelters from HEAT. However, the test remains a useful reference measurement nonetheless. As a last precaution, once the monitor is installed, a manual deformation of the different components of the telescope structure was finally performed to evaluate the sensitivity of the system.

Performing test measurements in an existing fluorescence telescope is a sensible precaution. It proves the ability of the system to acquire and transfer useful data, ensuring that it is in fact ready for its original purpose.

4 The Tilt Monitor

The system that will be used to accomplish the objectives discussed in the previous chapter is called the "Tilt Monitor". This monitoring system consists mainly of a series of accurate though relatively simple sensors. After consideration of a variety of possible methods, taking into account advantages and disadvantages of every possible strategy, it was decided to adopt mainly two types of sensors. The first type are the inclination sensors whose task is to measure the inclination variations at different points inside the HEAT shelters. The second type will measure the distance variations between the optical components of the telescope. The distance sensors will not only measure the long term variations but also the higher frequency variations that could take place in the telescope when subjected to strong winds or other similar conditions.

Simultaneously, a weather station was included to monitor the weather conditions. This will provide the necessary information in order to correlate distance and inclination fluctuations with possible weather patterns.

Finally, the data acquisition system for this monitor consists basically of a LabVIEW equipped laptop and an external Analog to Digital converter (ADC). The ADC converts the analog signal of the distance sensors into a digital output compatible with the data acquisition from LabVIEW. The inclination sensors do not need any ADC, as their output is already digitized. With this system, it was possible to use standard USB connections for all measuring tasks to simplify the monitoring process.

4.1 Inclination Sensors

The Tilt Monitor features a total of four small biaxial inclination sensors. They are based on the so called MEMS (i.e. Micro Electro-Mechanical System) technology. There are currently two main types of MEMS-based inclination sensors: capacitive and piezoresistive. In this case the sensors are capacitive, meaning that they use a micromachined silicon capacitive transductor, consisting of two fixed capacitor plates and a seismic mass located in between. Tilting the sensor causes movements in the position of the seismic mass. The resulting changes in the capacity reflect then the inclination of the sensor (principle shown in Fig. 20).

The model used for this task is the DAS-15-MC-RS232 inclinometer from Sensor Systems shown in Fig. 21. There is one sensor for each of the following components of the telescope: The mirror, the camera, the shutter and the ground plate.

As mentioned before, the signal output they provide is already digitized and precalibrated. It remains, however, not accurate enough for the purposes of this task. Therefore, in order to improve the accuracy of the data, the sensors were recalibrated

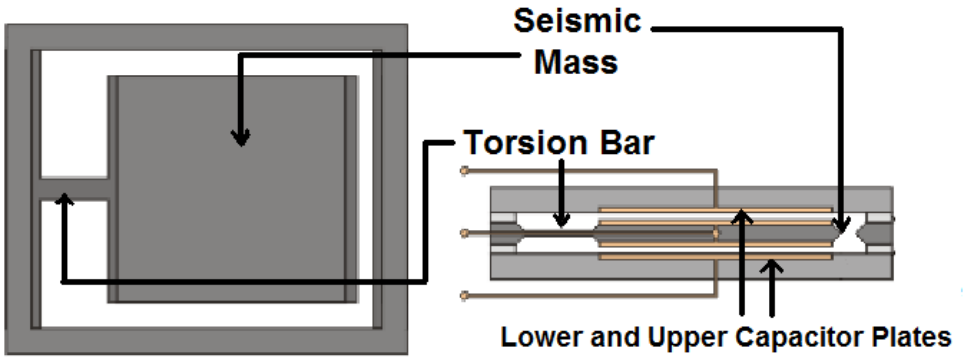

Figure 20: Working principle of a MEMS-based capacitive inclination sensor, adapted from [24].

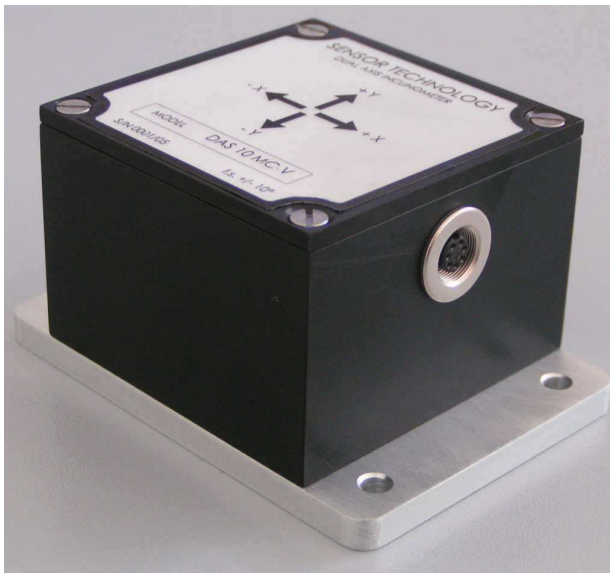

Figure 21: Inclination Sensor DAS-15-MC-RS232.

(see chapter 5). As for the maximal resolution of these inclinometers, the digital 12 bit data output provides inclination information for up to one hundredth of a degree. Although the official range of the sensors lies between -15 and 15^o, it was possible to obtain stable results for inclinations up to even 20 and -20^o. Note that even though the sensors are supposed to automatically correct temperature related effects, it turned out they appear to remain temperature sensitive.

Finally, the connection of the sensors uses a 6 pin output socket with an RS-232-TTL communication protocol and requires a 9V supply voltage input. The power supply was provided with an external AC/DC converter.

A subsystem of very accurate distance sensors form also part of this monitor. Specifically, it includes four potentiometers with a theoretically infinite resolution. Their task is to measure the distance variations between the different optical components of the telescope (see Fig. 22). The distance between the mirror and the camera is covered by three of them, with the fourth one measuring the distance between the shutter and the mirror. The model used for this task is the PTX-101 potentiometer from Celesco.

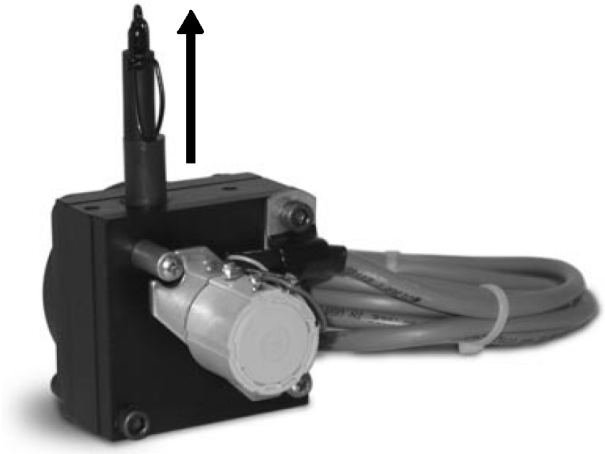

Distance Sensor PTX-101.

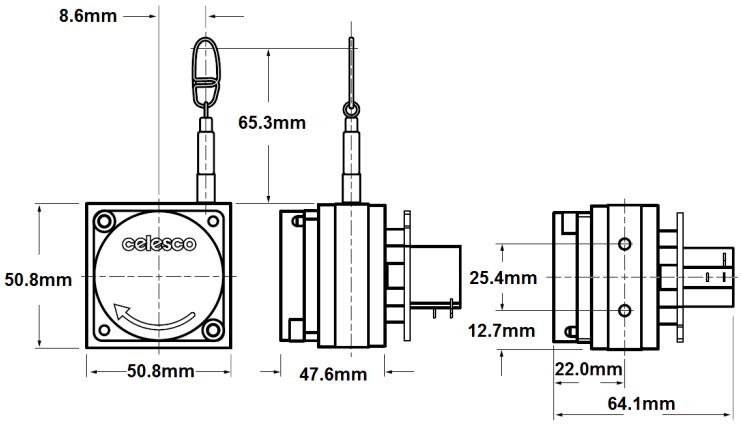

Detailed view of the potentiometer with exact dimensions.

Potentiometers, or cable-extension transducers, provide a voltage feedback output proportional to the linear movement of their attached extension cable. By pulling the cable from the sensor and measuring the resulting voltage variation it is possible to determine distances with a high accuracy. Note that a spring pulls the cable back into the sensor with a force of roughly 15N.

The cable length and thus the measuring range are typically inversely proportional to the accuracy (i.e. better accuracy with shorter range). Therefore, the use of potentiometers with larger cable lengths was ruled out. In order to achieve the required

accuracy of (at least) 0.5mm, it was only possible to use sensors with ranges of only a few centimeters. Evidently, with that cable length, it is not possible for them to measure the much larger absolute distances between the optical components. We therefore attached the sensors to long and very thin carbon fiber cables, allowing them to enlarge the distance. This way, the sensors record the distance variations between two objects at greater distances. The carbon fiber wires remain stable with their lengths practically unchanged under temperature fluctuations due to the negligible elasticity and thermal expansion coefficient of the material. Ultimately, measuring the absolute distances with the same accuracy would have resulted in a considerably more expensive system.

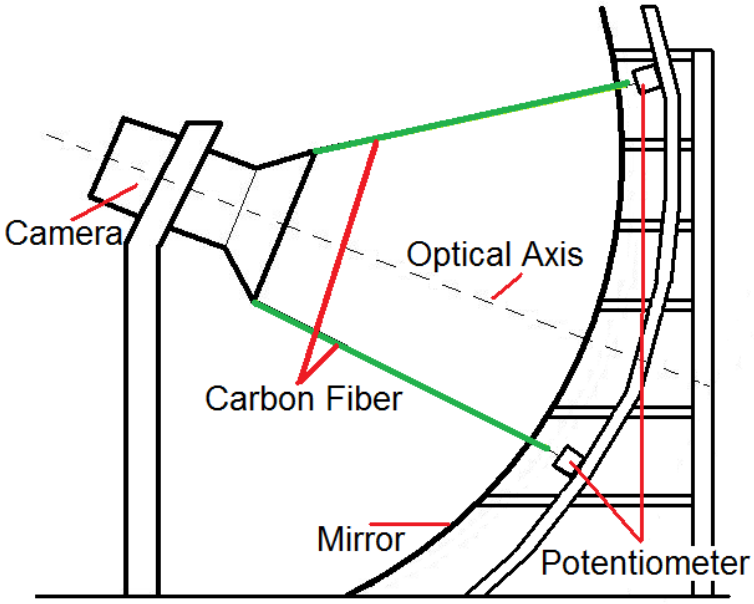

Figure 22: Setup for the distance sensors in an actual fluorescence telescope. Due to the limited range of the potentiometers, long carbon fiber cables were attached to the sensors to measure the relative variations in distance.

The transducers' connection socket is a simple 3 pin connector. One pin corresponds to the voltage supply, another to the voltage output and the last one to the ground connection. Unlike the inclinometers, the output of the sensor is not automatically digitalized. The sensors provide a signal in the form of an analog voltage. The output voltage varies linearly with the extension cable lengths and must be converted into a digital signal with an ADC before being read out with LabVIEW. The sensors require a 5V DC supply, which was provided with another AC/DC converter.

One advantage of this model over other alternatives is its temperature independence, which notably simplifies the subsequent data analysis.

4.2 Weather Station

The third and last measuring component of the Tilt Monitor is the weather monitoring station, whose function is to track weather fluctuations and their influence on the stability of the telescope. Taking into account the fact that there is no need of an extremely elaborated weather monitoring, the choice was made for a fairly simple commercial weather station. The exact model is the NEXUS weather station from the company TFA displayed in Fig. 23. It includes three wireless temperature sensors and hygrometers as well as one inside the basis station, a barometric pressure sensor, a wind velocity sensor and a rain quantity sensor. For a more detailed information about the range, resolution and accuracy of each component of the weather station, a list containing most of the technical specifications provided by the manufacturer is shown in table 2.

Figure 23: TFA NEXUS weather monitoring subsystem, complete with base station, external thermometers/hygrometers, wind speed and rain sensors.

The base station as well as the wireless temperature sensors were installed inside the telescope shelter, while the rain and wind speed sensors were placed on its roof. The three wireless thermometers measure the temperature changes on three different levels, the mirror, the camera and the ground plate, thus determining the temperatures around the inclinometers. They are operated by two standard AA batteries each and have, according to the manufacturer, an autonomy of 6 months.

Note that only the standard transmission frequency of 433 MHz is allowed in Argentina and in Germany. Therefore, this model was chosen in order to comply with argentinian regulations.

The station is equipped with an interface that connects to the PC via a standard

Parameter	Range	Resolution	Accuracy
Temperature (internal)	$-10^o..60^o$C	0.1^oC	$\pm$ 1^oC
Temperature (wireless)	$-40^o..80^o$C	0.1^oC	$\pm$ 1^oC
Humidity	0..99%	1%	$\pm$ 5%
Barometric air pressure	500..1100 hPa	0.1 hPa	$\pm$ 3 hPa
Wind velocity	0..200 km/h	0.1 km/h	$\pm$ 3 km/h
Rain quantity	0..2000 mm	0.1 mm	-

Table 2: Technical information concerning the NEXUS weather station.

USB cable. A software package with drivers and a data analysis program is also included with the station.

4.3 Software and Data Acquisition

The central assignment of the data acquisition system system (DAQ) must be fulfilled by a computer. A standard notebook PC with Windows XP as the operating system was used for this task. The computer model is an ACER Travelmate 290 with a 1.3GHz Pentium M processor and 1GB RAM memory. Additionally, the PC provides an ethernet connection and 3 different USB ports. With dimensions of 33.3cm×27.7cm×3.3cm it contributes in reducing the space needed for the monitor.

Along with the computer, other important DAQ hardware components include:

- An ADC to convert the analog signal data provided from the PTX-101 sensors into a digital signal compatible with LabVIEW.
- A RS232 to USB serial converter, to transform the four digital signals provided from the inclinometers into a single USB connection.

As for the software, from the beginning of the project it was decided that LabVIEW was the best option, due to its adaptability and multiple applications in the field of sensor technology. With the use of LabVIEW, the purpose was to create a single program capable of collecting data from all the sensors in perfect synchronisation and write it in a single file. The acquired data is then to be transfered from the location of the telescope in Malargüe, Argentina, to the RWTH in Germany for further analysis. The transfer was set up using a built-in function of LabVIEW.

4.3.1 MicroBOX Analog-Digital-Converter

The company that provides both the inclination and distance sensors, Disynet, also offers a digitization device. It is called microBOX, and was especially designed to function with a wide range of sensors, including the ones used for the Tilt Monitor.

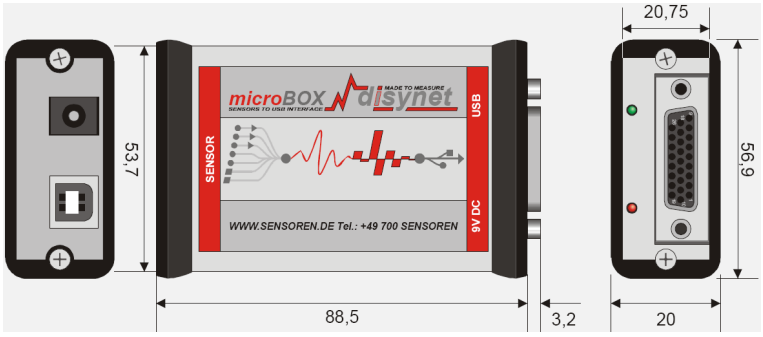

Figure 24: Analog-Digital-Converter microBOX from Disynet.

This device has the capacity to simultaneously connect to up to five analog sources and two additional digital ones and can be read out over USB. It connects then via a standard USB cable to the computer. Furthermore, not only does the USB connection suffice to supply the microBOX with the required voltage, it can also be used as the power input to the potentiometers (provided the consumption is not excessively high). The microBOX also provides an additional connection for an external power supply. The ADC operates with acquisition rates of up to 25kHz and features a 20 Bit resolution for the data conversion, which implies digitizing the signal in over one million steps. Note, however, that the maximal resolution mode is not compatible with the maximal 25kHz acquisition rate. Lastly, the microBOX uses an integrated amplifier to accept signals from 10mV to 10V for three of the analog input channels.

The use of LabVIEW was a suitable choice for the readout software, as the MicroBOX is equipped with its own LabVIEW-compatible drivers. This allowed the development of custom software using already existing packages and the compilation of executable files based on this software.

Finally, a connection box was produced in the Electronics Workshop of the III. Physikalisches Institut of the RWTH. It permits an easier connection between the sensors and the microBOX, as it allows for space to configure the cable connections while remaining reasonably compact at the same time.

4.3.2 RS232 to USB serial converter

Finally, a RS232 to USB serial converter completes the hardware equipment of the Tilt Monitor. It collects the RS232 output from the inclinometers with its four SUB-

D sockets and sends it in a standard USB output to the computer. The computer then interprets the signals of the four inclinometers as four separate serial port COM interfaces. The advantage of this is clear: instead of using four different ports, the device results in the implementation of only one physical USB port. This contributes to the overall uniformity of the connections. Much like for the ADC, an external power supply can be plugged into the converter to provide extra voltage. However, this is not needed, since the power supply of the USB connection provides enough voltage. This is not the case for the inclination sensors, which have to be powered by an external power supply.

4.3.3 LabVIEW Software

Concerning the code specifically implemented for the Tilt Monitor, the main objective was to create a stable, complete and relatively simple software. Its task should be to collect and send as much information as possible, while still keeping the size and transfer rate of the files manageable. The restraint on the size of the data is the result of the limited network capacity avalaible in the FD site.

The LabVIEW-based software is divided into two different applications called "TiltMonitor.exe" and "DataTransf.exe". "TiltMonitor.exe" includes the code for the data acquisition of the eight sensors as well as the data extraction of the weather station. "DataTransf.exe" is then used to compress the data from every sensor into one single ZIP-file and send it via e-mail to an account from which it can be extracted.

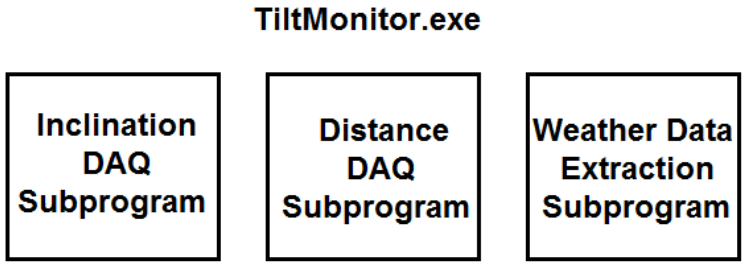

Figure 25: Organizational chart of the TiltMonitor.exe executable file.

The TiltMonitor.exe program is itself composed of three parts or subprograms, each one dealing with one type of sensor (see Fig. 25). The first subprogram, which collects the inclination data, uses four different timed loops for the four different inclinometers. Inside the loops, the previously configurated LabVIEW "Instrument Input/Output Assistant" extracts the data for both X and Y axes at the rate of 4Hz in the form of two different strings and sends it to the String-to-Double conversion function. The data is then finally saved as a LabVIEW Measurement File (.lvm) using the "Write to Measurement File" Labview program. LabVIEW subprograms

are also called VI, which stands for "Virtual Instrument".

The process is exactly the same for the four inclinometers, with each sensor being acquired by a different function in different loops. The reason that the sensors are not read out in a single loop is that each one of them digitizes by its own clock cycle. A readout in one loop would therefore cause a significant unsynchronization of the signal.

A chart displaying the structure and execution of the process can be seen in Fig. 26, with more detailed block diagrams from the LabVIEW code being shown in the appendix of this document.

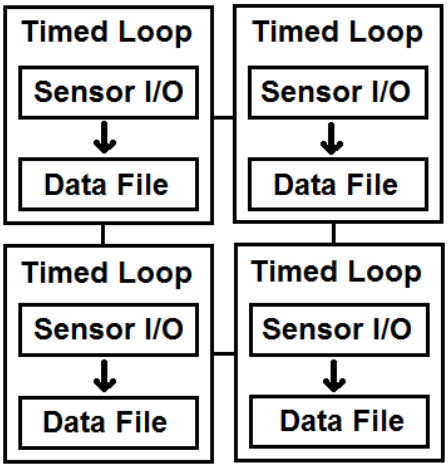

Figure 26: Block diagram of the inclination DAQ subprogram.

The second part of the program, dedicated to the distance measurements, is conditioned by the use of the Analog-Digital-Converter. The supplied drivers for LabVIEW determine the form in which the data is acquired (note that these drivers, implemented in the form of subVIs, were the only part of the LabVIEW code provided by Disynet).

After the initialization of the ADC, the subprogram uses a while loop to collect samples of data for every iteration. Firstly, the provided RealTime function has to be be enabled for each iteration. Then the GetRealTimeSampleBuffer function extracts a sample containing typically 1000-2000 values and stores them in a buffer. The content of the buffer is then filtered to eliminate possible peaks in the data caused by electrical instabilities in the ADC. Were these not filtered, it would then lead to an eventual bias in the sample. In order to optimize the accuracy of the data, the average value of the sample is calculated and stored in a LabVIEW measurement File. This leads in turn to a loss in the time resolution, but also contributes in reducing the overall size of the data.

However, in order to have at least a minimal measurement with a higher time resolution, the raw buffer data is still stored in a separate file every 300 iterations. The length of the buffer can then be fixed by setting the exact duration of each iteration in the final step of the loop. The standard value for the duration was set to one second. A schematic block diagram of the subprogram is shown in Fig. 27.

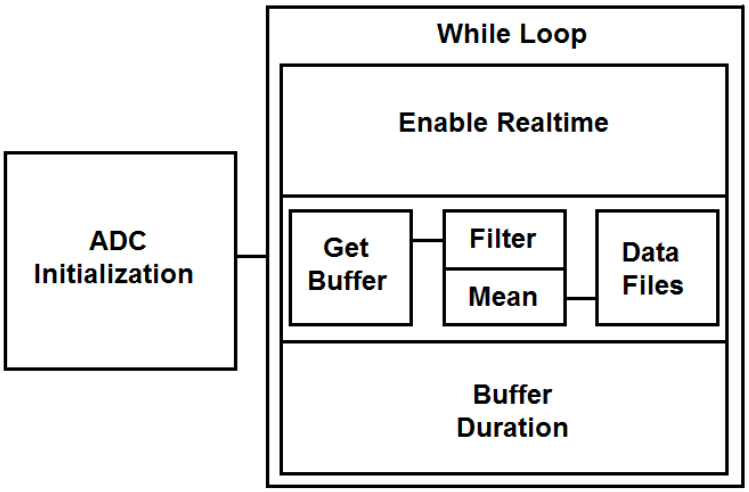

Figure 27: Block diagram of the distance DAQ subprogram.

The commercial weather station is built and configurated in an hermetic way that did not permit to create custom software capable to collect the data without the help of the supplied program. Therefore, there is no real data acquisition, since the data is already collected and stored in an Excel-like file via the station's own software. However, under the original format, the data is almost unusable and packed with excessive information. Moreover, the station only stores up to roughly 3000 lines of data and overwrites previous data after this amount is exceeded. It was therefore essential to find a way to continually extract the raw data and save it in an appropriate form. The subprogram corresponding to the weather station uses a timed loop to collect the data. In addition, it also employs the read_excel_values.llb library from LabVIEW to extract the data from the Excel files, as shown on the detailed LabVIEW block diagram located in the appendix. This library is not part of the base package, it is however avalaible from the National Instruments website. The program is synchronized so that it is able to choose the correct values in the Excel File and store them in a compact LabVIEW measurement file. Concerning the acquisition rate, the program is limited by the sampling rate of the weather station, which only allows up to one measurement per five minutes. A simplified block diagram of this subprogram can be seen in Fig. 28.

The size of the data files is also an important issue. The use of larger files would not

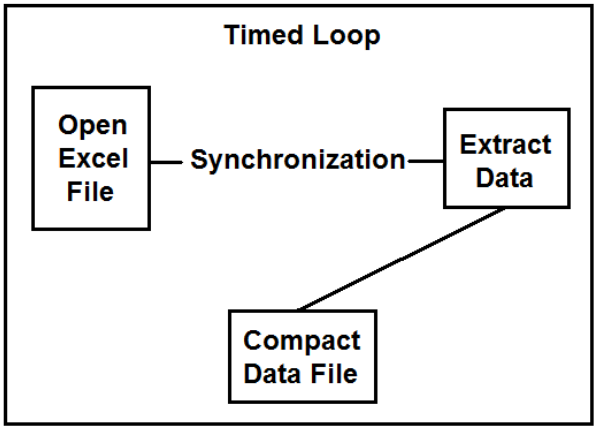

Figure 28: Block diagram of the weather DAQ subprogram.

only slow down the program but also eventually cause errors. To avoid this, every subprogram was designed to start writing the data on a new file every hour, limiting their size and making them more manageable. The typical size of a single file from an inclinometer does not exceed 700 kB. The normal size of an hour worth of data from one potentiometer is roughly 72 kB. Lastly, the size of the weather data is, due to the slow acquisition rate, almost negligible (<1kB).

The execution of the TiltMonitor.exe application opens a window with the front panel of the LabVIEW program (see Fig. 29). This front panel is divided into two tabs, the first one called "Distance, Inclination and Weather Sensors" displays the last 15-20 minutes of collected data from all sensors (including the weather station) in 15 different charts. The two charts situated on the top left side of the window show the distance measurements, with the data for the three mirror-camera sensors being shown on the top and the data from the mirror-shutter sensor on the bottom. Meanwhile, the inclination information is spread into eight different charts, each one for one of the two axes of each inclinometer. Lastly, the lower part of the window displays the weather data in five separate charts (for the four temperatures, humidity, air pressure, wind and rainfall, respectively). The second tab entitled "Configuration" was added to adjust the different parameters of the data acquisition setup, such as the resolution, range and gain of the input channels of the ADC.

The data must not only be collected, but transferred, so that it is accessible from the RWTH in Aachen. Hence, the second program "DataTransf.exe" was created. It basically consists in a Timed Loop which repeats a sequence of two actions every hour. The first one identifies the correct LabVIEW measurement files and compresses them into a single ZIP-file, thereby reducing the required disk space from roughly 3 MB to 700 kB. The second attaches the compressed file to an e-mail and sends it to a previously defined account.

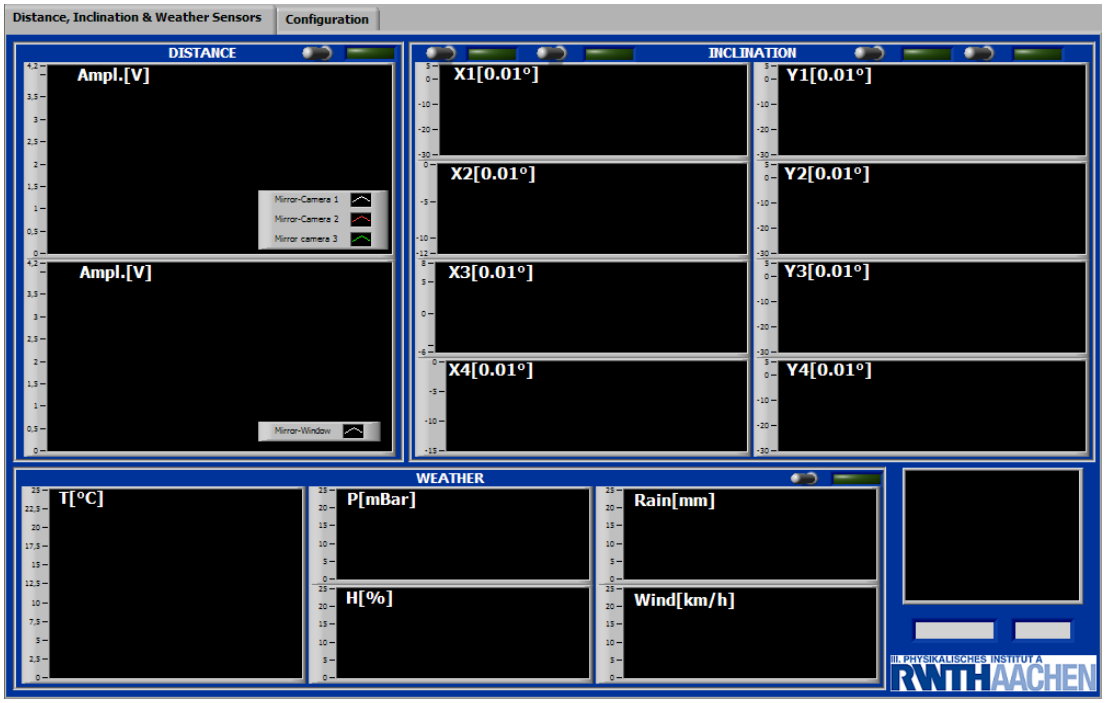

(a)

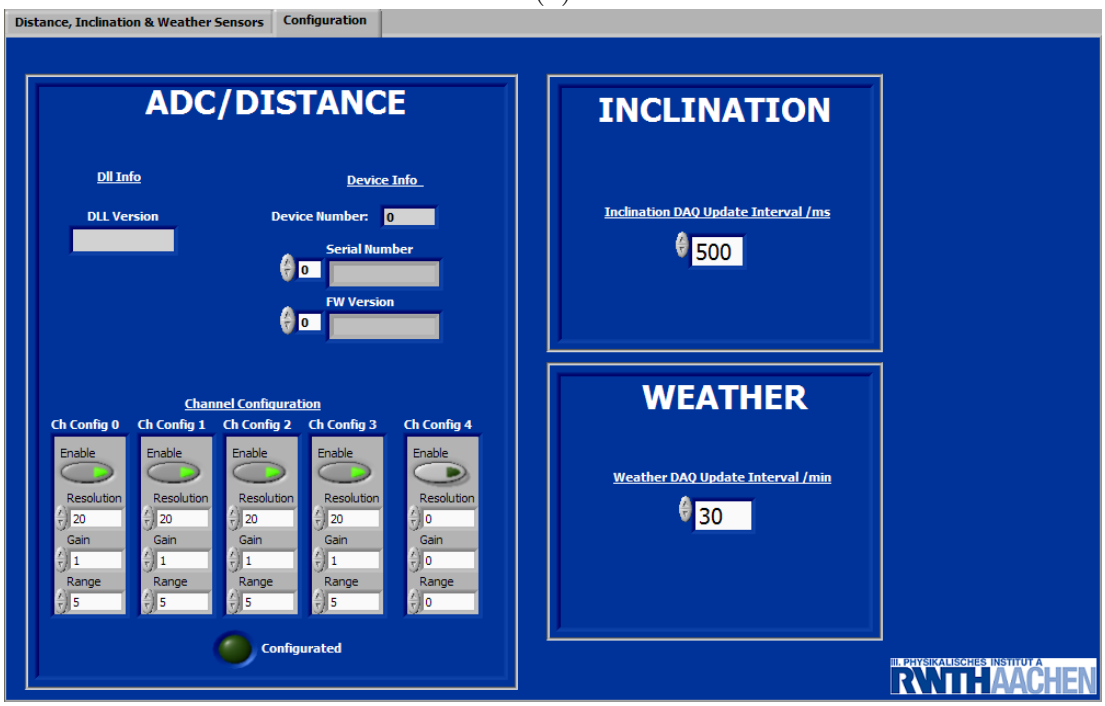

(b)

Figure 29: Screenshot of the Front Panel of the TiltMonitor.exe executable with (a) the first tab showing the sensor monitoring interface (no measurements), (b) the second tab showing the sensor configuration interface.

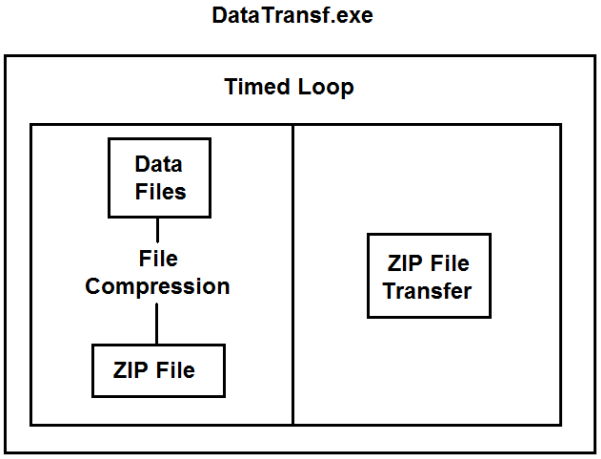

Figure 30: Organizatorial chart and block diagram of the DataTransf.exe executable file.

4.4 Result

It is required for the whole system to have no impact on the normal functioning of the telescopes. Hence the need for the setup to keep a compact and presentable appearance. Every piece of hardware, aside from the sensors and the weather station, was carefully placed inside a metal container labeled as "TiltMonitor". A metal plate then separates the container in two levels, a higher one for the laptop and a lower one for every other piece of data acquisition hardware. A multiple socket strip, attached to the back end of the metal container provides power sockets for the various required AC/DC adapters. Small openings in the box allow ethernet, sensor and power supply cables to connect to devices in the box. Under normal measuring circumstances, the metal box is to remain closed. For maintenance or debugging tasks, it is however possible to monitor the measurements in real time with the help of the front panel of the TiltMonitor.exe application. A schematic representation of the setup complete with hardware, container and cable connections can be seen in Fig. 31.

The resulting setup offers a complete and functional system. It provides a stable environment for a long duration measuring process and allows a thorough monitoring of the mechanical deformation of the HEAT telescopes.

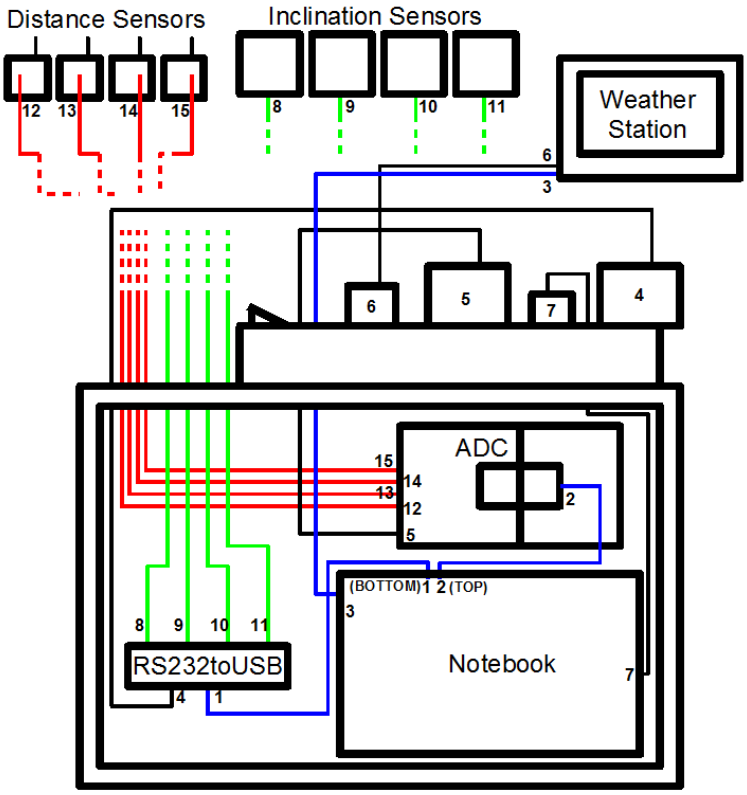

Figure 31: Schematic representation of the finished setup for the hardware that composes the Tilt Monitor. (1)USB Cable for RS232-to-USB Converter (BOTTOM USB); (2)USB Cable for microBOX ADC (TOP USB); (3)USB Cable for Weather Station; (4)9V AC/DC Adapter for Inclination Sensors; (5)4.5V AC/DC Adapter for Distance Sensors; (6)5V AC/DC Adapter for Weather Station; (7)19V AC/DC Adapter for Notebook; (8-11)6 Pin RS232 Signal Cables for Inclination Sensors; (12-15)3 Pin analog Signal Cables for Distance Sensors.

5 Calibration of the Sensors

Before using the sensors for their monitoring task, both inclinometers and potentiometers had to be calibrated. In the case of the inclinometers, the factory settings provided, from the start, a reasonable accuracy. However, a resetting of the zero point as well as a further linearisation were required to meet the standards set by this project. In the case of the distance sensors, their output signal does not directly provide a distance, but only a voltage. The distance corresponding to the measured voltage can only be calculated with the information collected from a dedicated calibrating process. Additionally, the non-linearity of the distance sensors was also corrected.

5.1 Inclination Sensors

An inclination table, or goniometer, was the tool used to adjust the real inclination of the sensors during the measurements. The surface of the inclination table was large enough to fix a sensor on it. Alternatively, it provided a stable surface on which a metal plate large enough to mount all four inclinometers could be fixed. This goniometer was itself installed on an aluminum platform, made in the mechanical workshop of the III. Physikalisches Institut of the RWTH. Using an adjusting screw, the surface of the goniometer could then be tilted from -10^o to 10^o with a precision well above the resolution of the inclinometers. The range of the goniometer was not large enough for a complete calibration of the sensors in the required range (from -20^o to 20^o). Therefore, an additional platform with a 10^o slanted top was made to extend the measuring range of the goniometer. The platforms, along with the goniometer and sensors, could then be screwed to a heavy horizontal working table on which the calibration process was conducted. Images of the setup used for this calibration are shown in Fig. 32 (a) and (b).

The zero degree inclination for both X and Y axes of the inclinometers was established according to the reasonable assumption that the measuring table offered an exactly horizontal area. The observation of the behaviour of the sensors only supported this concept. The inclination of the work bench was measured with the sensors placed directly onto the table. An offset was observed, but it remained constant when the sensors were rotated 90 degrees horizontally. The observed offset was then corrected to zero with a built-in function of the sensor implemented with LabVIEW.

5.1.1 Linearity

After this initial setting was corrected, the actual calibration process was applied. An integral calibration was only possible after the consideration of all possible sources of uncertainties. For this reason, three different measurement processes were performed. Each one of the processes contributed a separate error.

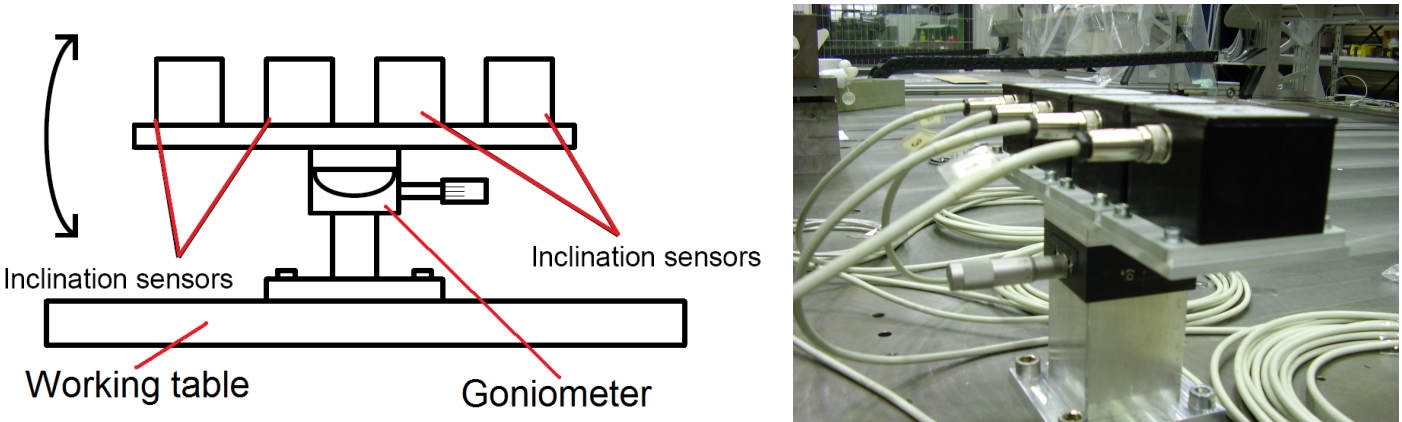

(a) (b)

Figure 32: (a) Schematic representation of the accurate inclination table, or goniometer, used to calibrate the inclination sensors. (b) Picture of the actual calibration setup used for the inclination sensors.

The calibration started with the already mentioned linearity measurement. The non-linearity is defined as the deviation of the characteristic curve of the sensor from a linear response. In order to calculate this parameter and correct the data accordingly, the sensors were manually tilted with the goniometer and the inclination was measured every 0.08^o. The entire measurement offered a total of 500 equidistant data positions between -20^o to 20^o for the linearity analysis. This was carried out by measuring firstly the range between -10^o to 10^o with the normal platform. The remaining range was then covered using the platform with the inclined top.

It turned out that, due to the mechanical properties of the goniometer, the measurements led to different results depending on the direction in which the goniometer was rotated (these differences are caused by the goniometer and do not reflect an hystheresis of the sensors). The goniometer is basically composed of two superimposed platforms. The lower platform remains always in the same position, while the second can be tilted using the adjusting screw. In one direction, the screw pushes the second platform, thereby tilting it. In the other direction, the screw is pulled outwards and the second platform is pulled back to the original position by springs located inside the goniometer. Due to the weight of the sensors, once reached a certain inclination, the springs were not strong enough to completely pull the second platform back. This caused a gradual loss of precision in the goniometer that led to inaccurate results, when moved in this direction. The data was therefore taken by moving the goniometer always in the first direction.

Once the linearity measurement was finished, the data for all four inclinometers could then be displayed against the real inclination extracted from the goniometer (see Fig. 33 (a)). Lastly, linear fits were applied to the four different curves. The values corresponding to both slopes and offsets that resulted from the linear fits are given in table 3.

The differences between the measured data and the linear response range from -0.2^o to 0.15^o. However, compared to the range of the devices, these values remain relatively small. This makes it difficult to observe a clear appreciation of the non-linearity under the layout shown in Fig. 33 (a). In order to better evaluate the linearity, the measured data was subtracted to the linear fit. The obtained residuals from the fit, shown in Fig. 33 (b), provide a clear representation of the non-linearity of the measured data and demonstrate the necessity of a recalibration. For all 4 sensors, there is a similar well-defined, characteristic curve, not caused by statistical fluctuations, but by systematic inaccuracies. These are the result of the properties of the sensors themselves and are also several times larger than the limit of $\pm 0.01^o$ required for this task.

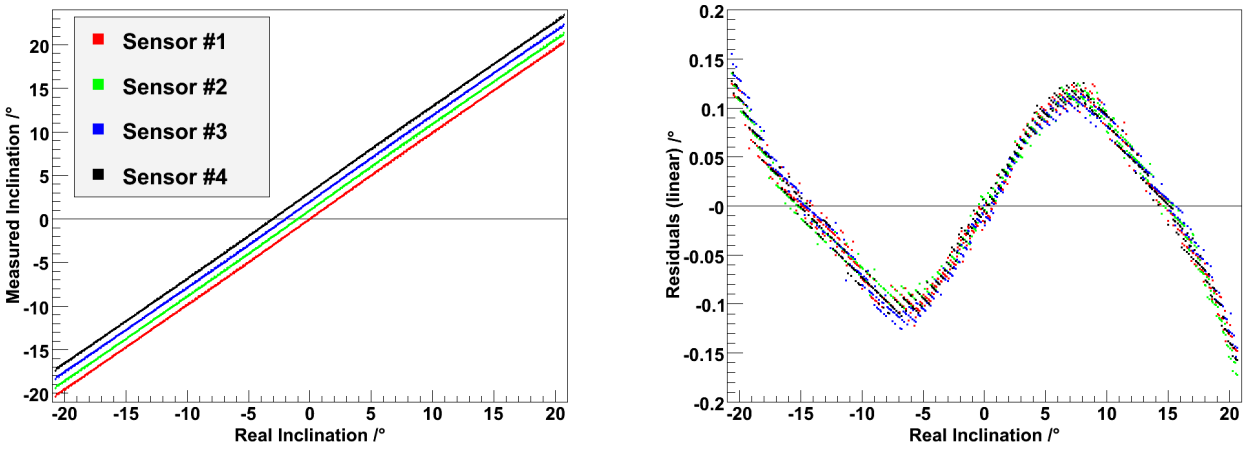

(a) (b)

Figure 33: (a)Linearity calibration for the four inclination sensors. (b)Residuals of linear fit.

Two different methods were applied to recalibrate the sensors. The first method requires the use of a polynomial fit instead of a linear fit as the reference for later measurements. The difference between a polynomial and a linear fit only depends

Sensor Nr.	Slope	Offset [^{o}]
1	0.9832 ± 0.0003	0.0267 ± 0.0033
2	0.9841 ± 0.0003	0.0135 ± 0.0033
3	0.9829 ± 0.0003	0.0096 ± 0.0033
4	0.9842 ± 0.0003	0.0451 ± 0.0033

Table 3: Parameters extracted from the linear fits of the linearity plots in Fig. 33.

on the higher degree of the polynomial function that is adjusted to the data. In this case, a polynomial fit of seventh degree provided by the fitting package of ROOT [27] was used. The higher degree allows a better alignment of the curve with the measured data, as shown in Fig. 34 (a). However, for functions with degrees higher than seven, the improvement over the previous order was negligible.

After applying this fit, the residuals were considerably reduced along the entire range. Nevertheless, other problems remained. For example, instead of the desired statistical distribution, the residuals show an evident structure. Moreover, despite the significant decrease in the residuals, they maintain values over the 0.01^o limit, and even reach 0.02^o in some cases. In conclusion, this first method leads to improved, but not entirely satisfactory results.

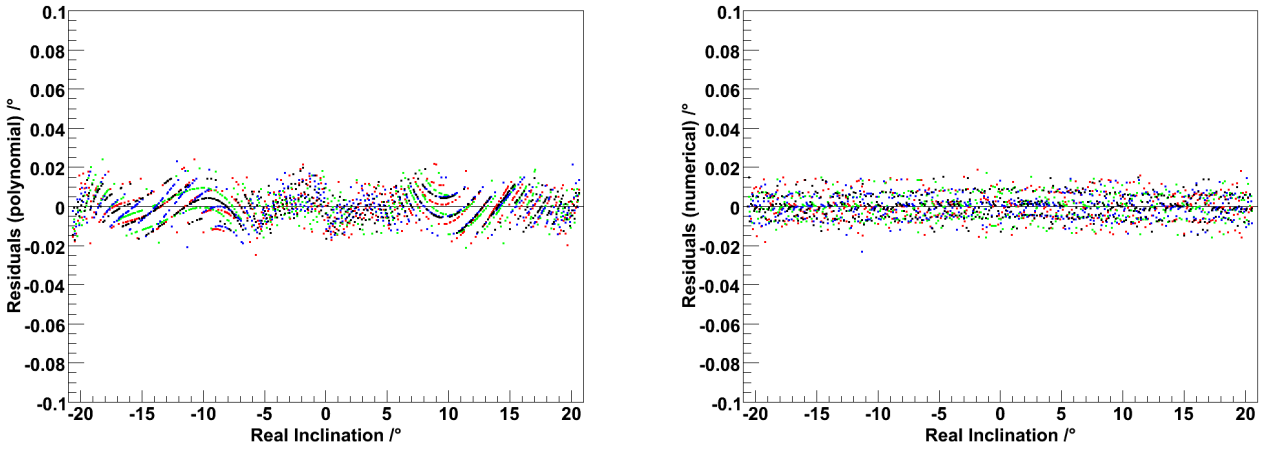

(a) (b)

Figure 34: (a)Residuals of polynomial fit. (b)Residuals of numerical fit.

The second method was called "numerical fit", though strictly speaking it does not really function as a fit. This particular method basically creates an alternative data set using a numerical algorithm. It starts by calculating the average value between

the first and third point in the data set, which is subsequently defined as the new, corrected, second point. The same process is then repeated with the corrected second point and the fourth point from the original data set to determine the corrected third point. The algorithm goes on until eventually the end of the original data set is reached. For a better understanding of the concept, a schematic sketch of the process is given in Fig. 35. The result of this process is a smoothed data set that can be later used as a reference. Note that, in order to calculate the final data set, the algorithm is only executed once, i.e. there are no additional iterations of the process.

The result of the process is an improved "fit" of the measured data with a correcting effect on the data points. Strong systematical fluctuations caused by the measuring process or the sensors themselves are thus removed. This can be verified with the residuals shown in Fig. 34 (b). Moreover, not only is there no recognizable structure anymore, but the residuals appear to have been noticeably reduced (with values typically around 0.006^o) compared to the previous results with the polynomial fit.

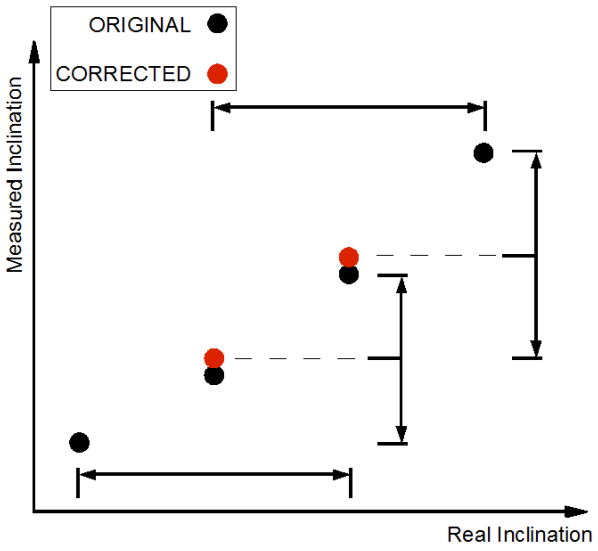

Figure 35: Principle of the "numerical fit" method.

For a thorough evaluation of the two fitting processes, the residuals were fed into two separate histograms (see Fig. 36 (a) and (b)). A "Gauss fit" was then applied to the data from each one of the sensors. The Gauss fit function provided by ROOT extracts the mean value $\overline{x}$ as well as the standard deviation σ of the four residuals. The resulting values are displayed in table 4.

Note that the mean values $\overline{x}$ of the Gauss fits are all located between 0 to 0.0002^o. Furthermore, the errors associated with these values are all smaller than 0.0003^o, which makes all the mean values compatible with zero. This result derives from the

fact that the $\overline{x}$ of both histograms are by definition 0, i.e. it is a property of the fits.

The apparent improvement of the numerical over the polynomial method observed in the previous Fig. 36 is confirmed by the values of the standard deviations written in table 5. This table shows a consistent reduction of the σ by more than 0.001^o for all four sensors.

The application of a Gauss fit is not entirely appropriate in these cases, as neither of the two methods results in truly gaussian distributions. Unlike the polynomial fit, the numerical fit leaves no visible structures attributable to systematical uncertainties. Nevertheless, another distorting effect can be observed in the residuals of the numerical fit. This effect consists in the existence of different levels along the horizontal axis in which the density of the residuals appears to be consistently higher. It can only be observed with an extremely thin binning, as displayed in Fig. 37 (bin length Δ x = 0.001^o). The use of such a thin binning is however unrealistic, considering that the resolution of the sensor is already ten times higher than the bin length (1 bit $\equiv 0.01^o$). On the other hand, with the more appropriate binning shown in Fig. 36 this effect almost disappears.

Although some minor problems still remain, the use of the numerical fit appears to provide the best results. It is therefore the best option for the linearity recalibration. Given the goal of the setup of 0.1^o, the target accuracy of 0.01^o is reached in all cases.

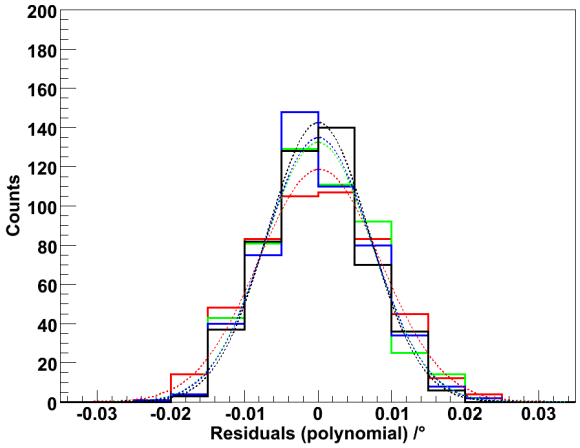

Histogram of residuals (polynomial)

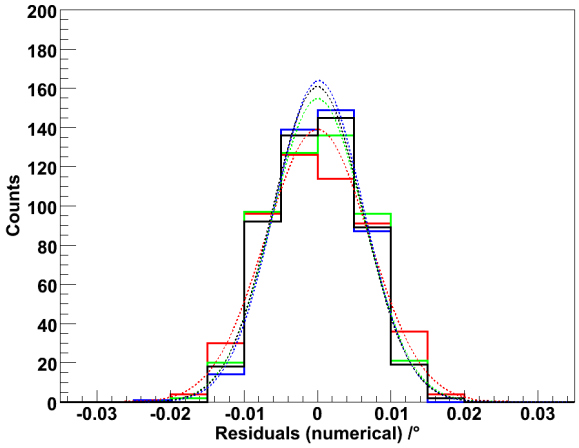

Histogram of residuals (numerical)

Figure 36:

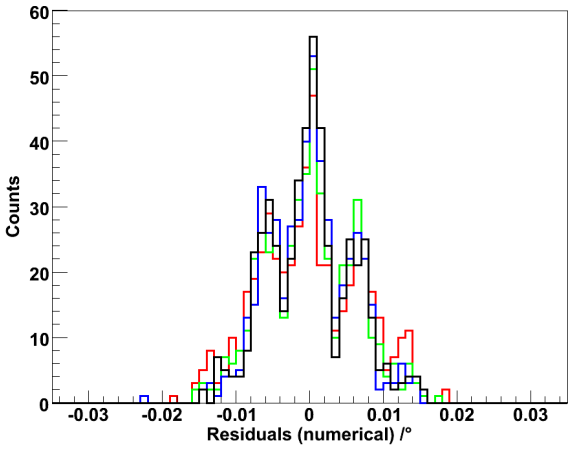

Figure 37: Histogram of residuals resulting from the numerical fit, with bin size Δx =0.001^o.

Sensor Nr.	Mean $\overline{x}$ [^{o}]	Standard Deviation σ [^{o}]
1	0.0002 ± 0.0004	0.0083 ± 0.0002
2	0.0000 ± 0.0003	0.0073 ± 0.0002
3	0.0001 ± 0.0003	0.0073 ± 0.0002
4	0.0000 ± 0.0003	0.0069 ± 0.0002

Table 4: Parameters that result from the application of Gauss fits to the residuals of the polynomial fit.

Sensor Nr.	Mean $\overline{x}$ [^{o}]	Standard Deviation σ [^{o}]
1	0.0000 ± 0.0003	0.0070 ± 0.0002
2	0.0001 ± 0.0003	0.0063 ± 0.0002
3	0.0002 ± 0.0003	0.0061 ± 0.0002
4	0.0000 ± 0.0003	0.0062 ± 0.0002

Table 5: Parameters that result from the application of Gauss fits to the residuals of the numerical fit.

5.1.2 Repeatability

However accurate, the linearity calibration alone is not enough to guarantee a correct description of the sensor properties. Two consecutive measurements along the entire range of the sensor result in similar, albeit different values. This fluctuation is described by the parameter called repeatability. The repeatability is defined as the deviation of a random measurement from the reference data. This factor is the result of the material properties of the sensor and cannot be corrected.

To measure the uncertainty that results from this parameter, the following process was carried out: After the previous measurement for the linearity, an additional measurement along the whole range was performed. It followed exactly the same procedure (order of measurements and rotation direction). The data measured this second time was subtracted from the data given by the numerical fits applied to the first measurement. The result of this operation, a sort of residual of the repeatability, can be seen in Fig. 38 (a). The corresponding histogram and Gauss fits are plotted in Fig. 38 (b).

Note that, in this case, the mean values of the fits are not situated exactly at the zero value. This is due to the nature of the repeatability, which unlike the linearity, does not automatically define the zero point as the mean value $\overline{x}$. Additionally , the fluctuations are different and clearly not statistically distributed. The table 6 shows the parameters extracted from the four Gauss fits. The values of the last column define the repeatability of the inclinometers. The values are determined by the standard deviation σ and the mean $\overline{x}$, as the two provide important and complementary information. Therefore:

$$u_{Rep} = \sqrt{\sigma_{Rep}^2 + \overline{x}_{Rep}^2} \tag{10}$$

This is another difference between the repeatability and the linearity. The latter being only defined by the standard deviation of the Gauss fits.

Sensor Nr.	Mean $\overline{x}$ [^{o}]	Standard Deviation σ [^{o}]	Repeatability Error [^{o}]
1	0.0023 ± 0.0006	0.0125 ± 0.0004	0.0127
2	0.0009 ± 0.0005	0.0117 ± 0.0004	0.0117
3	0.0026 ± 0.0004	0.0088 ± 0.0003	0.0092
4	-0.0049 ± 0.0004	0.0090 ± 0.0003	0.0102

Table 6: Parameters that result from the application of Gauss fits to the repeatability data.

5.1.3 Temperature Dependence

The ambient temperature in which sensors operate tends to become the environmental factor with the biggest influence on the precision of their measurements. For

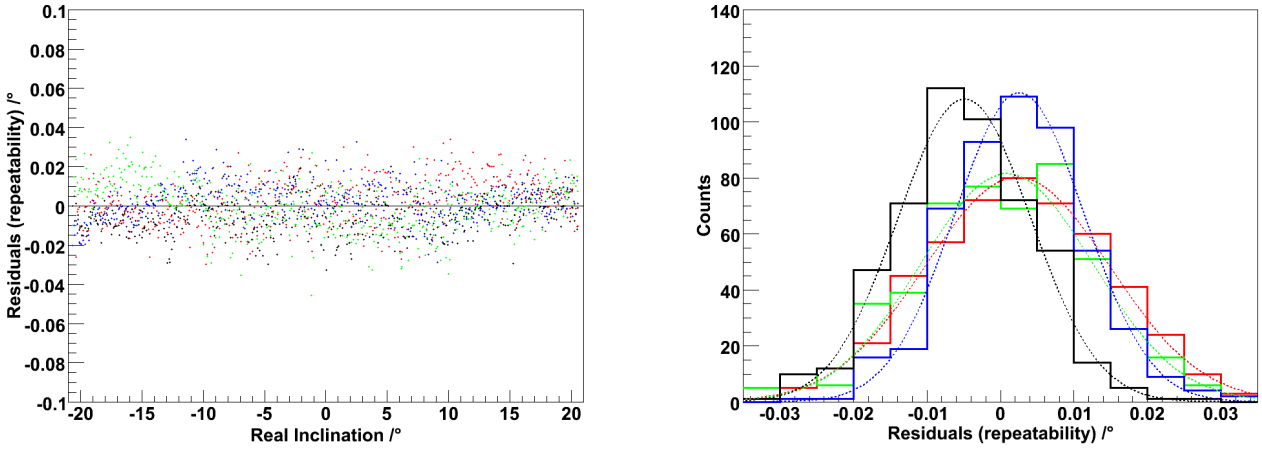

(a) (b)

Figure 38: (a)Repeatability measurement. (b)Histogram of repeatability.

this reason, the last part of the calibration deals with the temperature dependence of the sensors.

Unfortunately, for a determination of this parameter a great number of constraints associated with this process have to be taken into account. First of all, the temperature has to remain homogeneous for it to be determined with great precision for all four sensors. Additionally, there has to be absolutely no material, other than the inclinometers themselves, biasing the measurements. This would be the case, for example, if the measurement was performed with the sensors placed on a steel table. An inhomogeneous temperature variation would deform the table itself, due to the considerable thermal expansion coefficient of steel (α_{steel} = 13 μm /(K $\cdot$ m)). This would alter the inclination and bias the results.

The setup should therefore avoid these problems and solely measure the variation caused by the effect of the temperature on the sensor. On the one hand, a long-duration measurement would ensure the homogeneity of the ambient temperature. However, it would still not provide enough information to describe the temperature dependence, since the fluctuations in the laboratory do not surpass 3 or 4 degrees. On the other hand, if the air surrounding the sensors is to be heated, the homogeneity in the temperature must be maintained.

To avoid all these problems, the following setup was used (see Fig. 39): The sensors were fixed on a styrofoam pad and placed inside a styrofoam box with dimensions of roughly 1m $\times$ 0.5m $\times$ 0.5m. The box was placed on the stone floor of the labo-

ratory. Styrofoam is a thermal insulating material, able to contain the heat inside the box. A hole on the top of the styrofoam box allowed the introduction of an electrical heater to increase the air temperature inside the box. Using this method, the temperature could be raised from 20°C up to 60°C in roughly 10 minutes. Another styrofoam plate finally covered the sensors as well as the wireless thermometer placed inside the box. Without this last plate, a direct heating of the sensors could have damaged them. The inclination was then measured for angles of approximately 15° and -15° during more than one hour. The homogeneous heating of the content of the styrofoam box ensured that there were no temperature differences, as every component, including the styrofoam, was heated uniformly. Note also that numerous tests were performed with slightly different setups, always with similar results (for instance, measurements were performed with the inclinometers fixed on a steel plate instead of a styrofoam pad).

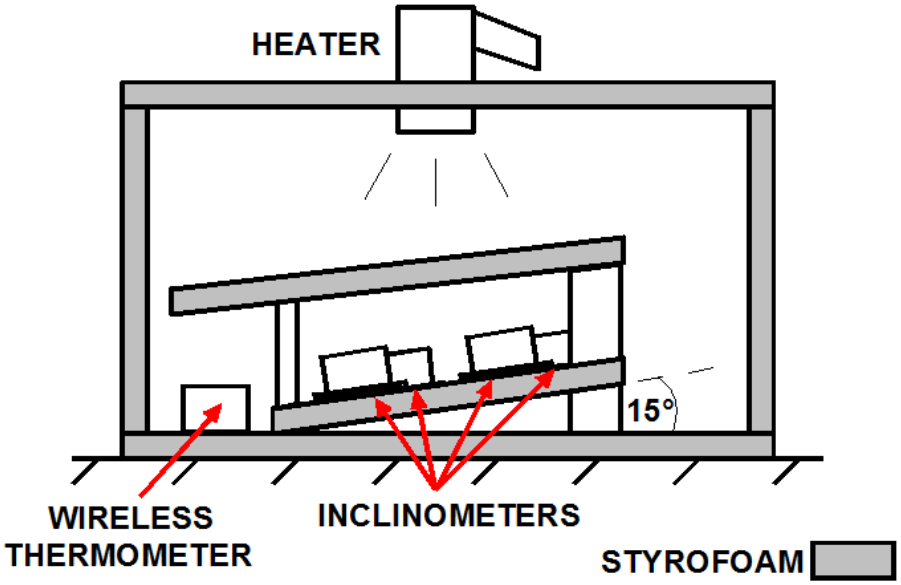

Figure 39: Schematic view of the setup used for the temperature dependence measurement.

The measurement took place during the cooling process that followed the heating process once the heater was turned off. This slower process ensured the complete temperature homogeneity inside the styrofoam box as well as a significantly better description of the temperature curve. Otherwise, since the thermometer only delivers one value per five minutes, it would not have performed sufficient measurements. This would have resulted in an inaccurate temperature reconstruction.

Once the temperature stabilized with the outside temperature the measurement was stopped. An example of such a measurement versus time is shown in Fig. 40. The four increasing curves represent the inclination measurements, while the blue

descending curve corresponds to the temperature. Even though the inclination of the setup remains unchanged, the decrease of the temperature leads to a clear increase of the measured inclination. This confirms that there is indeed a temperature dependence.

The low acquisition rate of the wireless thermometers limited the amount of temperature information. A hyperbolical fit was therefore applied to the temperature measurements in order to describe its behaviour. The inclination could then be plotted against the temperature, and a linear fit could finally be applied to the data. The slope that results from these linear fits characterizes the temperature dependence of each sensor. Fig. 41 displays these plots for inclinations of 15^o and -15^o. These are supposed to be the inclinations under which the sensors will later operate. The use of two independent measurements also offers the possibility to contrast the results with one another.

Note that the non-linearity observed for temperatures above 35°C comes from two different effects. The rapidly decreasing temperature at the start of the measurements combined with the slow acquisition rate of the thermometer lead to an inaccurate temperature representation. This, added to a persistent inhomogeneous temperature distribution caused by the previous heating process, render the first 5 to 10 minutes of the measurement unemployable. The data for temperatures higher than 32°C was therefore left unused.

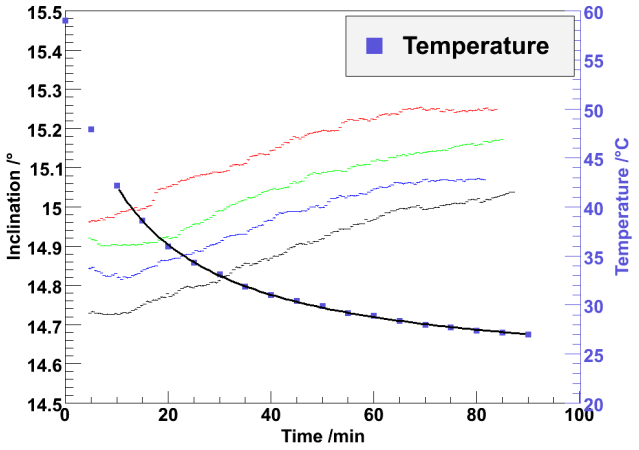

Figure 40: Example of a temperature dependence measurement comprising data from the four sensors as well as the temperature information. The thicker black curve corresponds to the hyperbolic fit applied to the temperature data.

The values shown in table 7 demonstrate a fairly similar performance for all inclinometers under temperature variations. Given the systematic uncertainties of

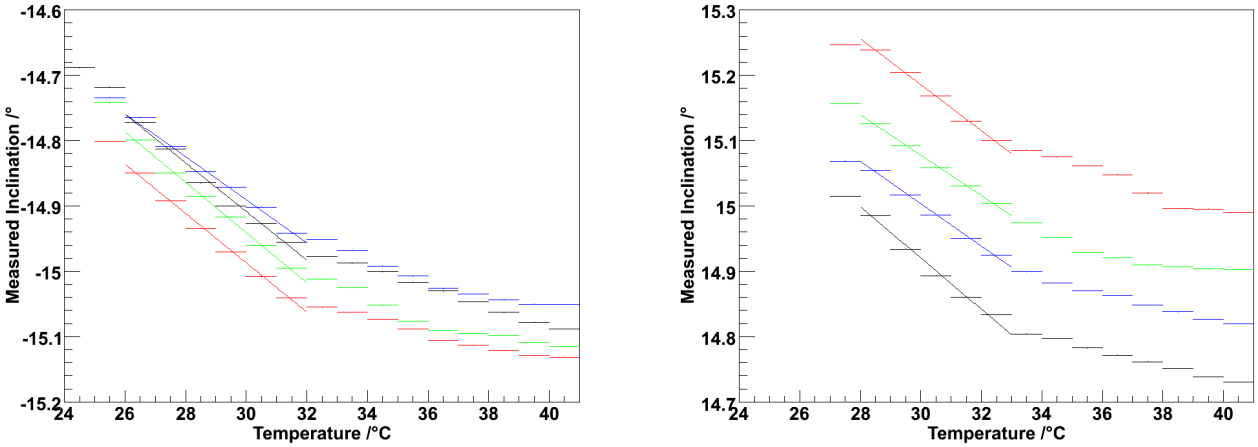

(a) (b)

Figure 41: (a)Inclination versus temperature, $\alpha = 15^o$. (b)Inclination versus temperature, $\alpha = -15^o$.

Sensor Nr.	Slope [^{o}/K] for 15^o	for -15^o
1	-0.0352 ± 0.0001	-0.0378 ± 0.0001
2	-0.0309 ± 0.0001	-0.0385 ± 0.0001
3	-0.0324 ± 0.0001	-0.0329 ± 0.0001
4	-0.0392 ± 0.0001	-0.0372 ± 0.0001

Table 7: Parameters describing the temperature dependence of the inclination sensors, extracted from the linear fits of the plots in Fig. 41.

the improvised setup, and for the sake of uniformity, the intermediate value of $0.035 \pm 0.005\ ^o/K$ was defined as the temperature dependence for all sensors. This value is compatible with all experimental results. For this reason, it provides an approximation of the effect of temperature variations, while considering possible discrepancies from the exact value with a large enough σ. Knowing that the method used for this experiment does not offer the same unequivocal precision as the previous calibration, the result could very well suffer from limited but significant bias. As such, the literal application of the individual parameters shown in table 7 could have been problematic. Note that the small errors in table 7 correspond to the error of the linear fit. With a large amount of data taken into account for each fit, the scale of the errors is understandable. They do not, however, provide the uncertainty on the parameter itself.

The plots in Fig. 41 reflect a constant effect of the temperature on the sensors. In this measurement, the slopes are the only relevant factor. The offsets do not contribute any substantial information to the calibration, since the sensors were not placed in the exact same position. Note that the temperatures used for the linear fits range from 25^oC to 33^oC and lie slightly higher than the expected operating temperature of the HEAT telescopes (20-25^o).

The linearity and the repeatability processes combine into what is considered the baseline calibration. Afterwards, the effect caused by the temperature dependence can be extrapolated using the temperature measurements of the weather station. This effect can then be added to the the baseline calibration, which was carried out at the constant temperature of 23.0^o.

5.1.4 Y-Axis

The previous calibration involves only the X-axis of the inclinometers. For their complete calibration, a process similar to the one just described was carried out for the Y-axis. The linearity was however only measured up to 10^o, as no inclinations in the Y-axis are expected from tilting the enclosures. For the repeatability, no additional evaluation was done, as the parameters extracted from the X-axis measurements could also be applied here. However, for the temperature dependence of the Y-axis of the inclinometers, a variation of the previously measured data was seen. In fact, an analysis of the Y-inclination measured during the previous temperature dependence test, for which the Y-inclination was always roughly 0, resulted in the following table:

Unlike the results for the X-axis, table 8 shows different temperature dependences for each sensor. As a result of this, a mean value can not be chosen and applied to all four sensors. Hence, the temperature correction has to be carried out for each sensor individually with the parameters displayed in table 8.

Sensor Nr.	Slope [^{o}/K] for 0^o
1	-0.0044 ± 0.0001
2	+0.0322 ± 0.0001
3	-0.0063 ± 0.0001
4	-0.0319 ± 0.0001

Table 8: Parameters describing the temperature dependence of the inclination sensors, extracted from the linear fits of the plots in Fig. 41.

5.1.5 X-Y Correlation

Besides the temperature dependence, the Y-axis measurement may depend on the X-inclination. For this reason, the determination of the deterioration of the Y-axis accuracy as a function of the X-inclination required an additional measurement. This phenomenon can be interpreted as the result of two circumstances. Firstly, the inclination of the sensor in the X-axis necessarily complicates the determination of the Y-inclination, as the tilted sensor becomes less and less sensitive. Secondly, poorly insulated electrical signals in parallel circuits influence each other by induction [24]. These effects are especially noticeable for greater X-inclinations, as shown in Fig. 42. The measurement displays the variation of the measured Y-inclination during the X-inclination linearity measurement. The deterioration of the Y-inclination accuracy as a function of the X-inclination leads therefore to an additional correction that is exclusively applied to the Y-inclination measurements. In this case, a linear fit applied to the data from each sensor largely suffices to recalibrate them. The values for $X_{inclination}$ =-15^o and $X_{inclination}$ =15^o are again the most important, since those are the standard positions of the inclinometers in the final setup in the telescope.

Note that another potential cause of this effect could come from the misalignment of the goniometer and the X-axis of the sensors. However, due to the consistency of the measured values, and their independence of the sensor position, such a cause is unlikely.

Sensor Nr.	Slope	Offset [^{o}]
1	-0.0054 ± 0.0001	-0.0226 ± 0.0016
2	-0.0064 ± 0.0002	0.01449 ± 0.0022
3	-0.0057 ± 0.0001	-0.0037 ± 0.0012
4	-0.0036 ± 0.0001	-0.0299 ± 0.0006

Table 9: Parameters describing the deterioration of the Y-inclination measurement with increasing X-inclination, extracted from the linear fits of the plots from Fig. 42.

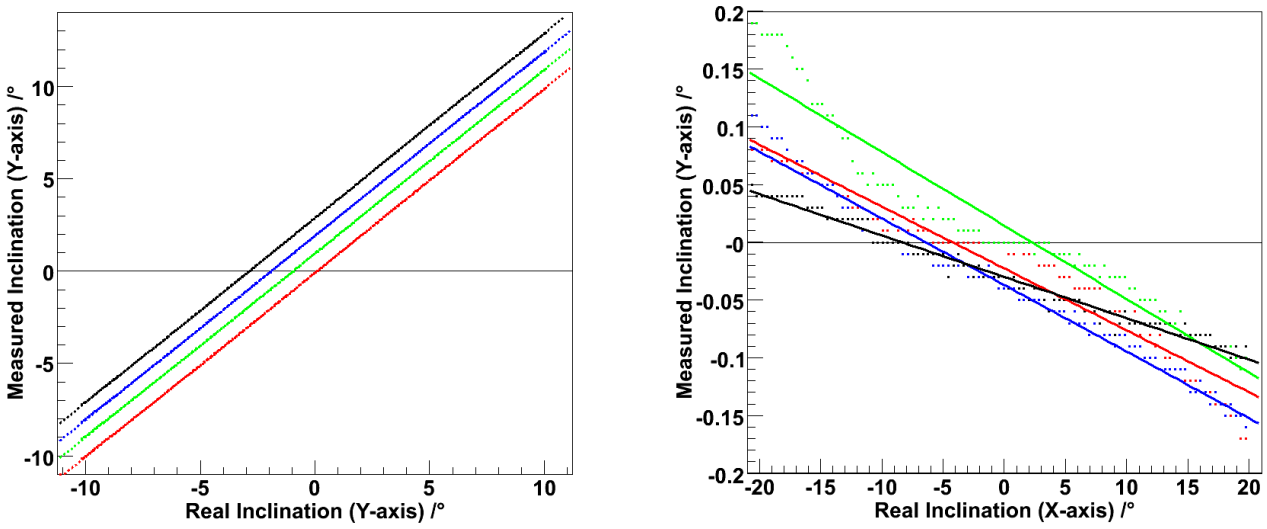

(a) (b)

Figure 42: (a)Linearity calibration for the Y-axis. (b)X-Y-axes correlation measurement.

5.1.6 Summary of Inclination Calibration

As a result of the inclination recalibration, the accuracy of the inclinometers improves significantly. The values of the uncertainties for the repeatability u_{Rep} and the the non-linearity u_{Lin} remain under 0.015^o for all sensors. This is more than six times better than the 0.1^o tolerance of the HEAT telescopes. The uncertainty that derives from the temperature correction u_T=0.005^o/K varies depending on the temperature of the environment. With appropriate temperature measurements, assuming for example variations of 5^oC, the total accuracy theoretically remains under 0.3^o, which still is more than three times better than the tolerance.

5.2 Distance Sensors

5.2.1 Linearity

The calibrations of distance sensors and inclinometers share many similarities. Once more, the same three separate aspects, linearity, repeatability and temperature dependence, are the basis of the calibration. Only the methodology behind each measurement varies slightly. Instead of fixing the sensors to an inclination table, they were attached to a micrometer. This micrometer is capable of adjusting distances with a precision of 5 μm. The sensor cables were fixed to a stable wall situated next to the micrometer. The distance between the sensors and the wall could then be altered with great precision. This allowed an analysis of the measured data as a function of the real distance.

Similarly as with the inclinometers, the distance between the sensors and the wall was then increased from 0cm up to 5.1cm (which corresponds to the maximum range of the potentiometers) in steps of 250μm. The objective of this measurement was not just a recalibration, but a complete transformation from the output voltage to the correlated distance (including digitization). For schematic representations as well as pictures of the setup see Fig. 43 and 44.

The result of this measurement can be plotted versus the real distance, and linear fits can also be applied to the data (Fig. 45 (a)). Subtracting values from the linear fit from the data leads to the residuals shown in Fig. 45 (b). As it was the case for the inclinometers, the residuals are significant and do not provide the needed accuracy. To reduce the residuals down to an acceptable level, the use of both the polynomial and numerical methods was also required, leading to similar results. In contrast to the linear and polynomial fit, the numerical fit provides again structure-free residuals with a minimal spread. Fig. 46 and 47 display the residuals and the histograms, respectively. The values of the Gauss fits are written in tables 11 and 12.

For the inclinometers, a small but noticeable improvement was observed in the transition from polynomial to numerical fit. The better quality of the numerical method becomes much more apparent here. Gauss fits result in σ roughly half as large as with the polynomial fit. In addition to that, there are other significant differences between the results for the two types of sensors. For instance, in the case of the potentiometers, the size of the bins have no impact on the form of the histograms, as shown in Fig. 47 and 48. The 20 bit resolution achieved by the ADC is likely responsible for the absence of structures in the histogram. This suggests that the distribution observed in Fig. 37 for the inclination sensors are the result of their relatively low resolution.

The performance of the distance sensors combined with the use of the microBOX ADC provides excellent results. Nevertheless, the sensors turned out to be some-

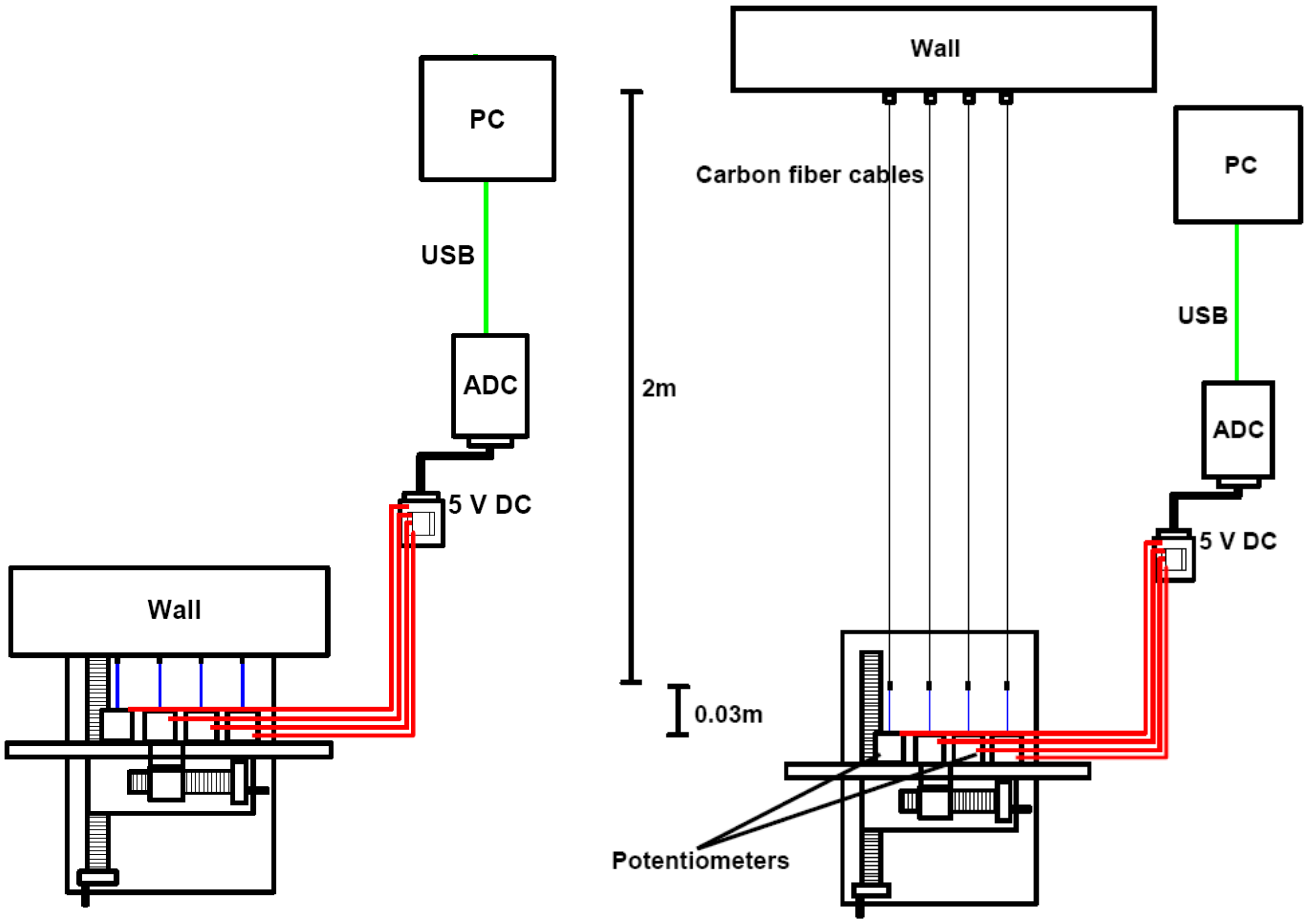

(a) (b)

Figure 43: Schematic representations of the setups used for (a) the calibration (b) the stability measurement of the distance sensors.

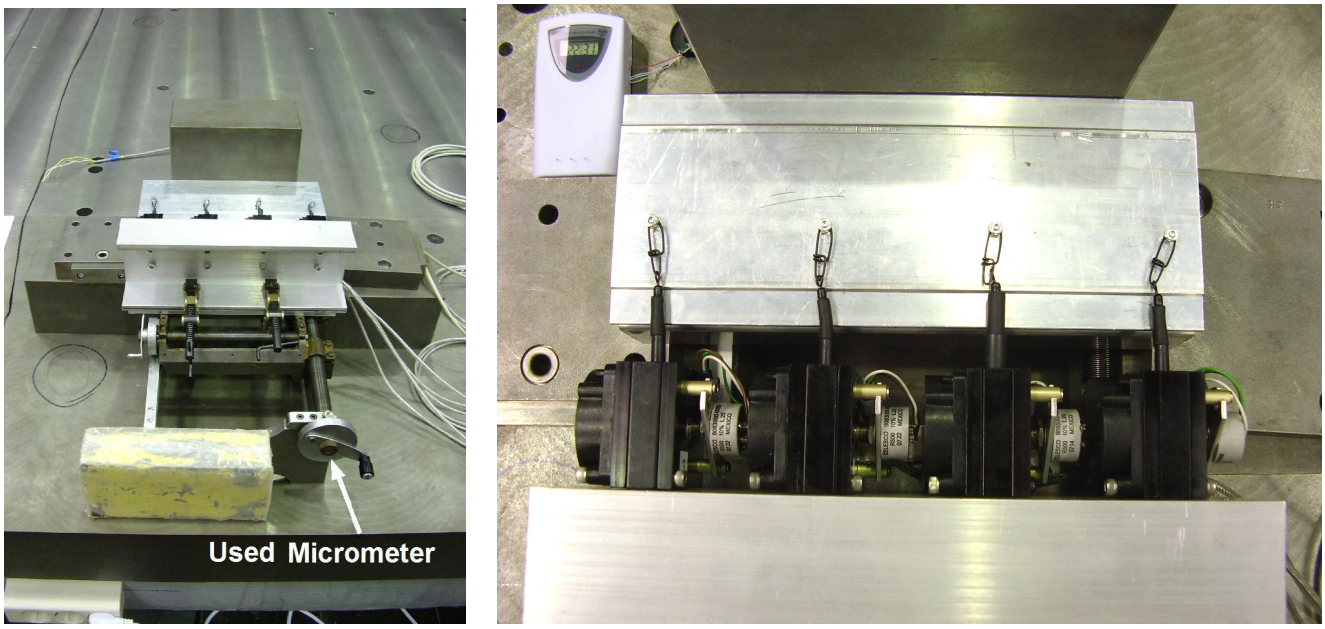

Figure 44: Pictures of the actual calibration setup used for the distance sensors. Note that the micrometer in the left right direction is not used here.

what prone to malfunction and mechanical problems. An example of this can be seen in the residuals of the distance sensor number 1, where a clear discontinuity is visible at a distance of 15mm (see Fig. 46). This discontinuity is very likely the result of a damaged section in the potentiometer. Its effect is, however, significantly reduced with the help of the numerical algorithm. Note that the accuracy is much better than required (50 μm) and that therefore the sensor is sufficiently precise.

Sensor Nr.	Slope [V/cm]	Offset [V]
0	0.8828 ± 0.0002	0.2486 ± 0.0005
1	0.8776 ± 0.0004	0.0085 ± 0.0012
2	0.8814 ± 0.0004	0.2214 ± 0.0013
3	0.8810 ± 0.0007	0.2712 ± 0.0019

Table 10: Parameters extracted from the linear fits of the linearity plots in Fig. 45.

5.2.2 Repeatability

The repeatability of the potentiometers was evaluated following the same procedure previously used for the inclinometers. After the initial linearity measurement, a

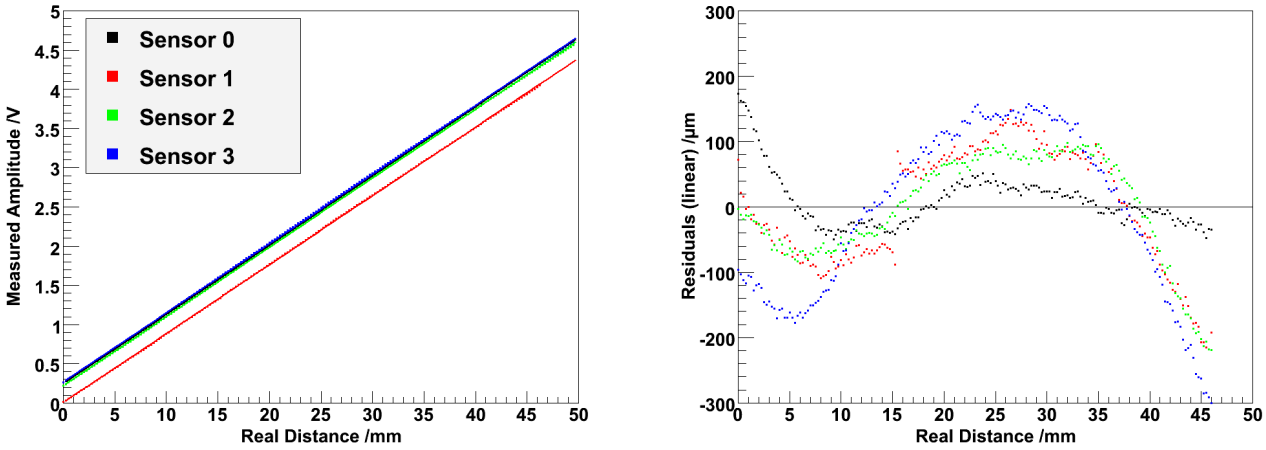

(a) (b)

Figure 45: (a)Linearity calibration for the four distance sensors. (b)Residuals of linear fit.

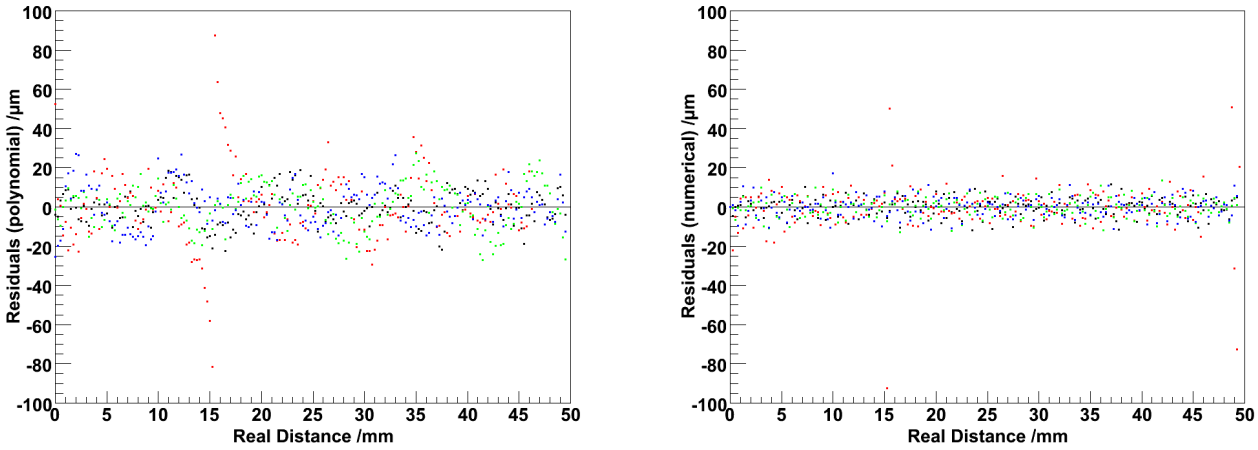

(a) (b)

Figure 46: (a)Residuals of polynomial fit. (b)Residuals of numerical fit.

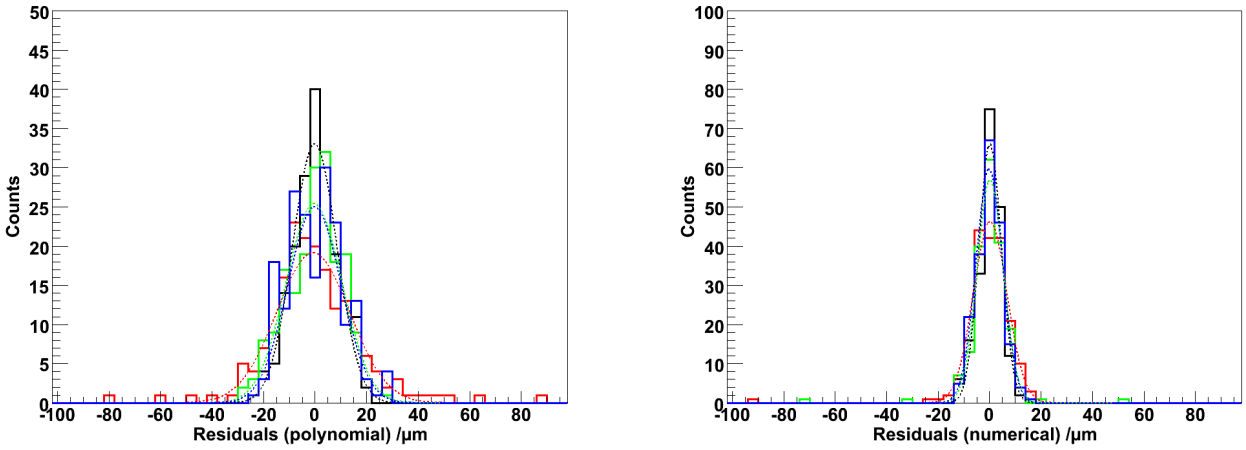

Figure 47: (a)Histogram of residuals (polynomial). (b)Histogram of residuals (numerical)

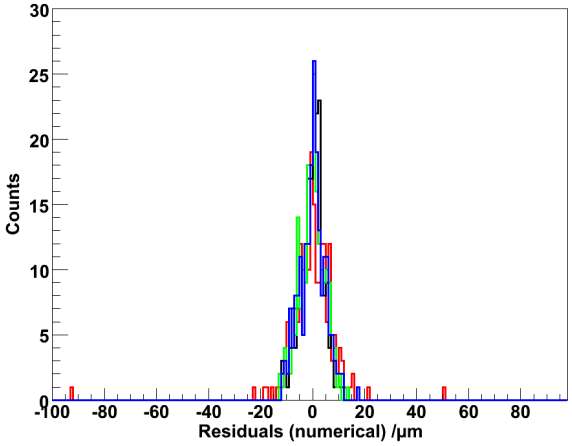

Figure 48: Histogram of residuals resulting from the numerical fit with bin size $\Delta x = 1\mu$m.

Sensor Nr.	Mean $\overline{x}$ [μm]	Standard Deviation σ [μm]
0	-0.2 ± 0.7	8.7 ± 0.6
1	-0.8 ± 1.1	14.2 ± 1.0
2	-0.4 ± 1.0	10.9 ± 0.7
3	-0.3 ± 0.8	10.4 ± 0.6

Table 11: Parameters that result from the application of Gauss fits to the residuals of the polynomial fit.

Sensor Nr.	Mean $\overline{x}$ [μm]	Standard Deviation σ [μm]
0	0.3 ± 0.4	4.4 ± 0.3
1	0.2 ± 0.5	6.4 ± 0.4
2	0.2 ± 0.4	4.8 ± 0.3
3	-0.1 ± 0.4	5.1 ± 0.4

Table 12: Parameters that result from the application of Gauss fits to the residuals of the numerical fit.

second identical measurement was carried out. The result of the second process was subtracted from the result of the numerical fit (Fig. 49) of the first measurement. The repeatability was finally determined with the help of Gauss fits (diagram in Fig. 49, results in table 13). Once again, the mean values of the Gauss fits are not located exactly on the center of the histograms. The repeatability is once more determined by the standard deviations and the mean values according to equation 10.

Sensor Nr.	Mean $\overline{x}$ [μm]	Standard Deviation σ [μm]	Repeatability Error [μm]
0	2.0 ± 0.9	10.0 ± 0.8	10.2
1	-0.1 ± 0.9	10.7 ± 1.0	10.7
2	1.0 ± 0.5	6.0 ± 0.4	6.1
3	-2.2 ± 0.4	5.1 ± 0.3	5.6

Table 13: Parameters that result from the application of Gauss fits to the repeatability data.

5.2.3 Temperature Dependence

The determination of the temperature dependence for the distance sensors is even more difficult than for the inclinometers. First of all, the same method cannot not be applied in this case. This is due to the much larger volume needed to perform the same analysis, but also because a similar heating is likely to damage the potentiometers. For that reason, the first step was to observe if temperature variations had

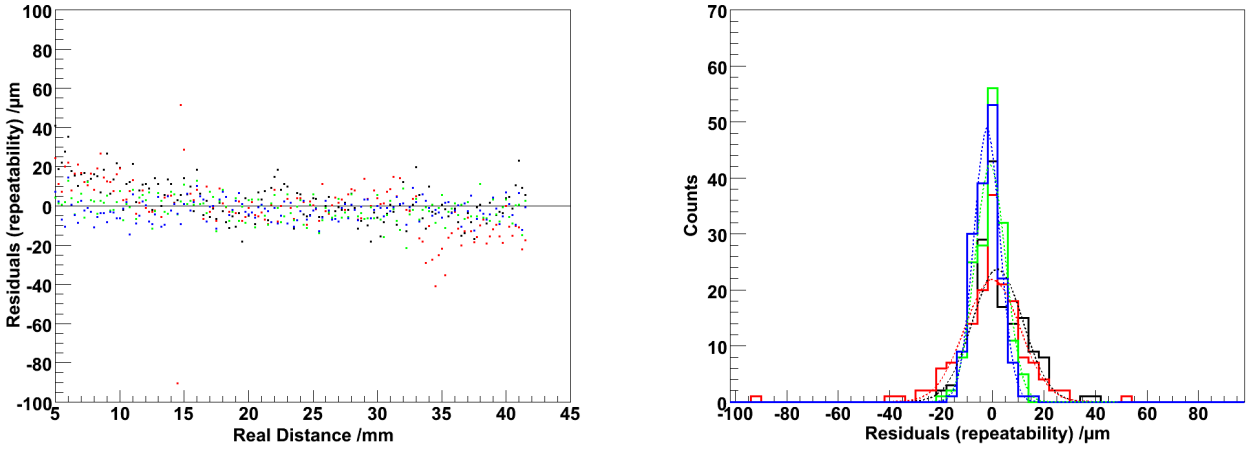

(a) (b)

Figure 49: (a)Repeatability measurement. (b)Histogram of repeatability.

any effect at all in the measurements. If no fluctuations were observed, no further analysis would then be required.

In order to evaluate the effect of temperature, two independent long duration measurements were executed. The first one used the same setup applied for both linearity and repeatability measurements. In this instance, instead of varying the distance, a constant distance was kept during the entire measurement, that lasted 20 hours. Afterwards, a second setup was used in the following test measurement, this time lasting 60 hours. Its exact configuration can be seen in Fig. 43 (b). The sensor cables were this time attached to 4 long carbon fiber cables, themselves fixed to the wall. The objective was to simulate the results expected in the telescope and compare them with the data from the first stage. Major differences were expected, mainly as a consequence of the thermal expansion of the steel stable that holds the setup.

For example, steel, from which the measurement table is primarily composed, has a relatively large $\alpha_{therm} \approx 12 \mu$m/K·m. On the other hand, the coefficient of thermal expansion $\alpha_{cf} \approx$-0.5μm/K·m of carbon fiber is almost negligible. As a result of this, temperature variations should lead to a more significant effect in the second measurement.

Fig. 50 shows the data resulting from both measurements and demonstrates the difference caused by the larger distance. In the first measurement, the temperature fluctuations caused practically no distance variations. This leads to the conclusion

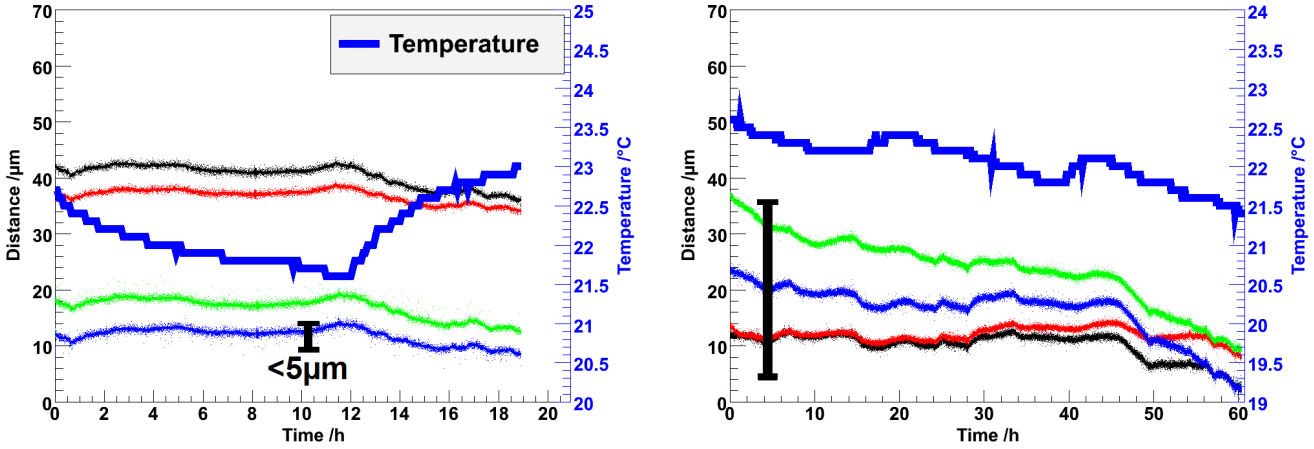

(a) (b)

Figure 50: Long duration measurements for the four potentiometers (a) with no carbon fiber cables attached to them and (b) with attached carbon fiber cables. The resulting temperature dependence is probably in part the consequence of the thermal expansion of the steel table on which the sensors are installed (the black vertical bar represents the theoretical variation of the table length).

that temperature has next to no direct effect on the sensors themselves. The effect of the temperature without the attached carbon fiber cables is, as such, negligible ($<5\mu$m for 1.5^{o}C temperature variations). On the contrary, the second measurement shows a clearly correlated trend between temperature and distance. With the extension of the cables, the sensors are therefore able to measure temperature-caused variations. These were, however, expected as the result of the deformation of the materials surrounding the sensors.

In the following, considering the results shown in Fig. 50 (a), the effect of the temperature on the potentiometers was assumed to be negligible. With the extension of the cables the distance measurements should remain accurate, since the temperature should have next to no effect on the length of the carbon fiber cables.

5.2.4 Vibration Test

Finally, an analysis of the data that results from the measurements with higher time resolution was also performed. The time resolution under this mode should theoretically allow the sensor to measure vibrations of up to roughly 100Hz. There was no real calibrating process at this point, but only a test of the functionality of this mode. This test was done by manually causing a vibration on a sensor fixed to the calibration setup. For this measurement, the sensor was read out with a frequency of roughly 1000Hz (note that for the long term measurements, another mode was used, which averages every 1000 values to one data point). The FFT function in ROOT then calculated the vibration spectrum. One of the various measurements performed during this test is pictured in Fig. 51.

In this example, the spectrum shown on the right side of Fig. 51 appears to reliably reflect the plot displayed on the left side, with vibration peaks at values around 6 to 8Hz. Combining the normal measuring mode of the distance sensors with this vibration mode allows the monitoring of distance variations for a wide range of time scales, going from 100Hz vibrations to month-long variations.

5.3 Summary of Distance Calibration

As a result of the distance calibration, the uncertainties corresponding to the non-linearity and the repeatability remain always smaller than 20μm for all four distance sensors. This offers an accuracy 25 times better than the 0.5mm tolerance of the HEAT telescopes. Concerning the temperature dependence, the direct effect on the sensors was assumed to be negligible.

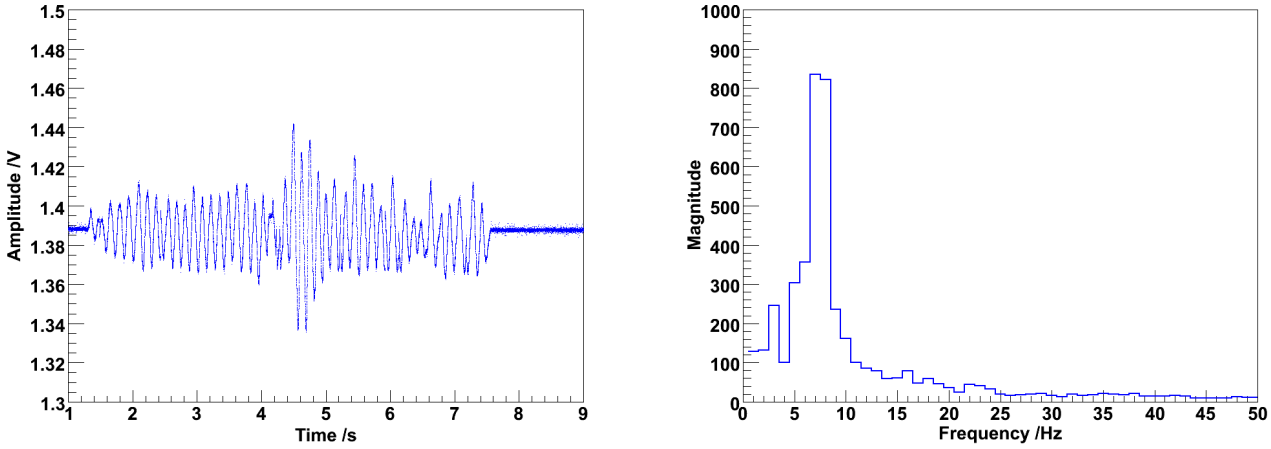

(a) (b)

Figure 51: (a) Example of a distance measurement showing a manually created vibration. (b) Vibration spectrum of the data displayed in (a).

6 Test Setup in a baseline FD

Having proven the capabilities of the Tilt Monitor, the system was finally installed in the Los Leones Fluorescence Detector building. This occurred during the week following the Auger Collaboration meeting that took place in Malargüe, Argentina, in November 2007. One requirement of the installation was not to interfere with or obstruct the actual measurements and maintenance of the Fluorescence Detector.

The telescope located at bay 6 in Los Leones is not capable of capturing nearly as much accurate data as the others. This is due to the fact that it covers a part of the sky illuminated by light coming from the town of Malargüe. Moreover, the field of view covered by this telescope is not covered by the Surface Detector array (see Fig. 8). For this reason, the data captured by this telescope does not contribute to the hybrid events. The combination of these two factors render this telescope less usable for the Pierre Auger Observatory. It was therefore the best choice for the placement of the Tilt Monitor.

6.1 Setup

First of all, the objective with this test setup was to find reasonably stable conditions for the sensors. A successful test for a normal FD telescope would demonstrate the feasibility of the Tilt Monitor for the nearly identical HEAT telescopes. The setup used in this test would then be copied for the enhanced telescopes. In this process,

it was important to position each component of the Tilt Monitor in an easily reproducible and reliable configuration.

All of the potentiometers were placed in different parts of the mirror structure (see Fig. 52). The objective was to provide redundancy in the different measurements. Once installed in a correct position, the measuring cables were fed through the square-shaped gaps between each piece of the fragmented mirror. Of the four distance sensors, two were placed on the mirror near its top, one on each side. Another one was placed in a more centered position on the lower part of the mirror structure. The fourth potentiometer was installed on the right side of the mirror at a height of about 1.80m.

Strong metal braces were used to hold the sensors in their final positions. As stated in chapter 4, the potentiometer cables were attached to longer carbon fiber cables ($\approx$1.5m). The cables fixed to the first three distance sensors were then attached to the telescope camera in different points. The fourth sensor was used to measure the distance separating the mirror from the window frame.

In order to avoid excessive pull on the sensors, the carbon fiber cables were connected to the sensors with magnets of a defined maximum load (3kg). This way, an accidental pull would simply separate the magnets instead of ripping the sensor cord. An alternative setup without this feature could potentially lead to damages in the camera, mirror or sensors. Was a person to inadvertently run into the almost invisible carbon fiber cables, the force resulting from this collision would be enough to separate both cables without damaging any component. An additional safety rope fixed to the mirror structure and to the sensor cable keeps the cable from reaching its maximum length. To attach the carbon fiber cables to the magnets, the cables were firstly glued to small screws. These screws were then inserted into the magnets.

After installing the distance sensors, three of the four inclination sensors were screwed onto L-shaped platforms. This made it possible to fix them on vertical pillars at different angles. Two of these platforms were screwed into the side of the central column of the mirror structure. Both at angles of 15^o to the horizontal (to simulate the same conditions needed in HEAT), but one on the top and one on the bottom. The third inclinometer was similarly placed on the side of the shutter at an angle of -15^o. The fourth inclination sensor was attached behind the camera using cable binders. A sideways installed L-shaped platform would most likely block a substantial amount of fluorescence light coming from the shutter during measurements. For this reason, this last sensor is the only one to lie on a horizontal plane, instead of the planned 15^o(-15^o) angle.

Each one of the wireless temperature sensors was positioned next to an inclinometer (except for the sensor on the shutter, which has no thermometer next to it). The

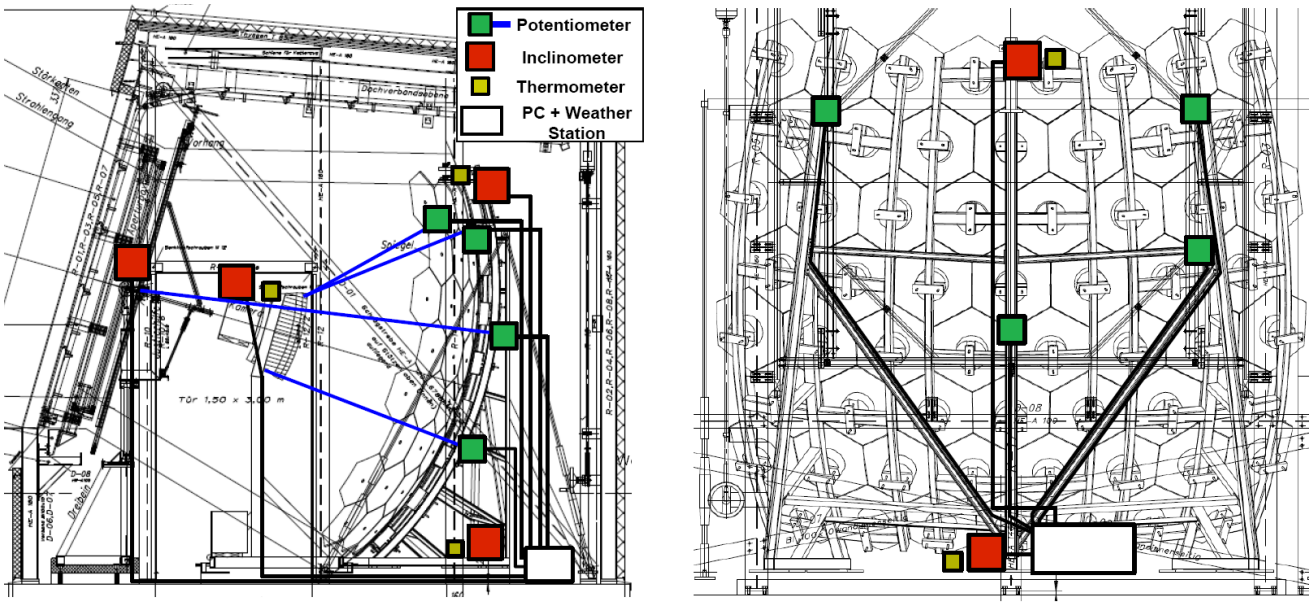

(a) (b)

Figure 52: Schematic view of the setup for the test measurements in the FD telescope (a) from one side of the telescope (b) from behind the mirror.

weather station was placed on the floor of the building, just behind the mirror, where it could receive the signal from all three thermometers.

Additionally, a UPS battery system was connected to the Tilt Monitor to provide a temporary power supply in case of power failures. It also avoided potential damages to the devices in the case of over voltages. Considering that such events occur fairly frequently in the Fluorescence Detector building, this precaution was very helpful. The FD team in Malargüe, which offered their constant support, provided the UPS system. Therefore, an additional UPS system needs to be bought as a replacement for the one used by the Tilt Monitor.

A schematic view of the placement of all sensors, including Tilt Monitor hardware box and weather station, can be seen in Fig. 52. Pictures of the resulting setup in Los Leones are shown in Fig. 53, 54 and 55. Note that the HEAT plans slightly differ from the real mirror configuration in Los Leones shown in Fig. 53, 54 and 55 (notably in the form of the mirror pieces). Despite these differences, the use of the HEAT plans to indicate the placement of each sensor is appropriate considering the objectives of the Tilt Monitor.

The Tilt Monitor hardware box presented in chapter 4 of this document was placed on a low wooden shelf for an easier maintenance and access to the laptop. To verify that everything was in its right place, the container was opened and every component inside was thoroughly inspected. Once every cable, including the ethernet cable, was plugged in, the system was finally ready to start its first measurements. The control panel of the TiltMonitor.exe executable functioned as planned, offering an optimal performance for all monitoring tasks. On the other hand, the DataTransf.exe application created, at first, some difficulties. These were however solved after a careful debugging and error checking. Fig. 56 (a), (b), (c) and (d) offer views of the container at different stages of the aforementioned checking process.

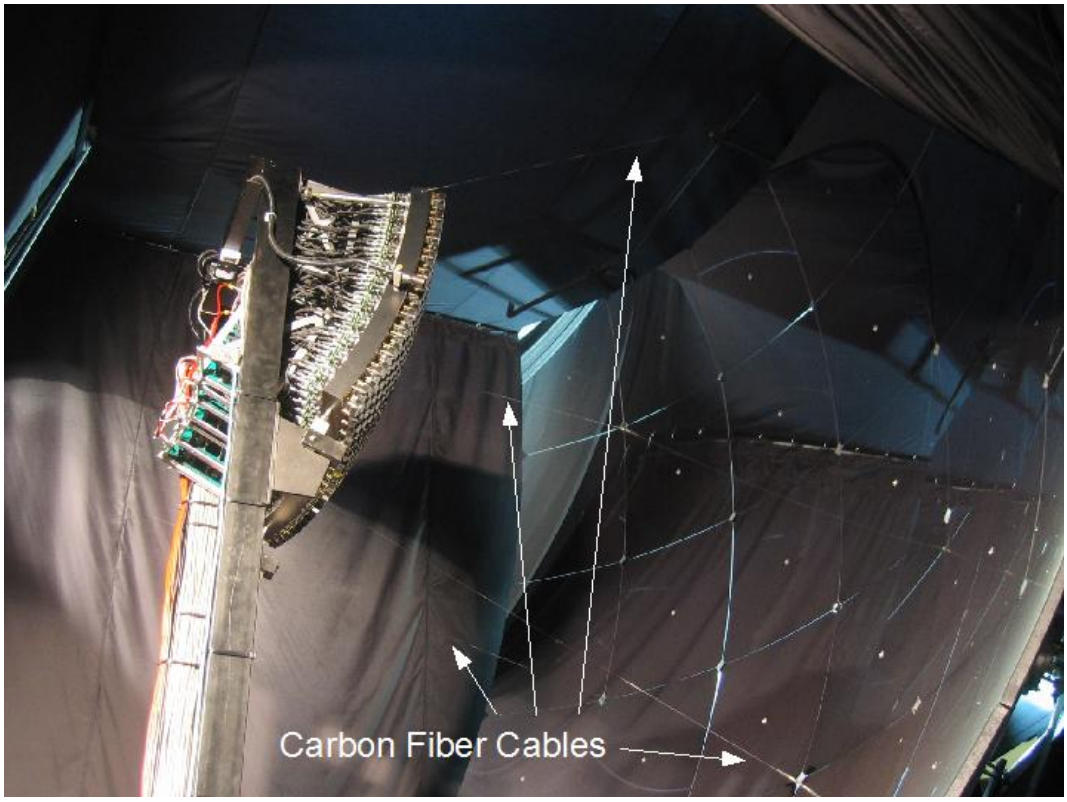

Figure 53: Picture of the installed setup, with the three carbon fiber cables going from the camera to the mirror, and the last one going from the mirror to the shutter.

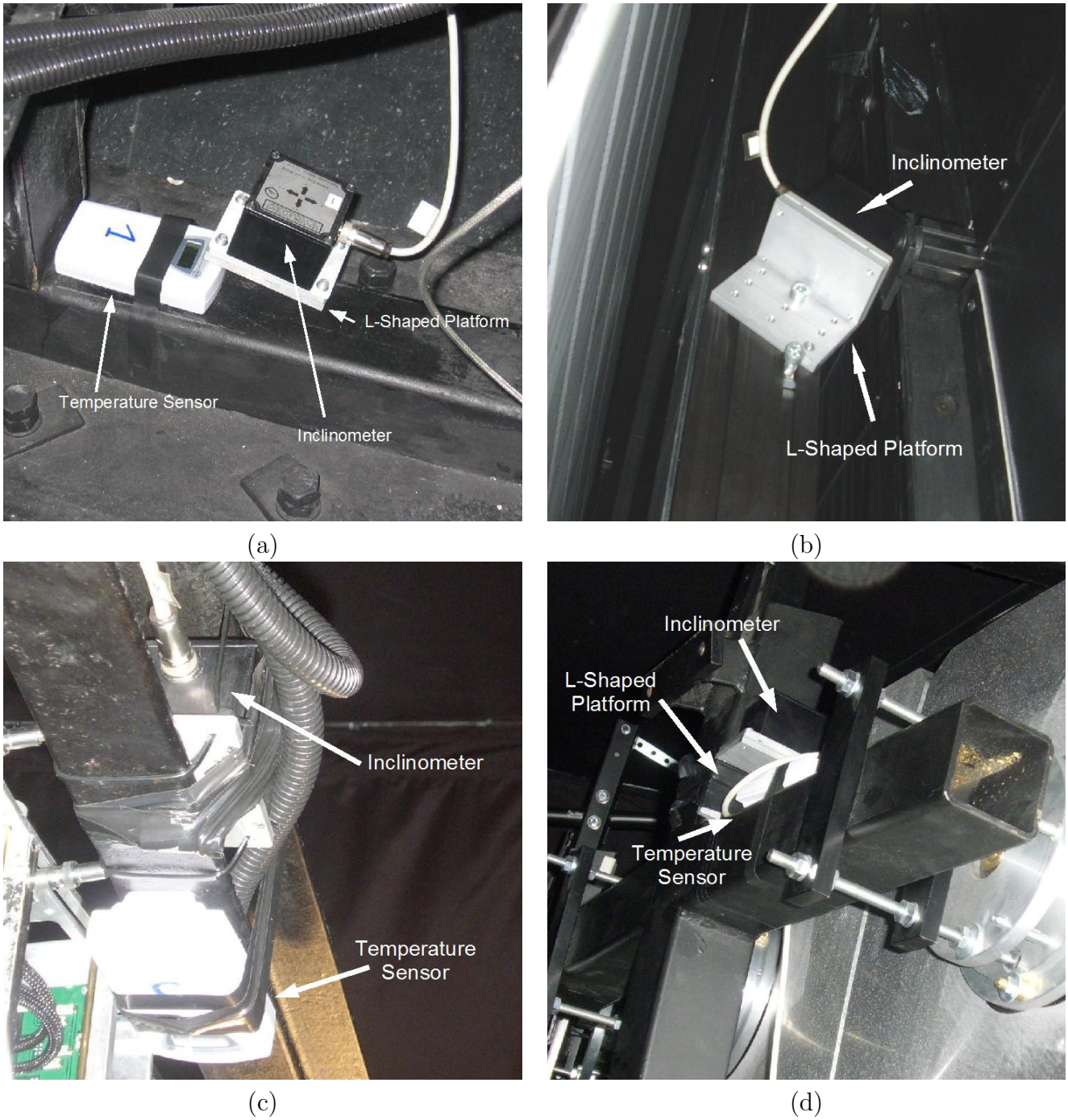

Figure 54: (a) Inclination and temperature sensors situated on bottom of the mirror. (b) Inclination sensor situated on the window frame. (c) Inclination and temperature sensors situated behind the camera. (d) Inclination and temperature sensors situated at the top of the mirror.

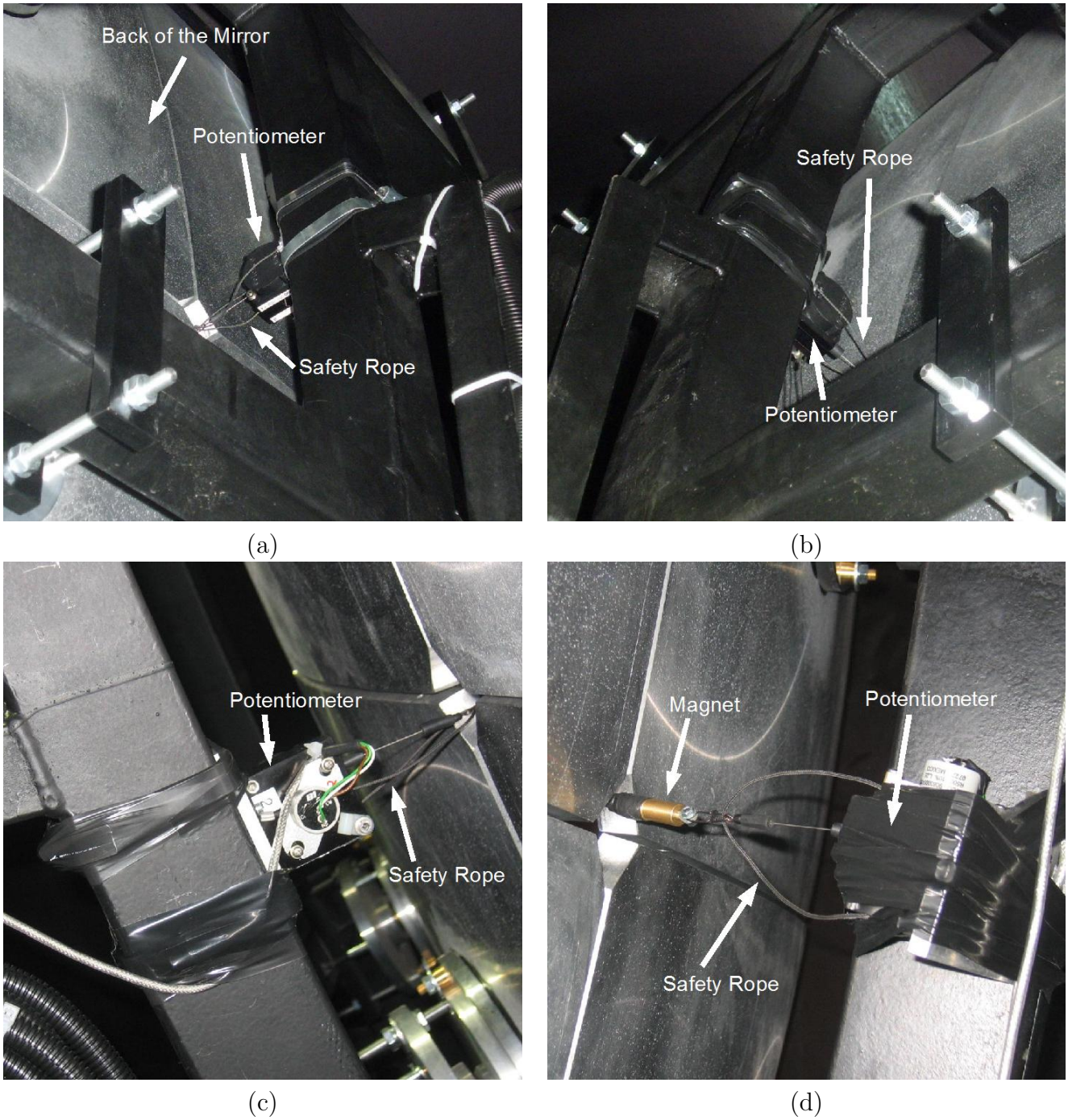

Figure 55: (a) Potentiometer situated on the top right side of the mirror. (b) Potentiometer situated on the top left side of the mirror. (c) Potentiometer situated in the center of the mirror. (d) Potentiometer situated on the right side of the mirror, to measure the distance shutter-mirror.

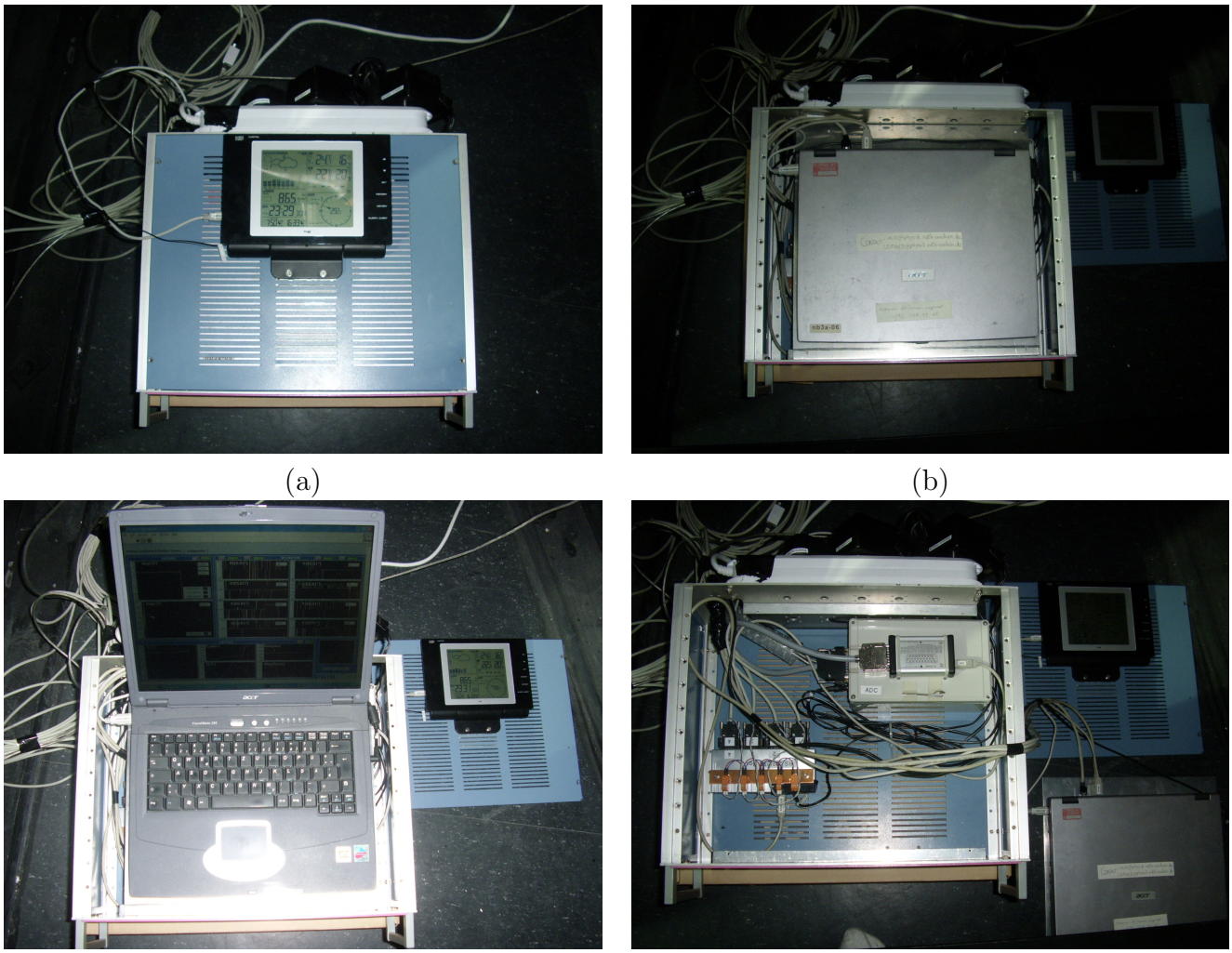

(a) (b)

(c) (d)

Figure 56: (a) Unopened hardware box of the Tilt Monitor, as it stands in normal measuring mode. (b) and (c) TiltMonitor open with the higher level containing the measuring notebook. (d) Lower level of the TiltMonitor containing the DAQ hardware (ADC, RS232 to USB serial).

6.2 Oscillation Test

Oscillation tests were performed as a reference for later measurements in the HEAT telescopes, but also as a method to evaluate the efficiency of the system under real circumstances. During this test, every component of the telescope was manually wagged in order to assess the mechanical stability to be expected from a baseline fluorescence telescope. Although this was done with the proper caution to avoid damaging any piece of equipment in the telescope, the results showed some significant fluctuations.

The test started with the manual oscillation of the camera from behind and in the direction of the mirror. The amplitude of the oscillations was small though significant enough to be measured by the Tilt Monitor. The process was repeated four times, each lasting a few seconds. Short pauses without any movement were left in between each oscillation. Afterwards, the camera was shaken from one side perpendicularly to the optical axis another three times. Then, the same treatment was applied to the shutter structure. Finally, vibrations on the mirror were manually induced in three different points. This was done from behind the mirror in this order: on the center, on the upper left corner and on the upper right corner. The entire procedure lasted less than 15 minutes.

Due to an impending planned power blackout shortly afterwards, the Tilt Monitor was safely turned off just after the end of the oscillation test. Hence, this kept the system from monitoring the evolution of the oscillations during the time following the test.

6.2.1 Analysis of the Inclination Data

The raw data that resulted from this measurement is plotted in Fig. 57. For a complete analysis, these plots show the inclination data for both X and Y axes. Oscillations are clearly visible in both axes after the 46 minute mark, especially for the inclination sensor placed on the camera. These variations on both axes reflect the chronological order in which the test was performed. This can be seen, for instance, in the signal of the sensor located on the camera. The X-axis of the inclinometer recorded oscillations of greater magnitude when the mirror was pushed along the same axis. The same applies to the Y-axis when the mirror was moved along this axis.

With variations greater than 2^o the camera oscillated 20 times more than permitted by the tolerance mentioned in chapter 3. The inclinometers placed on the shutter and on top of the mirror also measured oscillations, although of a lesser degree. Only the reference inclinometer placed on the bottom of the mirror recorded next to no amplitudes.

It has to be noted that these are not the definite results, as the data has not yet been corrected according to the results of the calibration. The effect of the correction on the overall structure of the measurements is, however, small (especially for the temperature correction, as there are no significant temperature variations during the test).

The unprocessed information diverges from the real inclination and has to be corrected according to the calibration. In a first stage, the corrected data set from the numerical calibration was used to recalculate the real inclination. A sort of linear spline function of the reference data set was created with ROOT. This offered the possibility to manipulate a continuous function instead of the discrete points of the numerical fit. The spline functions corresponding to each sensor are different, since there were four different sets. With these functions it was possible to link every possible measured point with its corrected counterpart.

Secondly, the influence of the temperature in the sensors had to be calculated. The effect for each inclinometer was estimated according to the data of the wireless thermometers located next to them. However, due to the number of wireless thermometers, this method was limited to three of the four inclinometers. Due to their proximity as well as to the similar height on which they were installed, the data from the camera temperature served as the reference for the sensor placed on the shutter. Using the temperature dependence of the sensors obtained in chapter 5.1.3, it was then possible to extrapolate the real inclination from the measured data:

$$I(T) = I(23.0^oC) + i(T) \tag{11}$$

where I(23.0^{o}C) corresponds to the inclination data after the linearity correction and

$$i(T) = a \cdot (T - 23^oC) \tag{12}$$

With a=-0.035^o/K:

$$i(T) = -0.035^o \frac{1}{^oC} \cdot (T - 23^oC) \tag{13}$$

Lastly, an estimation of the overall errors of these measurements was performed. This estimation had to take into account the independent sources of errors for non-linearity (u_{Lin}), repeatability (u_{Rep}) and temperature dependence (u_T= $\pm$0.005^o/K). The errors corresponding to the first two are supposed to remain constant and vary from sensor to sensor. As opposed to that, the error from the temperature dependence extrapolation increases with greater temperature variations. The total error was accordingly calculated using error propagation:

$$u_I = \sqrt{u_{Lin}^2 + u_{Rep}^2 + (\frac{\partial I}{\partial a} \cdot u_T)^2} \tag{14}$$

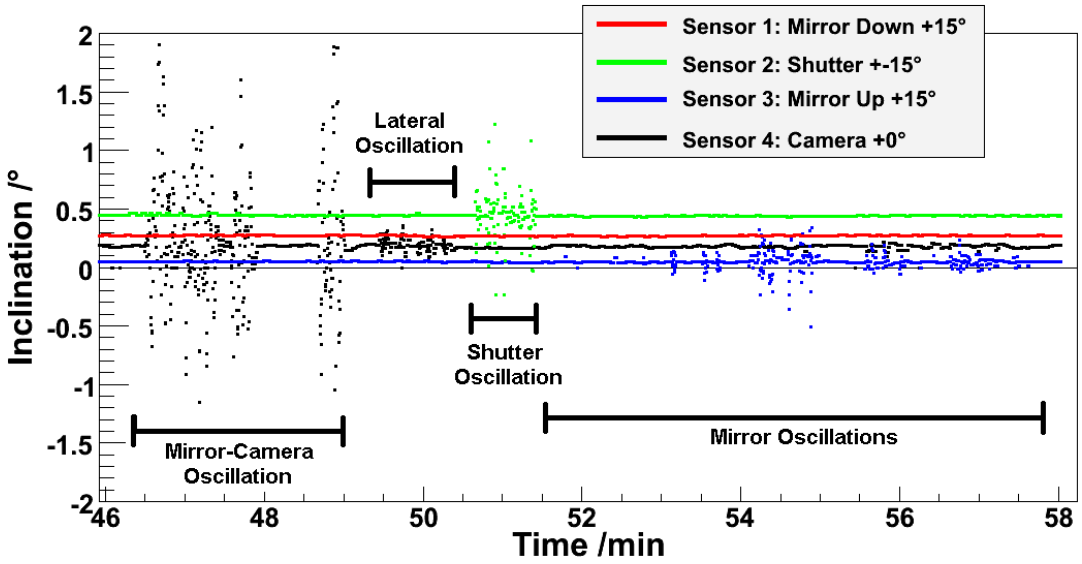

(a) X-Axis Inclination

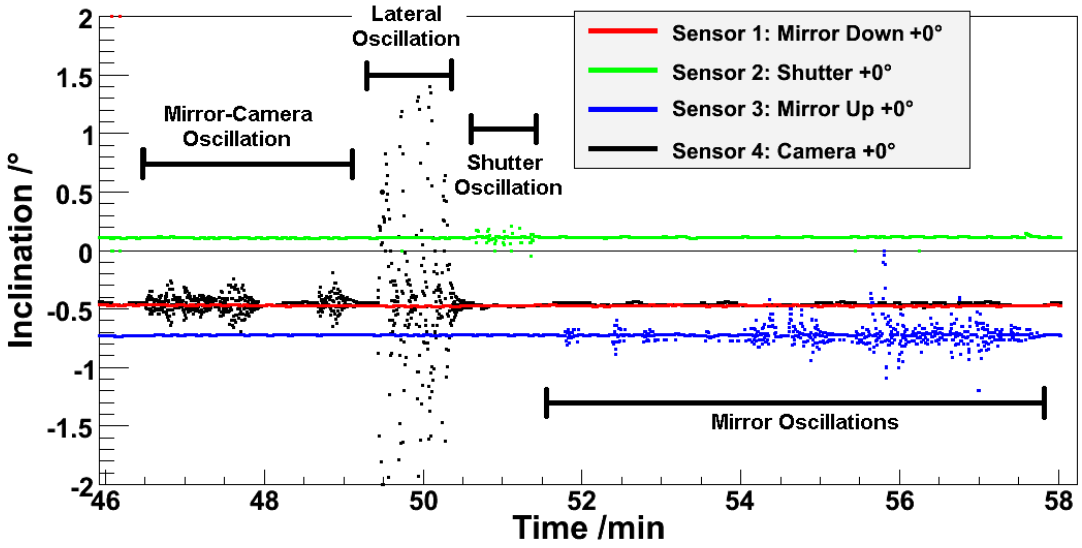

(b) Y-Axis Inclination

Figure 57: Raw inclination data from the 15 minutes long oscillation test for the (a) X and (b) Y axes.

and therefore

$$u_I = \sqrt{\sigma_{Lin}^2 + \sigma_{Rep}^2 + \overline{x}_{Rep}^2 + (u_T \cdot (T - 23^oC))^2} \tag{15}$$

The final result for both axes after the corrections is shown in Fig. 58. The form of the plot does not appear to change from Fig. 57 to Fig. 58. Nevertheless, a significant variation is visible for all sensors as a result of the temperature related correction. However, since the temperature is nearly constant due to the short time window, these variations are basically constant offsets.

6.2.2 Analysis of the Distance Data

After performing a correction similar to the one applied for the non-linearity of the inclination sensors, the voltages are finally transformed into distances. However, in the case of the distance measurements, the data does not need temperature corrections. The temperature independence leads to constant uncertainties. The total uncertainty on the measured distances only depends on the non-linearity and the repeatability. The error bars were calculated to complete the plot shown in Fig. 59.

Once again, the measurement shown in Fig.59 displays important oscillations that coincide with the different stages of the test. In particular, the three potentiometers attached to the camera registered significant variations over the duration of the test.

The form of the fluctuations varied depending on the direction in which the camera moved. For example, the potentiometers attached to the camera measured almost the exact same variations as the camera oscillated in the direction of the mirror. As the camera began to oscillate sideways, the distance variations for the two lateral sensors alternated accordingly. During this period of time, the potentiometer on the center measured next to no variations.

Later during the test, two subsequent bumps were measured, one for each one of the potentiometers located on the top of the mirror. These bumps also coincided with the corresponding stage of the test. Meanwhile, during the 15 minutes that the test lasted, only a relatively small variation was measured by the distance sensor attached to the shutter. However, the distance did not return to its original value afterwards.

Due to the nature of the oscillations caused on the camera, the potentiometers were probably unable to register the full amplitude. The method in which the data was registered was probably responsible for this. As explained in chapter 4.4.3, there are two distance measuring modes. One that measures up to 2000 data points per second (vibration measuring mode) and one that averages these points every sec-

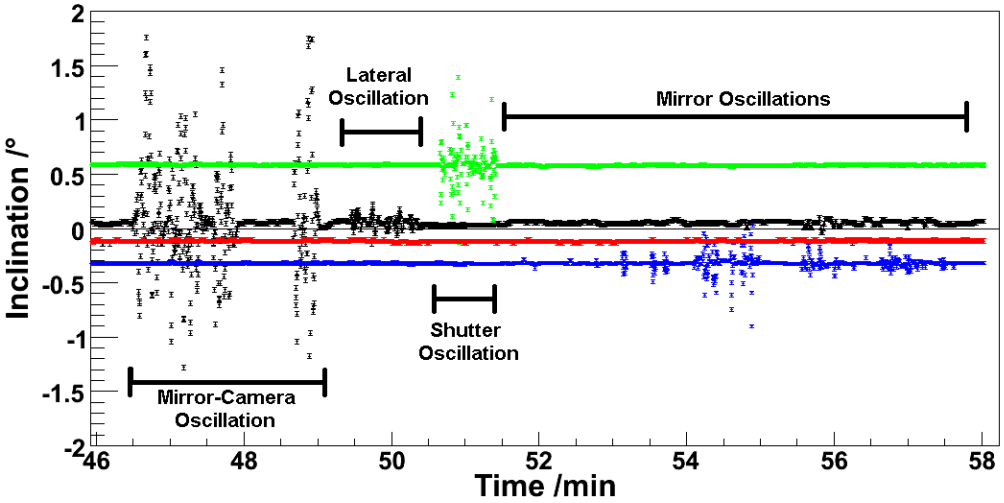

(a) X-Axis Inclination

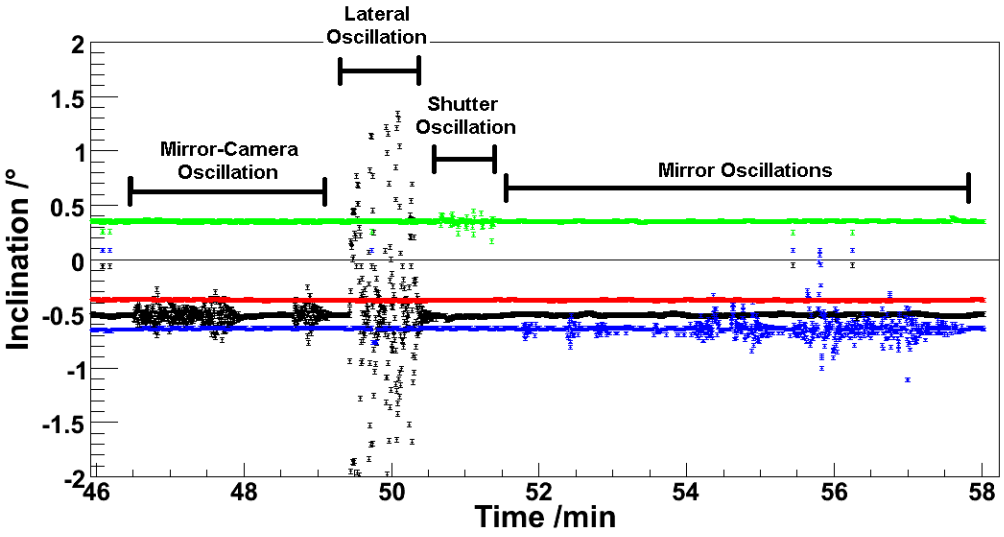

(b) Y-Axis Inclination

Figure 58: Corrected inclination data from the 15 minutes long oscillation test for the (a) X and (b) Y axes.

ond (long duration measuring mode). Unfortunately, during this test, the monitor operated in the averaging mode. The resulting limited time resolution lead to the recording of smaller variations for oscillations with frequencies higher than 1Hz. At one point, however, around the 47 minute mark, a peak stands out from the previous variations and is most likely the result of a synchronization of the oscillations with the measurements.

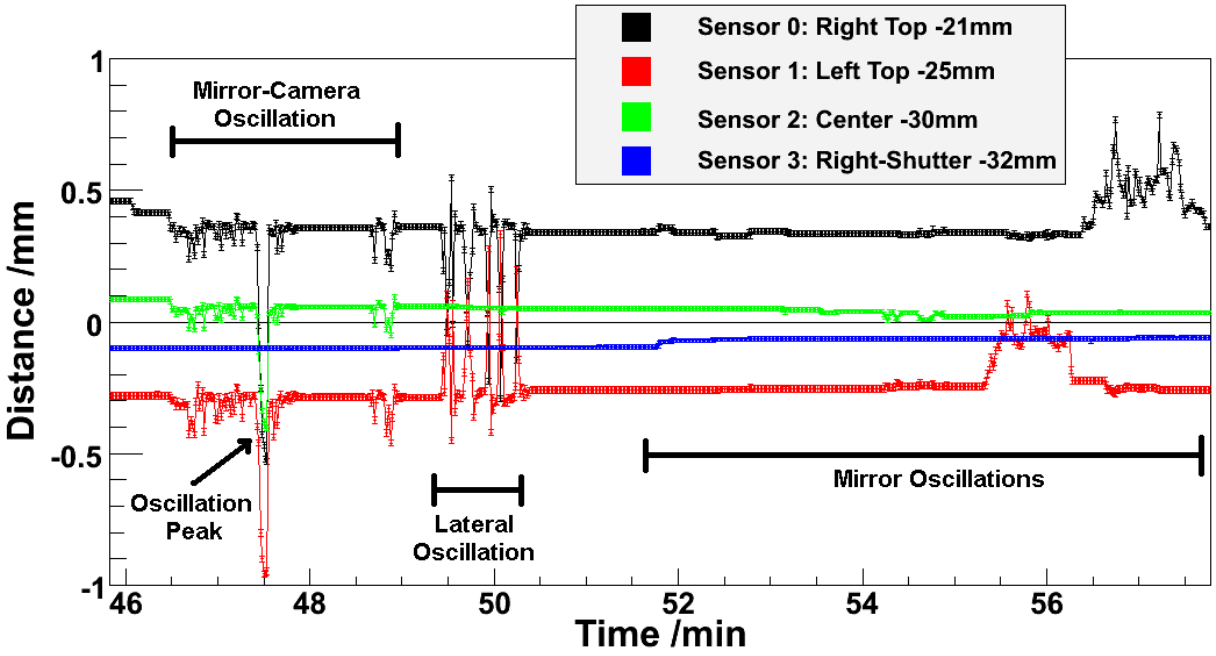

Figure 59: Distance data from the oscillation test, corrected according to the calibration.

Note that the results of the oscillation test are mainly useful as a good qualitative check of the performance provided by the system.

6.3 Long Duration Measurements

Five days after the oscillation test and the power failure that followed, the system was brought back online. Since then, the transfer of data only suffered minor interruptions. These were mostly caused by short power failures that affected the internet connection of the Fluorescence Detector building. During these blackouts, the computer of the Tilt Monitor was kept from shutting down by the UPS battery connected to the system.

In this chapter, the data corresponding to four weeks of measurements will be presented. Once analyzed, the data will provide an estimation of the behaviour to be expected from an Auger baseline telescope. This information is necessary in order to later evaluate the differences between the current and the enhanced telescopes for longer periods of time. It was also important in order to test the reliability of the sensors.

6.3.1 Inclination

The plot corresponding to the raw inclination data for the X axis is presented in Fig. 60. Each one of the colors corresponds to one of the inclinometers. The temperatures are displayed as dotted lines of the same color as its respective inclinometer. Their values can be read from the vertical axis on the right side of the diagrams.

As expected, for the raw data, there appears to be a correlation between the temperature and the inclination. Clear 24 hour long structures can be seen for three of the four inclinometers. The inclination fluctuations caused by the typical temperature changes between the night and the day (ΔT$\approx 2^o$C) lead to significant inclination variations of up to 0.08^o. The sensor located on the bottom of the mirror did not register these cycles, as the temperature on the ground does not follow the same pattern. The sensor does, however, register peaks of up to more than 0.1^o (near the 480 hour mark, see Fig. 60) that correspond to sudden temperature changes. The entire form of the temperature measurement is, in fact, reflected in the inclination measurement. Other than the fluctuations that apparently result from temperature variations, the inclination remains reasonably stable for all sensors.

Note that the inclination data plotted in the diagram does not directly correspond to the measured inclination data, but to its mean value for intervals of roughly 20 seconds. The reason for this lies in the resolution and the size of the data. As a result of the 0.01^o resolution, a plot using every data point would have shown a vast amount of points, distributed along only three or four different levels, leaving 0.01^o wide spaces between them. Furthermore, due to the large time scale, the shape and density of the four different curves would have been difficult to discern. The use of the mean values to display the data provides therefore a practical solution to all these problems.

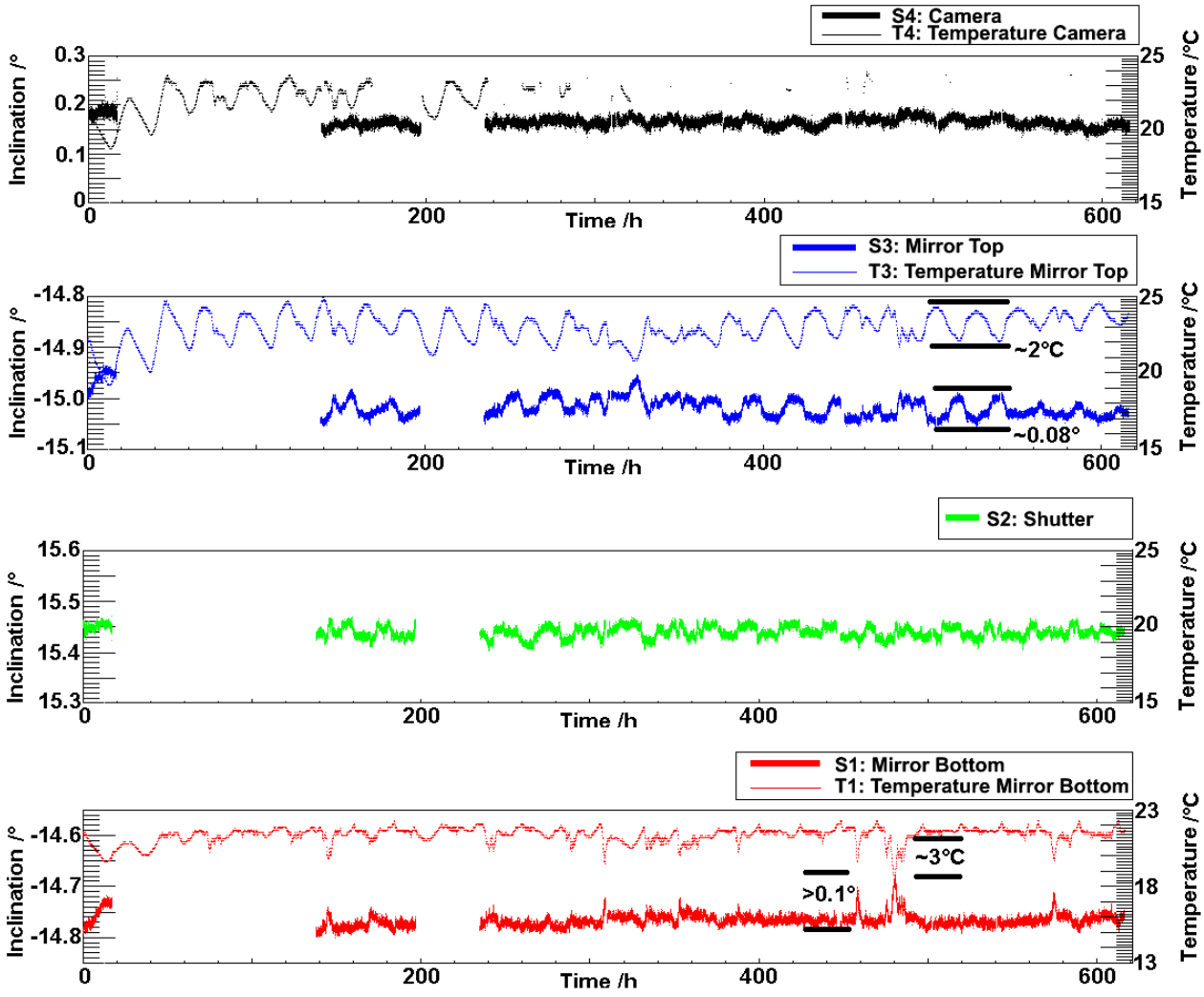

Figure 60: Uncorrected inclination data extracted from the long term measurement, for the X-axis.

To correct the inclination data collected during the long duration measurements, the same method used for the oscillation test was applied. First, using a spline function, the non-linearity was corrected. Then, the effect of the temperature dependence was calculated and accordingly taken into account.

Unfortunately, after the first days of measurements, the weather station started experiencing difficulties receiving the signal from the temperature sensor located on the camera. For this reason, the inclinometer next to it had to be corrected using

information provided by another wireless temperature sensor. Taking into account their similar temperature structure, the sensor on top of the mirror was used to extrapolate the temperature variations at the location of the two inclinometers with no temperature measurements.

In fact, the temperature measured by the wireless thermometers basically depends on the height on which the thermometer is installed. Thermometers situated at a higher level measure, during the day, higher temperature peaks than the sensors located near the ground. This is the result of the relatively thin thermal insulation on the roof, which leads to stronger temperature fluctuations on this section of the building. On the other hand, the air conditioning system, located at ground level, has a stranger influence on the temperature of the lower section of the building. During the night, however, the temperature tends to remain similar for all sensors, as there is no outside influence on the temperature of the building.

The wireless thermometer located on the top of the mirror lies at a slightly higher level than the two other thermometer-less inclinometers. Consequently, the amplitudes of the temperature fluctuations at its location are also higher. Its data was nevertheless used for their temperature-related correction, as it provides the best temperature approximation in these two other locations.

The corrected inclination data is presented in Fig. 61. The areas under slightly brighter colors describe the uncertainty on the absolute value of the inclination, according to the calibration. For sensors 1 and 3, the correction results in significant reductions of the temperature correlation. The amplitudes of the fluctuations do not exceed 0.05^o and there is only a small temperature correlation. On the other hand, sensors 2 and 4 display important fluctuations, with amplitudes even higher than for the raw data.

Hence, the corrected data from the sensors benefiting from an accurate temperature measurement (sensors 1 and 3) appears to correctly reflect the real inclination, as the resulting curve is almost flat. This observation is made under the assumption that no significant inclination is supposed to occur for the baseline telescope. At least for the reference inclination measurement of the sensor placed on the bottom part of the mirror structure, this should most certainly be the case. The temperature-related corrections for sensors 1 and 3 are therefore optimal. For large temperature changes, for instance, in the 480 hour mark, the variation observed in the raw data is now negligible. However, for the two remaining inclinometers, the temperature-based adjustment results in a clear overcorrection of the data. This is not the result of a variation of the temperature dependence as a function of the inclination, since additional measurements during the calibration demonstrated a consistent temperature dependence for inclinations of 0^o, $\pm 5^o$ and $\pm 10^o$. The overcorrection probably stems from the absence of accurate temperature data for these inclinometers. A separate

determination of the temperatures for all four inclinometers is hence not only useful, but required, in order to avoid a temperature-related bias in the correction.

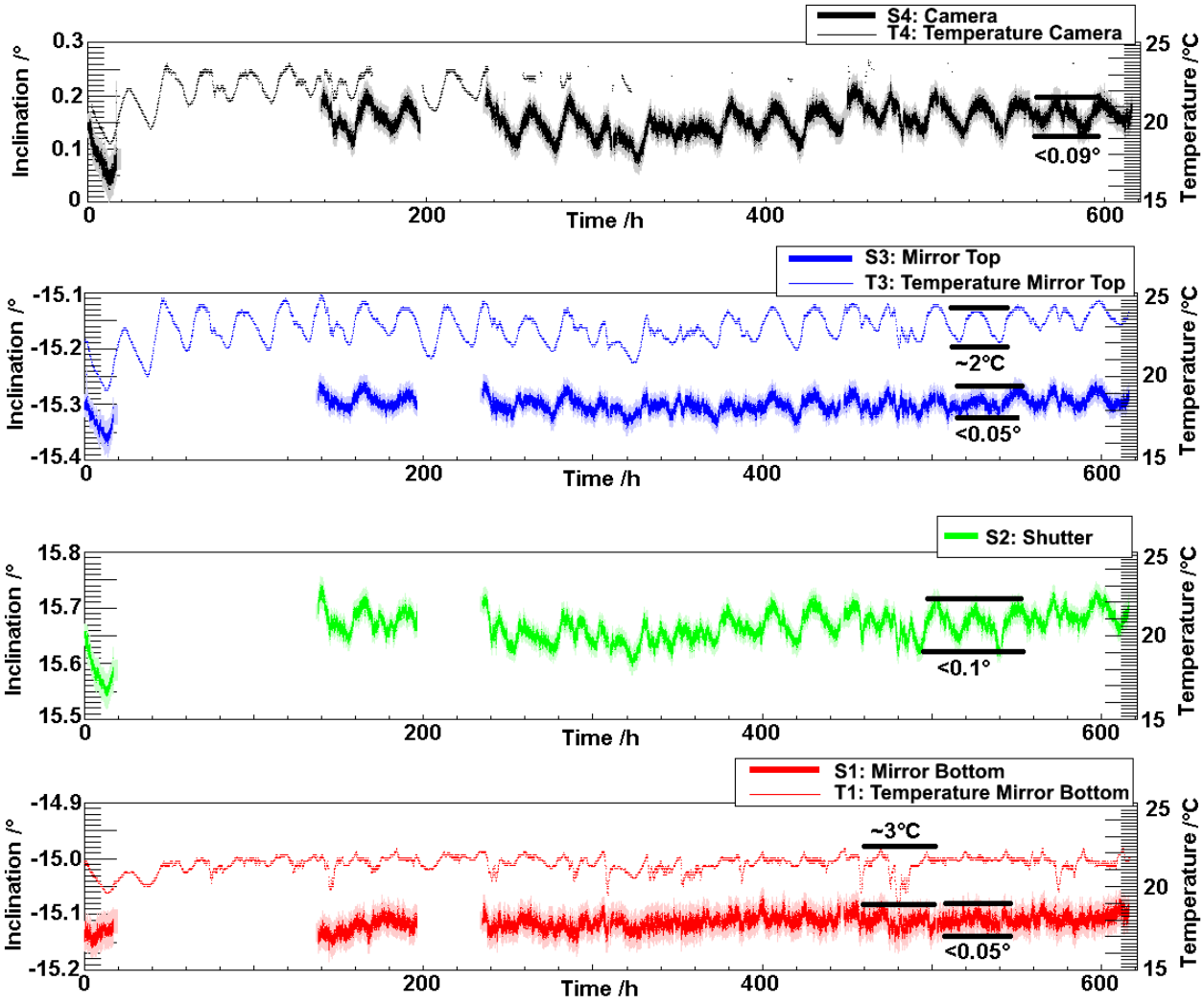

Figure 61: Corrected inclination data extracted from the long term measurement, for the X-axis.

Finally, Fig. 62 displays the inclination data for the Y-axes of the four inclinometers. After the linearity correction and the individual temperature correction, the results are similar to those for the X-axis. Much like for the X-axis, the data from sensors 1 and 3 appear to be almost flat, with fluctuations lower than 0.05^o, while the remaining two plots show variations of a larger scale (amplitudes go up to 0.09^o). This is once more probably due to the bias caused by the temperature uncertainty.

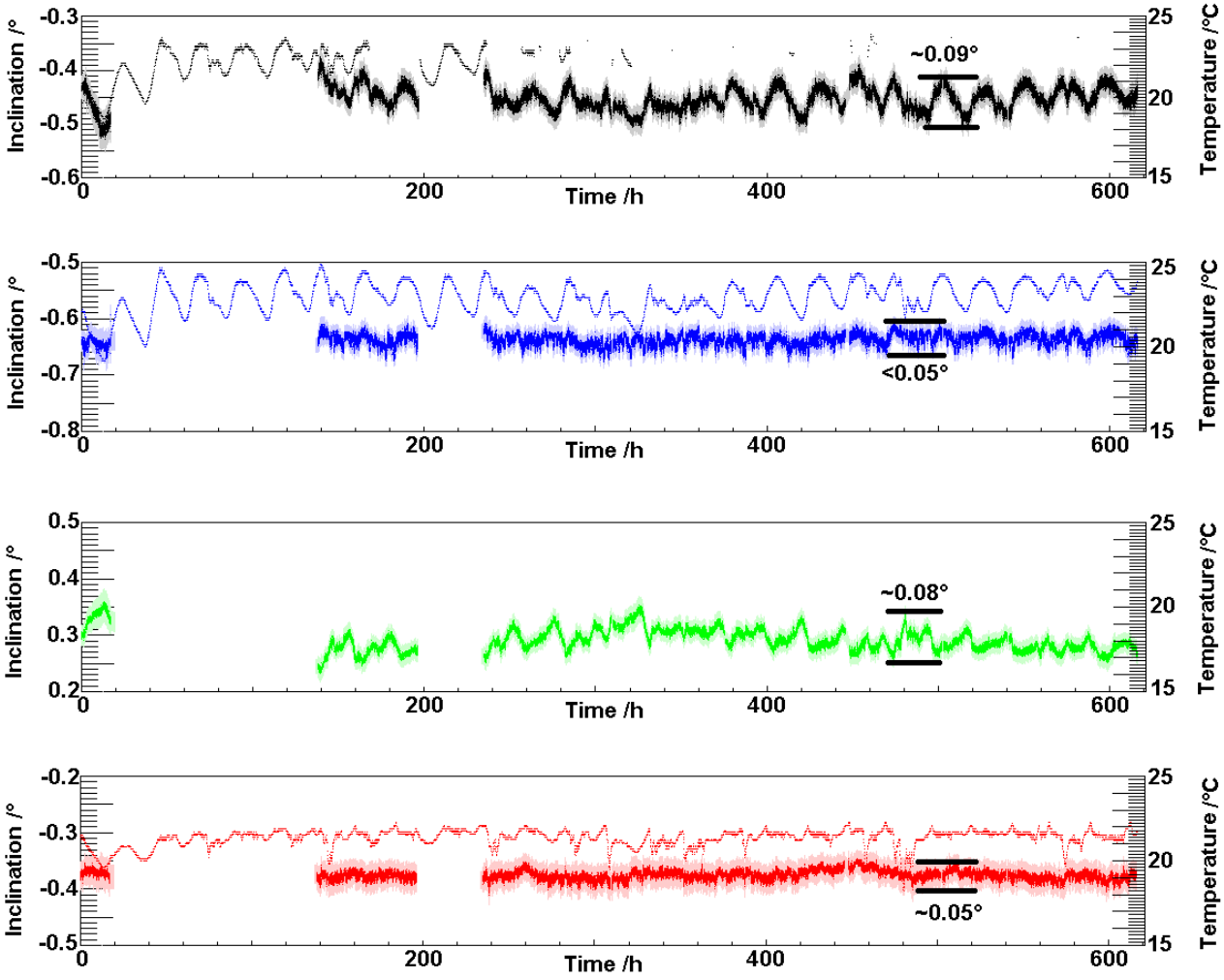

Figure 62: Corrected inclination data extracted from the long term measurement, for the Y-axis.

The results of the long duration measurement show that the inclinometers are able to detect potential deformations of the telescope structure with a satisfactory reliability. For the over corrected sensors, the inclination fluctuations in the Los Leones baseline telescope do not exceed the 0.1^o limit. For the two appropriately corrected sensors, they even remain under 0.05^o.

6.3.2 Distance

The long term data corresponding to the calibrated distance measurement is shown in Fig. 63. Sensors 0, 1 and 2, the three sensors that measure the distance between the camera and the mirror, show similar structures. This suggests that all three sensors fulfilled their objective and measured the real distance variation. Most of the distance fluctuations visible in Fig. 63 seem to be somewhat correlated to the temperature changes measured by the weather station. However, there appear to be other fluctuations not directly correlated to temperature variations. The amplitude of all fluctuations typically remains under 70μm.

The instability of the input voltage of the potentiometers could be responsible for the fluctuations uncorrelated to the . However, the voltage stabilization performed by the microBOX practically excludes this possibility. In order to be completely sure, future tests in the HEAT telescopes will include the measurement of the input voltage.

The total distance variation registered by sensors 1 and 2 does not exceed 140μm(Δx_2 < 130μm for sensor 2 and Δx_1 < 140μm). This remains considerably under the 0.5mm tolerance value mentioned in chapter 3. As such, the variations measured in the baseline telescope are uncritical.

However, the signal coming from the potentiometer attached to the top right side of the mirror (sensor 0) appears to continuously decrease with time. This slow descent could be caused by a gradual detachment of the cable or the sensor itself from its fixation (note that this effect could also be caused by a malfunctioning of the sensor itself, in which case a replacement of the sensor would be inevitable).

In Fig. 64, a subtraction of the data from the defective sensor from the distance measured with one of the other two sensors reveals a level-based structure for this decrease. Although the total variation over a period of almost one month does not exceed 500μm, the problem nevertheless causes a number of difficulties. For instance, in order to calculate the exact distance variation in the optical axis, accurate data from all three of the distance sensors is required.

Concerning sensor 3, the sensor that measures the shutter-mirror distance, the lower diagram in Fig. 63 reveals a different structure than the one measured by the first three sensors. This demonstrates that the window frame and the camera suffer two completely different types of deformations. While the camera remains relatively stable, barring minor fluctuations, the window repeatedly experiences more abrupt changes. The changes in question tend to involve variations of similar amounts of distance, roughly 100μm to 200μm. These occur suddenly and go in both directions, with a total distance variation that does not exceed 600μm during the whole measurement. Moreover, the changes do not appear to occur at random intervals, but

take place apparently after similar amounts of time. Fig. 63 supports this by showing that these changes are likely correlated with day-night cycles in the telescope. The cause could therefore be related to the working schedule of the telescope. Note that sensor 3 also occasionally registers changes similar to the ones measured by the three other potentiometers. These changes can therefore be attributed to mirror movements.

Although substantially greater than the variations measured by the other three sensors, the fluctuations measured by sensor 3 remain almost insignificant considering the 5mm tolerance of the shutter-mirror distance.

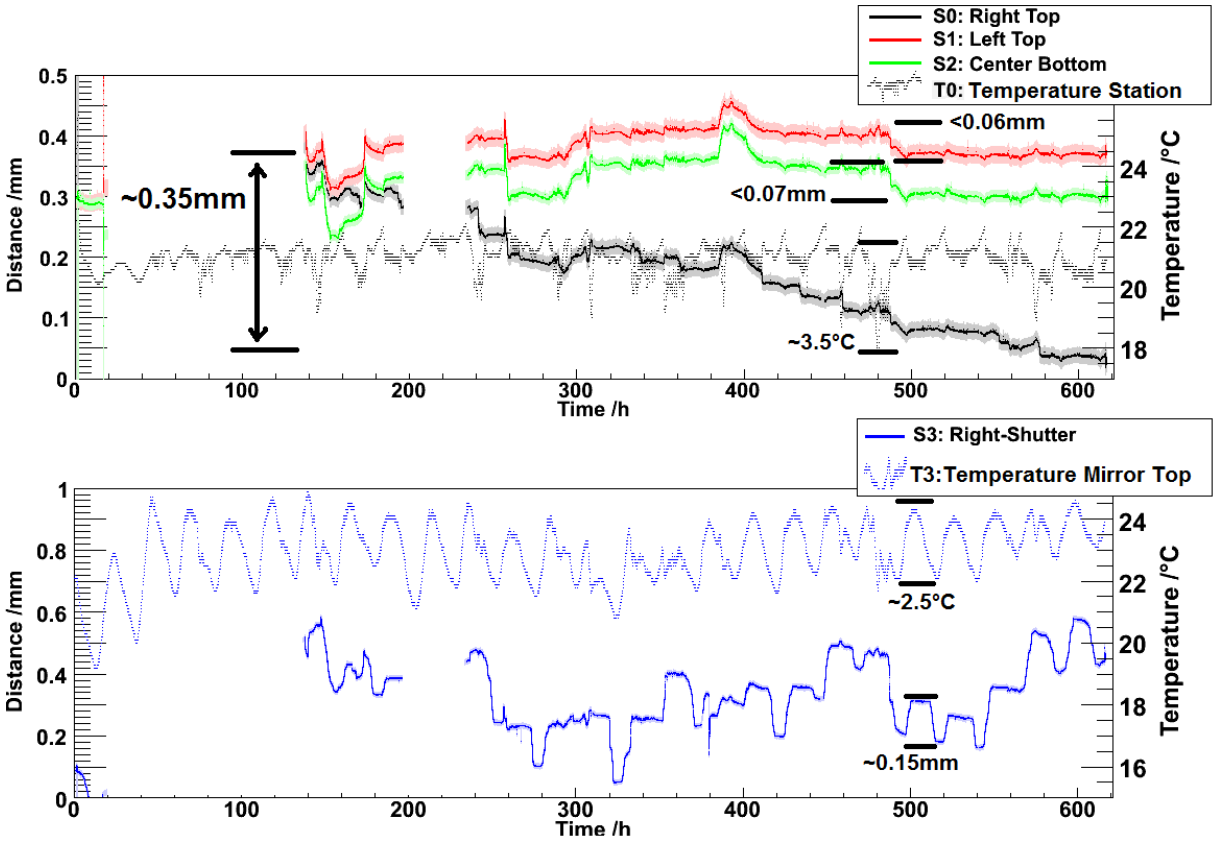

Figure 63: Corrected distance data for the long duration measurement.

In order to better evaluate the measured deformation, a zoom of the plot for a 60 hour long time interval is shown in Fig. 65. For shorter periods of time, the temperature correlation is significantly more apparent. The form of the temperature curve is the direct result of the temperature changes, probably induced by the air conditioning system of the FD building. This system typically follows one hour long

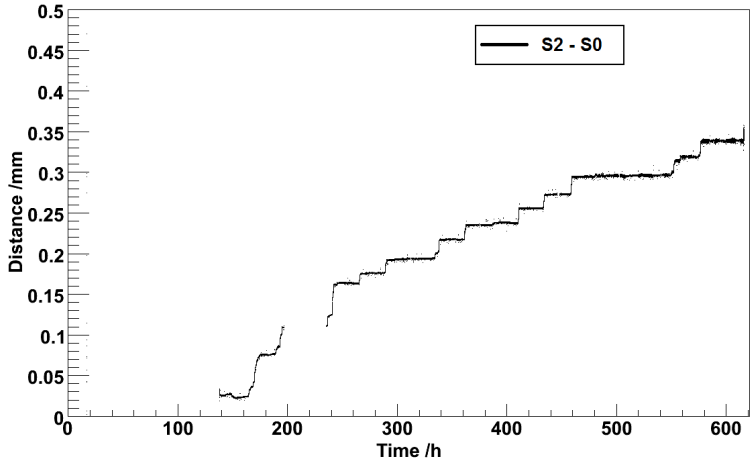

Figure 64: Data from S0 subtracted from data from S1.

cycles during the day in which it is repeatedly activated and deactivated in order to keep the room at the same temperature. The small but consistent temperature variations probably cause a deformation of the metallic structures that can be measured with the potentiometers ($\Delta x < 10\ \mu m$). In fact, the structure of the measured distances displayed in Fig. 65 is strikingly similar to the separately measured temperature data. Note that, due to the reduced resolution and the low scale of the fluctuations ($\Delta T = 1^oC$), the temperature sensitive inclination sensors measure no such variations. In addition to all this, the curves shown on the lower diagram of Fig. 65 further suggest the correlation between the step like structure measured by sensor 3 and the 24 hour cycles in the temperature.

6.3.3 Distance Variations in the Optical Axis

The data measured by the sensors does not, however, correspond to the exact distance variation in the optical axis, which is the relevant parameter. To determine the maximal camera-mirror distance variation in this axis, a calculation involving the data from all three sensors and the geometry of their positions in the telescope is necessary.

With the projection of the real distance along the three sensor-camera axes, it is possible to approximately determine the distance variations along the optical axis. This has to be done in two steps. First, the movement along the plane formed by the camera, sensor 0 and sensor 1 has to be determined. Then, the same process can be repeated for the plane composed by the optical and the vertical axes.

Sensors 0 and 1 stand at exactly the same height and their distance to the optical axis is for both the same. The axes connecting these two sensors and the camera form an angle of β=58^o with each other. For a better visualization of the

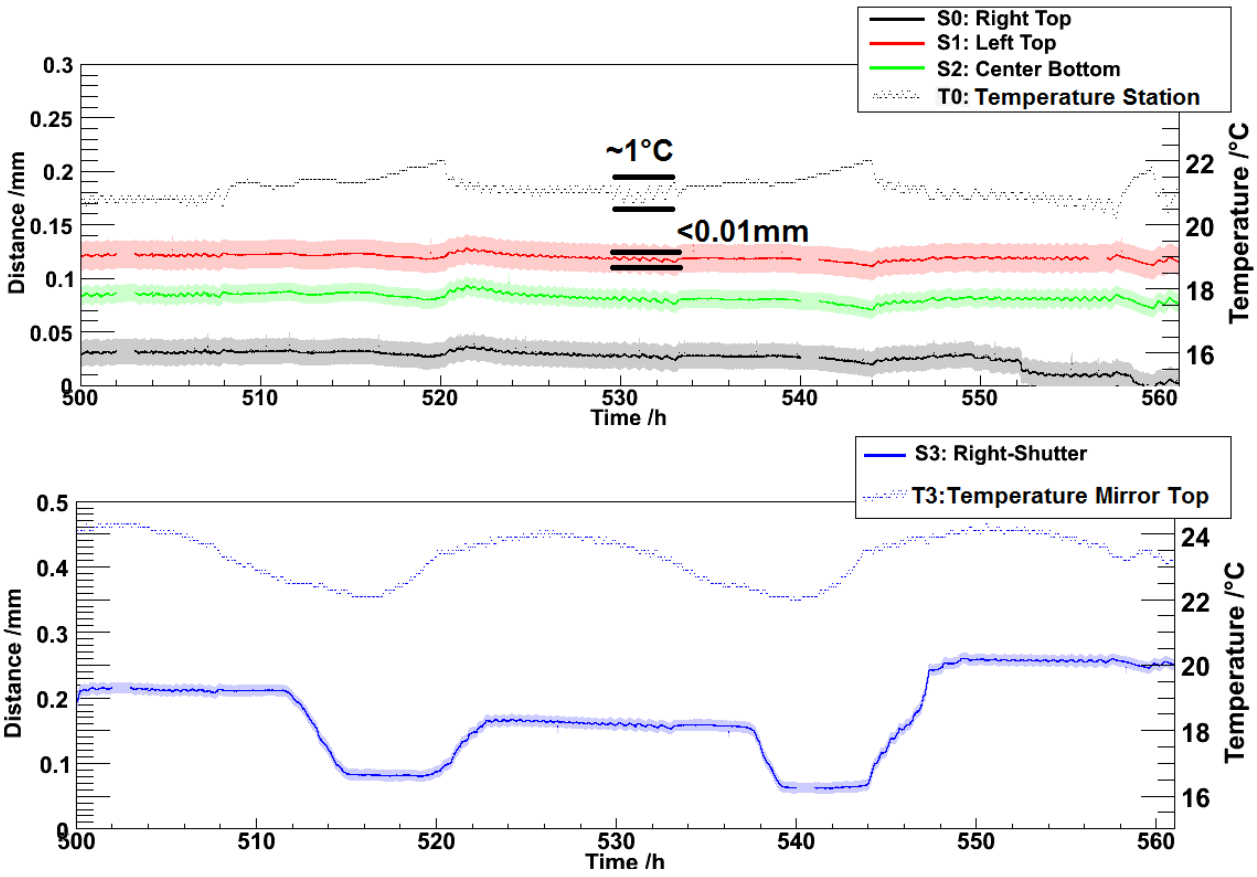

Figure 65: Zoom of the corrected distance data for a 30 hour long period of time.

geometry involved, a schematic representation is shown in Fig. 66. Assuming a random movement of the camera described by a vector $\vec{d}$, its projection in the camera-sensor0-sensor1 plane (Fig. 66 left) is given by another vector $\vec{d_1}$. Using the distances measured by sensor0 (variable $k_0 = \left|\vec{k_0}\right|$) and sensor1 (variable $k_1 = \left|\vec{k_1}\right|$), we know that:

$$k_0 = d_1 \cdot cos(\alpha) \tag{16}$$

and

$$k_1 = d_1 \cdot cos(\alpha + \beta) \tag{17}$$

Where $d_1 = \left|\vec{d_1}\right|$ and α is the angle between $\vec{d_1}$ and $\vec{k_0}$. $\vec{k_0}$ and $\vec{k_1}$ are thus the projections of $\vec{d_1}$ in their respective camera-sensor axes. Equations 16 and 17 lead to:

$$k_1 = k_0 \cdot cos(\beta) - \sqrt{d_1^2 - k_0^2} \cdot sin(\beta) \tag{18}$$

and therefore

$$d_1 = \sqrt{\left(\frac{k_0 \cdot cos(\beta) - k_1}{sin(\beta)}\right)^2 + k_0^2} \tag{19}$$

and

$$\alpha = arcos(k_0/d_1) \tag{20}$$

Knowing the distance d_1 and the angle α it is now possible to calculate the distance variation $d_2 = \left|\vec{d_2}\right|$ in the axis that bisects the angle β. With this parameter, the same process previously performed can now be repeated for the camera-sensor2-vertical plane (Fig. 66 right). We now combine the calculated projection d_2 and the data measured by sensor2 (parameter $k_2 = \left|\vec{k_2}\right|$) in order to calculate the total distance variation $d_3 = \left|\vec{d_3}\right|$ in this plane:

$$d_2 = d_3 \cdot cos(\alpha_2) \tag{21}$$

$$k_2 = d_3 \cdot cos(\alpha_2 + \beta_2) \tag{22}$$

$$d_3 = \sqrt{\left(\frac{d_2 \cdot cos(\beta_2) - k_2}{sin(\beta_2)}\right)^2 + d_2^2} \tag{23}$$

The projection $\vec{k_2}$ forms an angle $\beta_2 = 42^o$ with the projection $\vec{d_2}$, and an angle $\gamma = 8^o$ with the optical axis. As the three axes stand on the same plane, a simple calculation leads to the distance variation in the optical axis:

$$d_{Opt} = d_3 \cdot cos(\beta_2 + \alpha_2 - \gamma) \tag{24}$$

As it stands, the data from the defective sensor 0 interferes with this process. However, the calculation of the distance variation in the optical axis is possible for smaller time intervals, where sensor 0 did not register any sudden drop that would

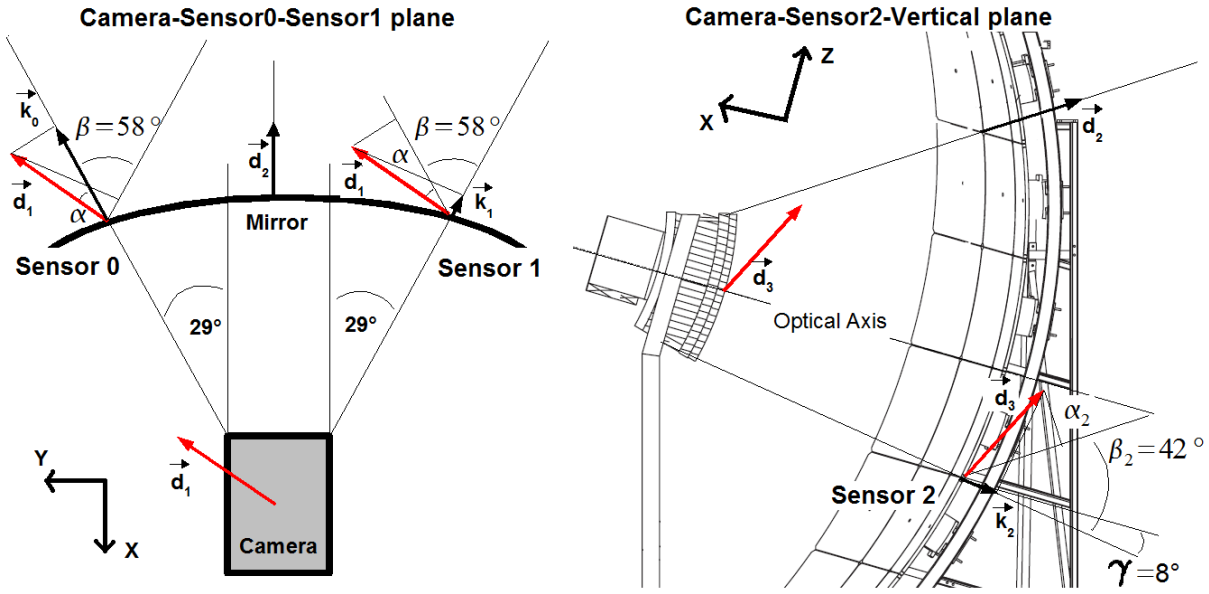

Figure 66: Schematic representation of the camera-mirror movement.

otherwise bias the result.

For instance, analyzing the interval of the long term measurement between the 380 and 400 hour mark provides a good idea of the maximal distance fluctuations in the optical axis. Fig. 63 shows that there are significant distance fluctuations for this period of time, while Fig. 64 demonstrates that none of the sudden drops measured by sensor 0 occur in this range. The results of the analysis corresponding to the calculation of the distance variation in the optical axis in this time range are presented in Fig. 67. The four different curves show the variations measured by sensor 2 as well as the calculated variations for the X,Y and Z axes (where X corresponds to the optical axis). The plot demonstrates that the deformations occur mostly in the optical axis ($\Delta X_{max} \approx 60 \mu$m), while the variations in the two other axes remain considerably less significant ($\Delta Y_{max} \approx \Delta Z_{max} \approx 5 \mu$m). This appears to be consistent with the original data of the sensors.

Finally, note that the axis connecting the camera with sensor number 2 forms a 8^o angle with the optical axis. Therefore, the data from this sensor already provides a reasonable approximation of the distance variation in the optical axis. The results shown in Fig. 67 confirm this, as there is practically no difference between the theoretical movement in the optical axis and the movement measured by sensor 2.

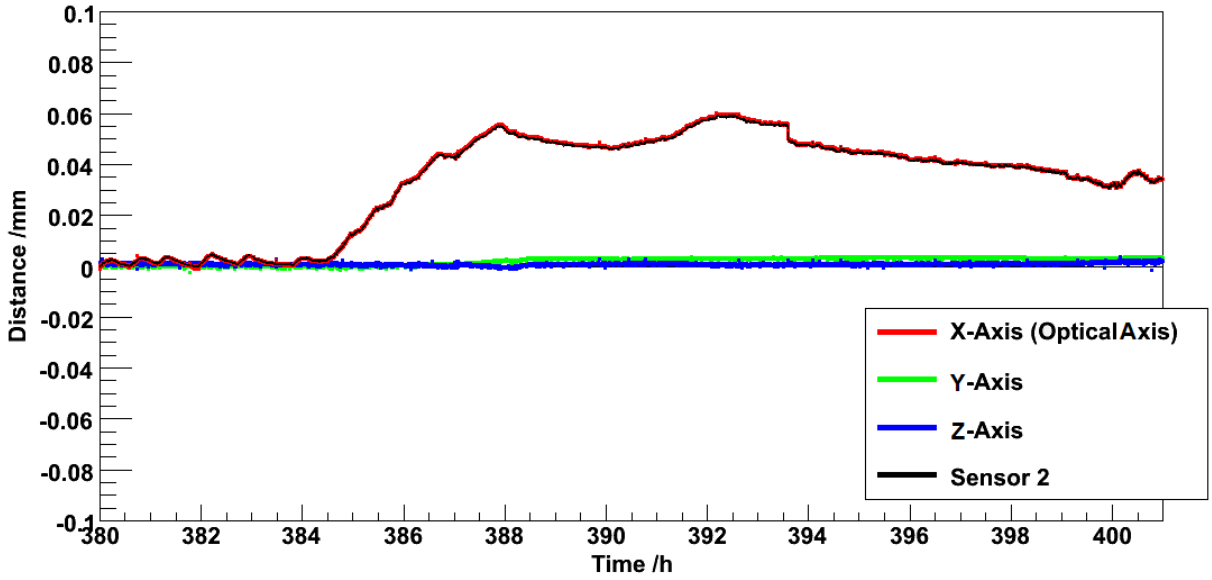

Figure 67: Distance variations in x,y and z axes for the time period between the 380 and the 400 hour mark. In order to compare the results, the data measured by sensor 2 is also shown here.

6.3.4 Vibration Spectrum

As a final part of the experiment, the data measured under the vibration mode was analyzed. The data covers the same period of time analyzed in chapter 6.3.2. Every 300 seconds, the Tilt Monitor recorded the distance measured by sensor 2 under a higher sampling rate, during one second. The number of data points per measurement varies between 1200 and 2000. In total, 5942 seconds of data were avalaible. Intervals of roughly five minutes separate each fast measurement. The spectrum shown in Fig. 68 covers the vibration frequency range between 1 and 100Hz. For higher frequencies, the spectrum is filled with noise, probably due to the limited sampling rate of the ADC as well as the nature of the variations in the input current (see Fig. 69). It is therefore difficult to recognize possible structures above this level, though there appears to be a short vibration increase for frequencies just above 100Hz. This could however also be the result of the noise. Except for this feature and an initial bump for frequencies lower than 10 Hz, the spectrum provided by the fourier analysis of the data reveals no significant vibration peak or resonance point.

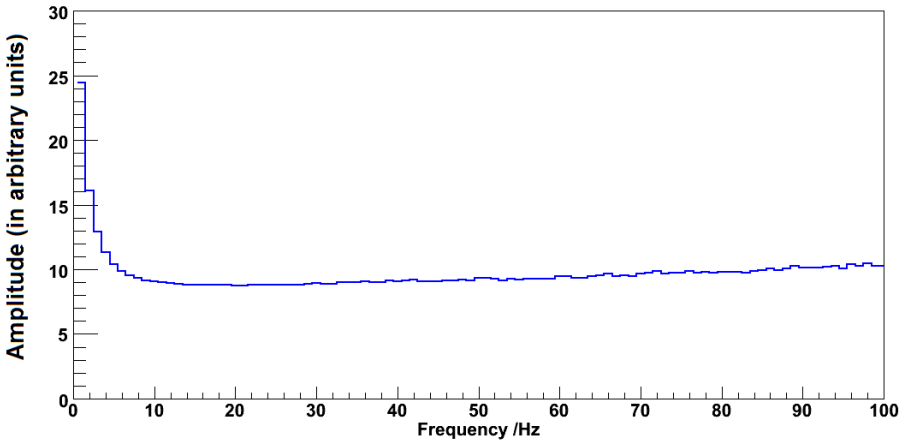

Figure 68: Vibration spectrum in the 1-100Hz frequency range.

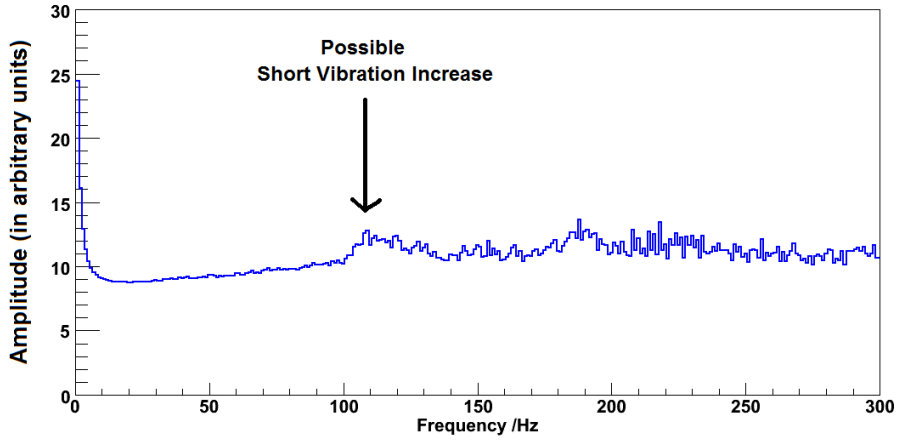

Figure 69: Vibration spectrum in the 1-300Hz frequency range.

7 Recommended Improvements

After observing the results of the test measurement in the Los Leones Fluorescence Detector, a number of simple improvements are desirable for the system.

Most of the difficulties stem from the use of the commercial weather station. Due to the problems caused by the wireless transmission of the temperature sensors, their replacement with wired temperature sensors would probably improve the reliability of the temperature monitoring. In addition to this, wired temperature sensors would allow the use of an external power supply, instead of using AA batteries with limited autonomy.

In order to confirm the stability of the input voltage of the potentiometers, the fifth and last channel of the microBOX ADC should be configurated to measure possible fluctuations in the power supply.

A new UPS battery system would also be suitable for the Tilt Monitor, as the one currently used belongs to the Fluorescence Detector and must be replaced.

Finally, in order to further understand the performance of the sensors, it would perhaps be suitable to build an additional monitoring setup. This setup could then be used as a reference in the laboratory at the RWTH in Aachen.

8 Conclusion

Once operational, the High Elevation Auger Telescopes will offer an extremely useful addition to the current Fluorescence Detector configuration of the Pierre Auger Observatory. However, the properties of the new telescopes could potentially become problematic and lead to mechanical deformations of their structure. Therefore, in order to guarantee their stability, a reliable monitoring system is required.

After observing the results displayed in this diploma thesis, the Tilt Monitor developed at the RWTH Aachen seems to provide more than adequate results.

First of all, the choice of the sensors has been proven to be reliable for the purpose of the project. The two measuring methods provide accurate and redundant information about the deformation of the telescopes. The two parameters, distance and inclination, constitute the basis of the monitoring. The number of sensors (four inclinometers and four potentiometers) suffices for a complete analysis of the camera deformations. Furthermore, the distance sensors provide information in a considerable time range, going from 100Hz vibrations to month-long fluctuations. While the inclination sensors are not capable of measuring such vibrations, their 4-5Hz sampling rate significantly contributes to the monitoring process.

The software implemented with LabVIEW for the DAQ system is perfectly adapted for the task, while remaining simple and stable. It also allows a real-time monitoring of the data and an easy access to the source code.

The successful calibration of both distance and inclination sensors reduces the uncertainty down to considerable levels. With typical distance uncertainties below 15μm, the distances are measured with a precision more than 30 times higher than the 0.5mm tolerance of the mirror-camera distance. Inclinations are also monitored with an impressive accuracy. In this case, the typical uncertainty rarely exceeds 0.02^o, thus remaining under one fifth of the 0.1^o inclination tolerance.

The constant weather monitoring performed by the weather station also provides useful information about the repercussions of the environmental factors in the stability of the telescope. Nevertheless, the setup could potentially be improved by using wired temperature sensors instead of wireless ones, so as to avoid wireless transmission difficulties.

Some other minor difficulties remain. Small changes can therefore be made in order to improve the overall performance of the system. For instance, the significant temperature sensitivity of the inclinometers combined with higher than expected temperature fluctuations inside the FD building require a more accurate temperature monitoring. In addition to this, the cause of the problem affecting the distance sensor number 0 has yet to be explained.

The test setup in an existing fluorescence telescope constitutes the last step before the final installation in the HEAT telescopes. The results suggest the long-term stability of the system as well as its ability to perform the required measurements in a real environment. It also serves as a reference measurement for later measurements. Once the construction of the HEAT enhancement finished, the Tilt Monitor will be ready to measure the mechanical deformations inside the telescope shelters.

References

[1] V.F. Hess, Über Beobachtungen der durchdringen Strahlung bei sieben Freiballonfahrten, Phys. Zeit. 13 1084 (1912).

[2] The Pierre Auger Collaboration, Enhancement of the PAO Fluorescence Detector by Additional Telescopes with Elevated Field of View, Proposal to the CB of the Pierre Auger Collaboration (2006)

[3] Pierre Auger, Roland Maze, Paul Ehrenfest et Andr Freon, Les grandes gerbes de rayons cosmiques, J. Phys. Radium 10 1 (1939) 39-48.

[4] J. Cronin, T. Gaisser, and S. Swordy, Cosmic Rays at the Energy Frontier, Scientific American 276, 44 (1997).

[5] A. M. Hillas, The Origin of Ultra-High-Energy Cosmic Rays, Ann. Rev. Astron. Astroph. 22, 425 (1984).

[6] W. Heitler, The Quantum Theory of Radiation (third ed.), Oxford University Press, London (1954) p. 386 (Section 38).

[7] The Pierre Auger Collaboration, The Pierre Auger Observatory Design Report: Second Edition (1997), http://www.auger.org/admin/DesignReport/index.html.

[8] S. Argirò, The Pierre Auger Observatory and its Fluorescence Detector, for the Pierre Auger Collaboration, Università degli Studi di Torino and INFN (2002).

[9] K. Greisen, Phys. Rev. Lett. 16, 748 (1966). G. T. Zatsepin and V. A. Kuzmin, JETP Lett. 4, 78 (1966).

[10] M. Palatka et al., On optics of FD without corrector ring, GAP-2003-058

[11] E. Fermi, On the Origin of the Cosmic Radiation, Phys. Rev. 75, 1169 (1949).

[12] H.V. Klapdor-Kleingrothaus, K. Zuber, Teilchenastrophysik: Teubner Studienbücher (1997).

[13] M. Unger, Shower Profile Reconstruction from Fluorescence and Cherenkov light, GAP-2006-010.

[14] P. Travnicek et al., Test of FD the camera pointing by checking the parameters of reconstructed SDPs in CLF laser events, GAP-2006-032

[15] T.Winchen, Measurements of the Continuous Radio Background and Comparison with Simulated Radio Signals from Cosmic Ray Air Showers at the Pierre Auger Observatory: Diploma thesis, RWTH Aachen University (2007)

[16] N.Scharf, RADAR Detection of Extended Air Showers: Diploma thesis, RWTH Aachen University (2008)

[17] M. Takeda, et al., Astropart. Phys. 19 (2003).

[18] T. Abu-Zayyad, et al., Phys. Rev. Lett., astro-ph/0208243

[19] The Pierre Auger Observatory, http://www.auger.org.

[20] S. N. Vernov et al. Cosmic rays and cosmophysical problems. Novosibirsk: SB AS USSR, (1964).

[21] G. Cunningham et al., Ap. J. 236, L75 (1980).

[22] J. Nishimura, Handbuch der Physik. Springer, Berlin - Heidelberg, (1967).

[23] J. Cronin, Cosmic rays: the most energetic particles in the universe, Rev. Mod. Phys., Vol. 71, No. 2, Centenary (1999).

[24] Disynet GmbH., http://www.sensoren.info/.

[25] M. S. Longair,high energy astrophysics, Cambridge University Press, Cambridge, (1992).

[26] The Pierre Auger Collaboration, et al. Correlation of the Highest-Energy Cosmic Rays with Nearby Extragalactic Objects. Science 318, 938 (2007).

[27] http://root.cern.ch/

[28] The Pierre Auger Collaboration, December 2007 - January 2008 Pierre Auger Project Progress Report, (2008).

[29] A. Etchegoyen, AMIGA, Auger Muons and Infill for the Ground Array, for the Pierre Auger Collaboration, Departamento de Física (Tandar), Centro Atómico Constituyentes, Comisión Nacional de Energía Atómica and UTN-FRBA, (2007)

9 Appendix

The following figures show the exact LabVIEW code developed and used for the Tilt Monitor system. The screenshots include the block diagrams of every subprogram and structure of the TiltMonitor.exe and DataTransfer.exe executables.

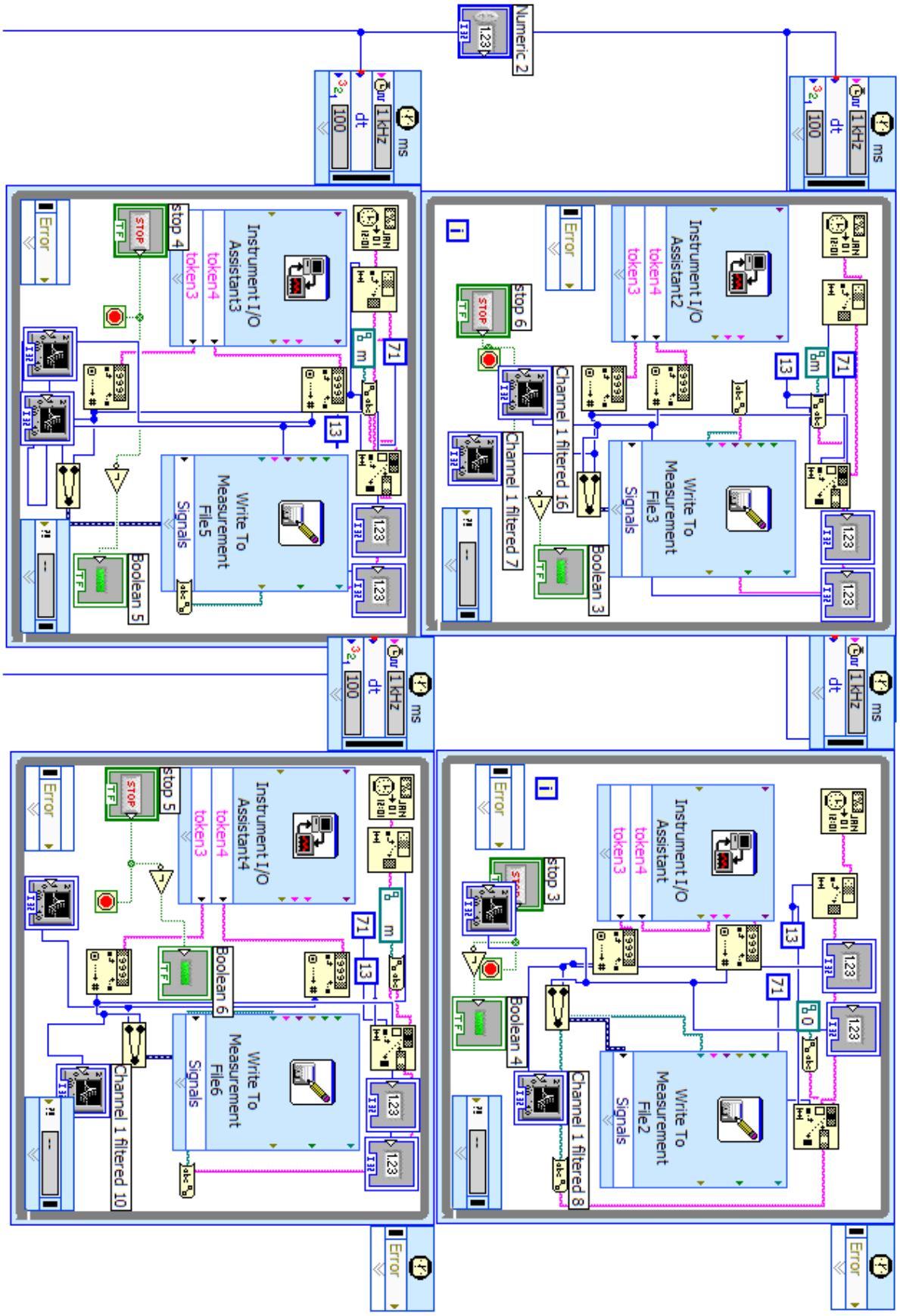

Figure 70: Detailed LabVIEW Block diagram of the inclination DAQ program.

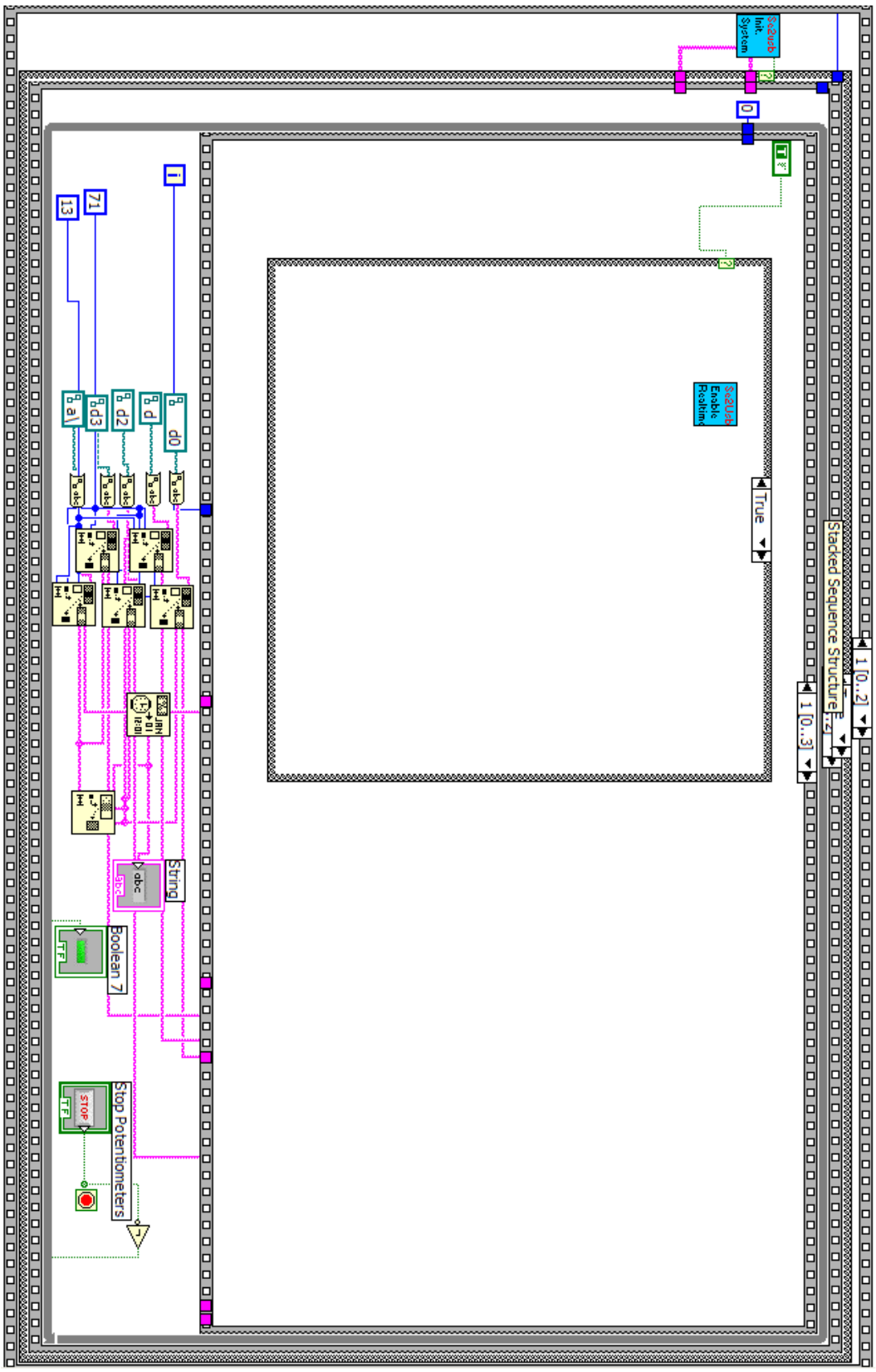

Figure 71: Detailed LabVIEW Block diagram of the distance DAQ program, part 1 (initialization).

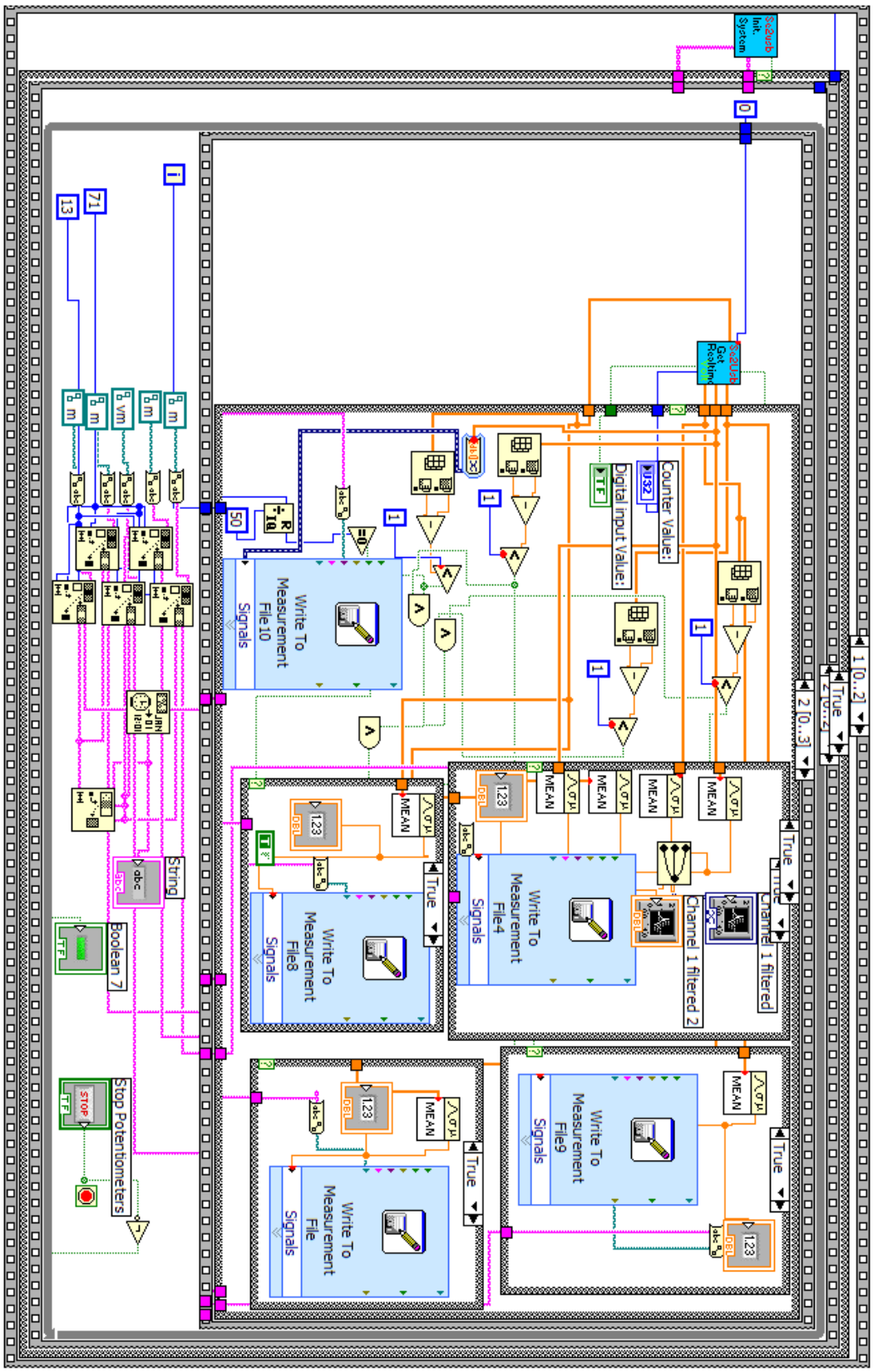

Figure 72: Detailed LabVIEW Block diagram of the distance DAQ program, part 2 (measurement).

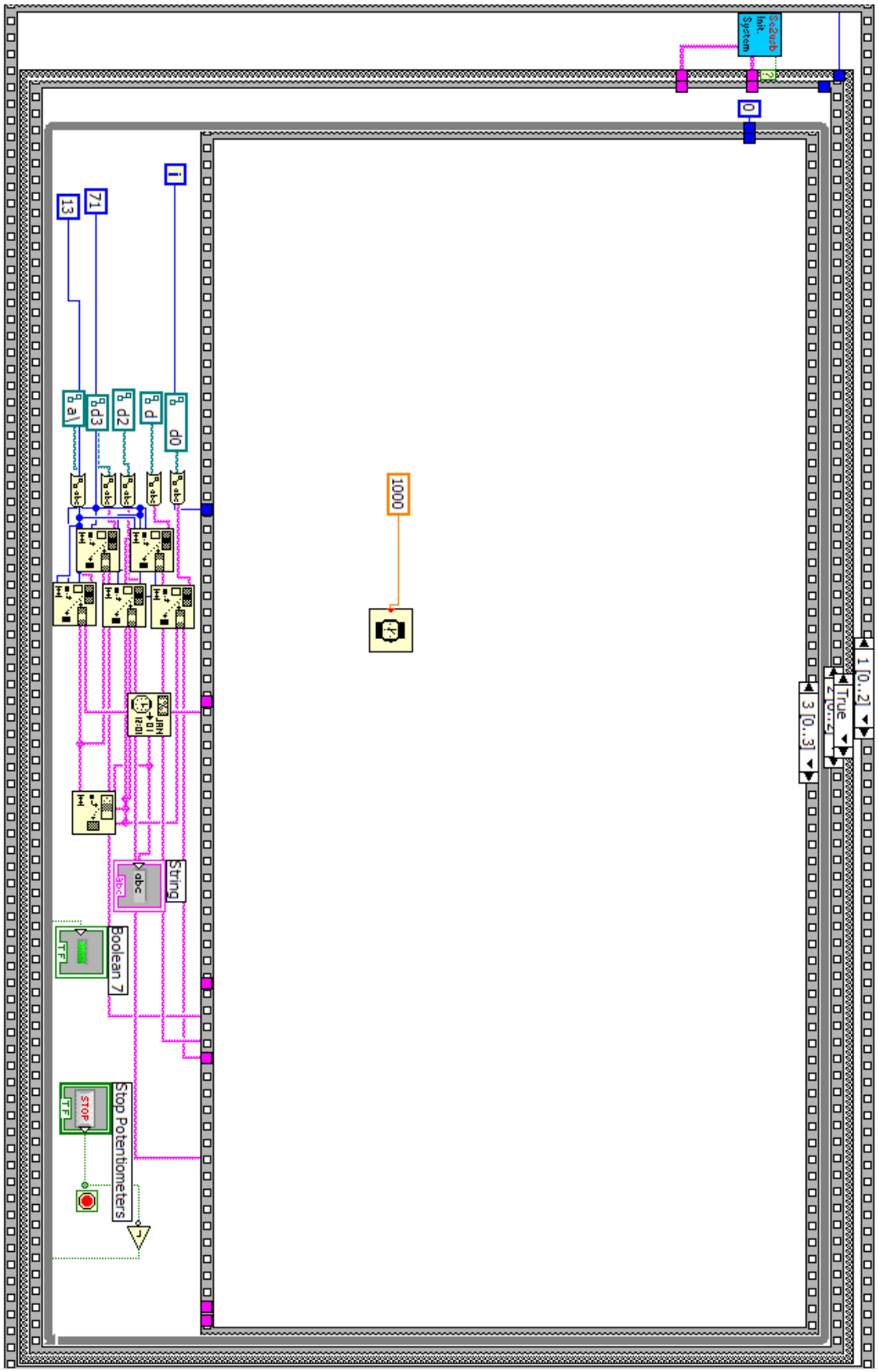

Figure 73: Detailed LabVIEW Block diagram of the distance DAQ program, part 3 (measurement duration).

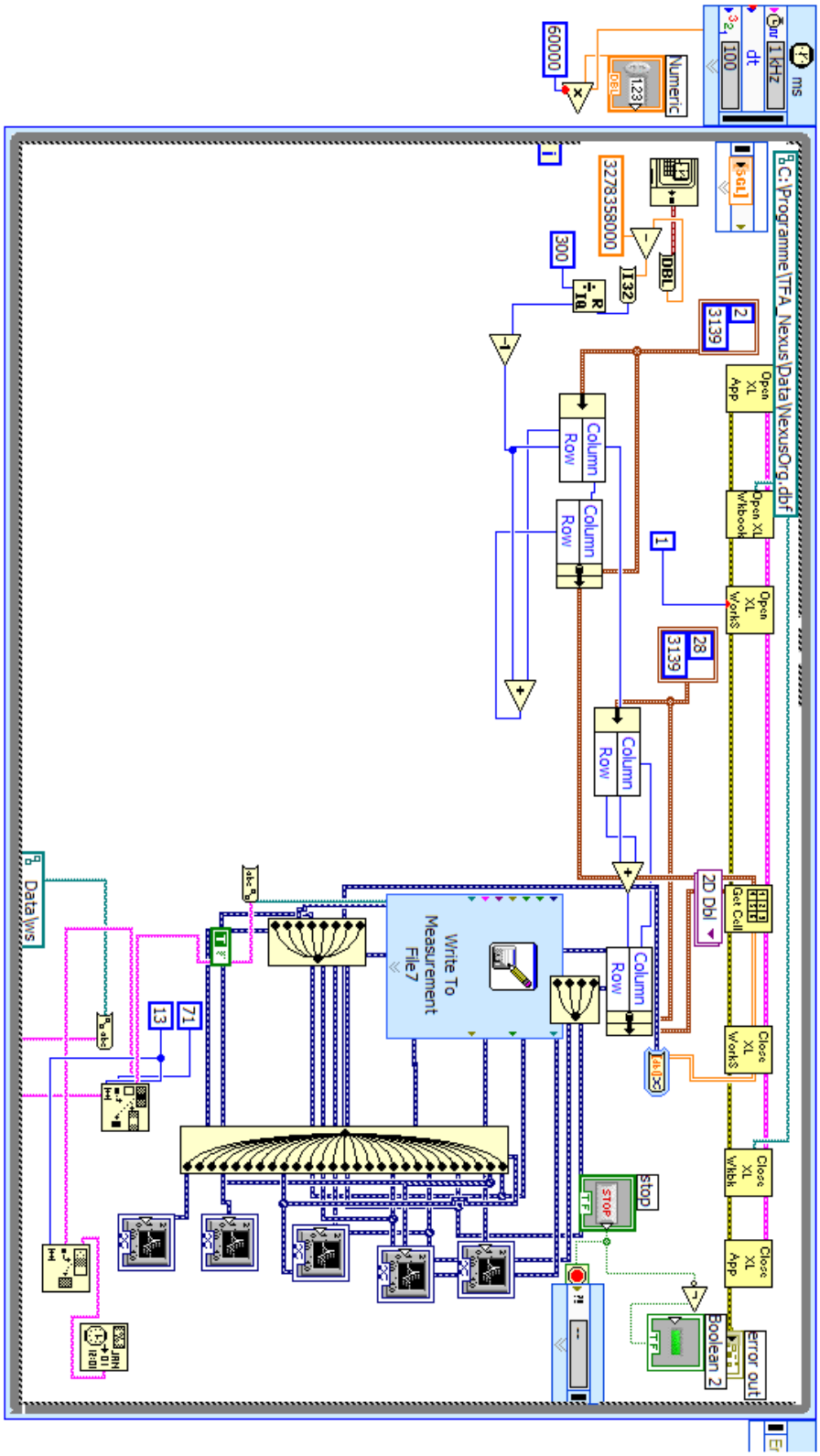

Figure 74: Detailed LabVIEW Block diagram of the weather DAQ program.

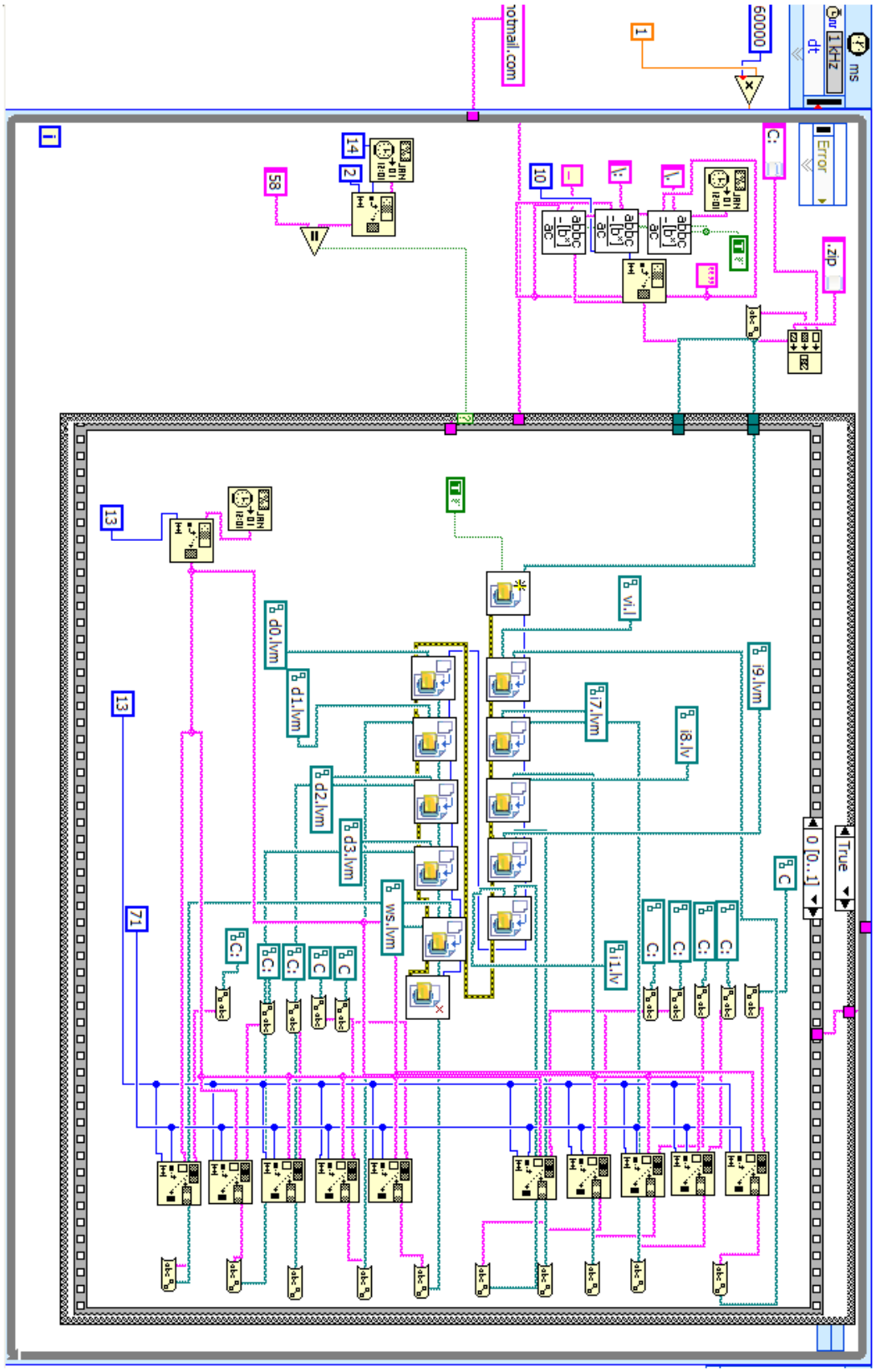

Figure 75: Detailed LabVIEW Block diagram of the data transfer program, part 1 (data compression).

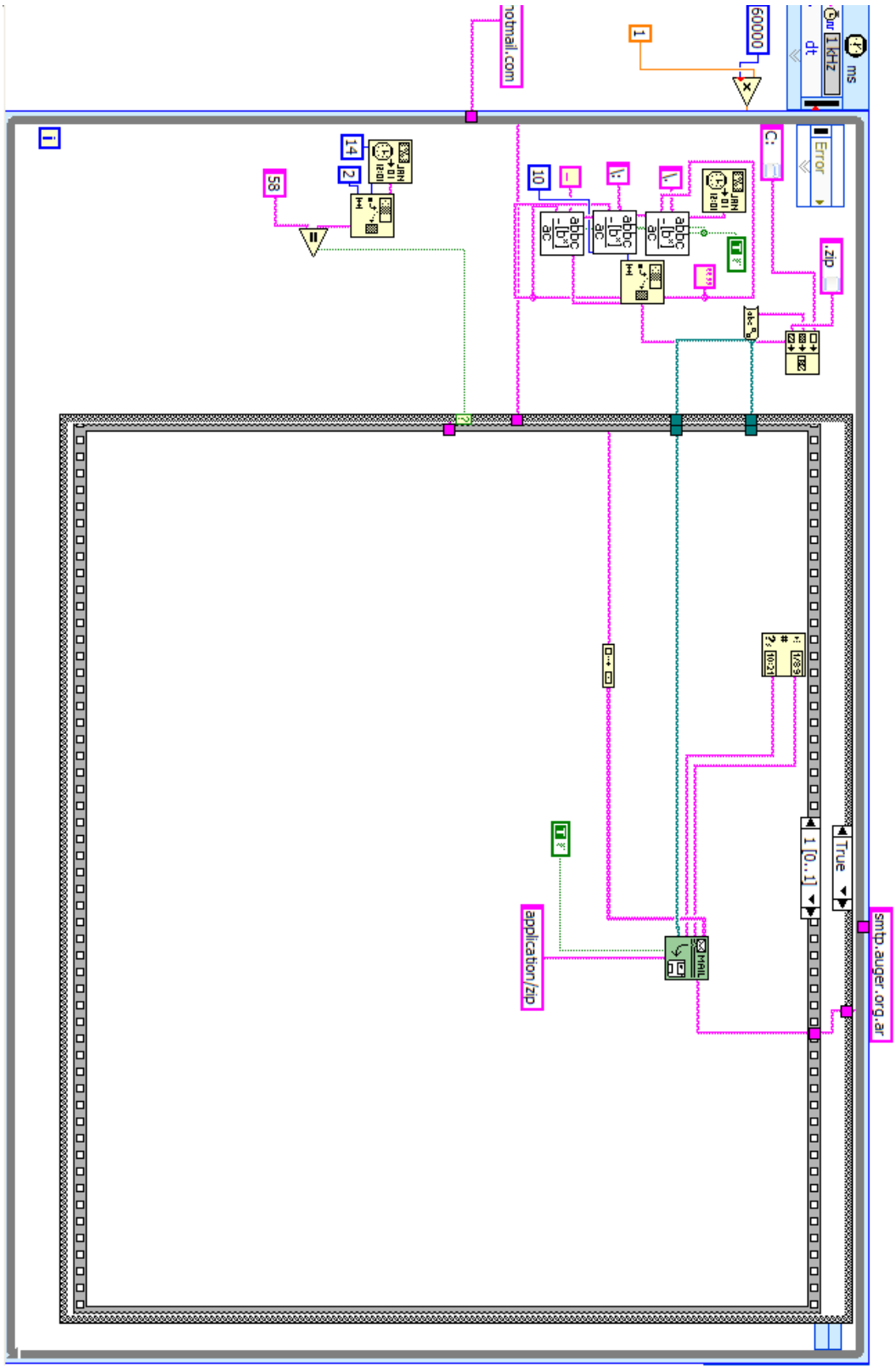

Figure 76: Detailed LabVIEW Block diagram of the data transfer program, part 2 (data transfer through e-mail).

List of Figures

Acknowledgements

Working with the sensors was not always easy and sometimes required large quantities of patience, but the environment in which I did it made it definitely enjoyable. In fact, during this past year, I received the help and support of many people, that I would now therefore like to thank.

First of all, I would like to thank Matthias Leuthold. The incredible amount of help, support and advice he gave me turned out to be, without a doubt, essential for this project. The Auger student group in Aachen, and especially Nils Scharf, Stefan Fliescher and Hans Dembinski, was always there to help with any difficulty or problem I encountered, for which I am very thankful. I would also like to thank Prof. Hebbeker and Prof. Erdmann for providing the best and wisest guidance during my last year as a student in the RWTH Aachen.

It is important not to forget the work done by the Mechanical and Electronical Workshops of the III. Physikalisches Institut of the RWTH Aachen, and more exactly by Henry Szczesny, H. Rainer Lampe and Barthel Philipps. The hardware they provided was extremely useful.

The two weeks spent in Argentina were both exciting and exhausting. Although the intensive work done there left me practically no time to enjoy the magnificent landscape, the enthusiasm and cooperation of the people over at the Auger site made everything easier. I am therefore very grateful for the help provided by the FD team in Malargüe and by Primo Vitale in particular.

Finally, I wish the best luck to Stephan Schulte, who will be from now on responsible for the Tilt Monitor and its final installation in the HEAT telescopes.

Statement

I hereby declare that this thesis is entirely my own, unaided work and that recognition has been given to the references used. It has not been submitted for any degree or examination at any other university.

Joaquín Calvo de Nó

March 19, 2008